



저작자표시-비영리-변경금지 2.0 대한민국

이용자는 아래의 조건을 따르는 경우에 한하여 자유롭게

- 이 저작물을 복제, 배포, 전송, 전시, 공연 및 방송할 수 있습니다.

다음과 같은 조건을 따라야 합니다:



저작자표시. 귀하는 원저작자를 표시하여야 합니다.



비영리. 귀하는 이 저작물을 영리 목적으로 이용할 수 없습니다.



변경금지. 귀하는 이 저작물을 개작, 변형 또는 가공할 수 없습니다.

- 귀하는, 이 저작물의 재이용이나 배포의 경우, 이 저작물에 적용된 이용허락조건을 명확하게 나타내어야 합니다.
- 저작권자로부터 별도의 허가를 받으면 이러한 조건들은 적용되지 않습니다.

저작권법에 따른 이용자의 권리는 위의 내용에 의하여 영향을 받지 않습니다.

이것은 [이용허락규약\(Legal Code\)](#)을 이해하기 쉽게 요약한 것입니다.

[Disclaimer](#)

공학박사 학위논문

**Evaluation of structure-property
relationship in tailor-made metallic glasses**

**Tailor-made 비정질 합금에서
구조-특성간 상관관계 규명**

2018년 2월

서울대학교 대학원

재료공학부

박태규

Abstract

Evaluation of structure-property relationship in tailor-made metallic glasses

TaeGyu Park

Department of Materials Science and Engineering

College of Engineering

Seoul National University

Since amorphous alloys have disordered atomic structures that are different from those of crystalline alloys, they exhibit various unique properties that can not be explained by conventional theory. In particular, when the amorphous material increases in size, It is very likely to be applied as However, unlike crystalline alloys, amorphous alloys have disadvantage that surplus breakdown occurs at the same time as breakdown because there are no plastic deformation mechanisms such as slip or dislocation. In addition, due to the amorphous forming ability(which requires a rapid cooling rate), it is difficult to fabricate a general metal manufacturing process; therefore, there is a limitation in the size of amorphous material.

Therefore, to expand the possibility of using amorphous materials as structural materials, it is essential to improve the plastic deformation resistances of the materials and to enlarge them while maintaining the amorphous structure.

Therefore, in this study, we analyzed the atomic-scale structural change of an amorphous alloy depending on the added element and experimentally investigated the change of physical properties according to the structural change. As a result, we overcame the limit of application of existing amorphous materials as a structural material. We propose a concept to control the structure. In addition, we tried to overcome the limitations of existing amorphous alloys by studying enlargement through additive manufacture of amorphous powders using 3D the printing process, which is a leading innovation in manufacturing technology.

To investigate the structural and physical properties of a monolithic amorphous phase, a simple binary system (Ni-Nb) was selected and a series of elements (Zr, Gd, Y) was added to the alloy. When Zr (+4 kJ/mol), which has a relatively small positive heat of mixing, was added to the Ni-Nb binary alloy, no heterogeneity could be confirmed in monolithic amorphous phase through transmission electron microscopy or SAXS (small angle X-ray scattering). However, as a result of confirming the interatomic bonding distance and coordination number using EXAFS (extended X-ray absorption fine structure), local atomic-scale heterogeneity in the single amorphous

phase was confirmed due to the addition of Zr. In addition, the local atomic-scale heterogeneity could provide several sites where shear bands can be generated, thereby preventing sudden destruction by a concentrated shear band and ultimately improving the amorphous stretching. These results were the first to be experimentally identified. In addition, the correlation between heterogeneity at the atomic scale and the physical properties was confirmed through bulk specimens. It was influenced by the cooling rate.

On the other hand, when Y and Gd (+30 kJ/mol), which have positive heats of mixing with constituent elements, were added to the Ni-Nb binary alloy, a phase-separated amorphous phase was obtained. The microstructures and thermal properties of amorphous phase separation were different despite having the same enthalpy of mixing. Based on the thermodynamic data, we developed a new alloy design concept to control the microstructures of phase separated amorphous alloys by calculating the miscibility gap of the phase separated amorphous material (which can induce differences in microstructure) and examining the governing factor.

To overcome the size limitation of amorphous material, we observed that the change of physical properties of the printed result varied according to process variable control, which was confirmed through 3D print(powder bed fusion) processing of the amorphous powder. By using the amorphous powder, the amorphous structure could be enlarged while retaining the amorphous structure when the

process parameters and the heat input of 3D printing were controlled appropriately. In addition, the amorphous mechanical behavior experiment (produced by 3D printing) showed a difference in cooling rate within a single amorphous state during amorphous manufacture through 3D printing, unlike conventional amorphous manufacturing, It was found that atomic-scale heterogeneity in the single amorphous phase can increase elongation of the amorphous phase.

A broad understanding of the amorphous structure and property relationships from this work will ultimately provide a new way to design and process various alloys to take advantage of the excellent properties of amorphous materials. Furthermore, a new milestone for manufacturing customized amorphous materials for their industrial application is suggested.

Keywords: Metallic glasses, Positive mixing enthalpy, Chemical heterogeneity, Preferential bonding, Plasticity, Laser powder fusion bed additive manufacturing

Student Number: 2013-30179

Table of Contents

Abstract	i
Table of Contents	v
List of Figures	ix
List of Table	x vii
Chapter 1. Introduction	1
1.1. Metallic glasses	1
1.1.1. Definition of metallic glasses	1
1.1.2. Development of metallic glasses	2
1.1.3. Application of metallic glasses	5
1.2. Deformation of metallic glasses	8
1.2.1. Deformation mode of metallic glasses	13
1.2.2. Plastic deformation of metallic glasses	22
1.3. Improvement of plasticity of bulk metallic glasses	25
1.3.1. Ex-situ formed bulk metallic glass composites	26
1.3.2. In-situ formed bulk metallic glass composites	26
1.4. Phase separation in metallic glasses	29
1.4.1. Thermodynamic background phase separation	33
1.4.2. Mechanism of phase separation	38
1.5. Additive manufacturing	42
1.5.1. Type of additive manufacturing	42
1.5.2. Metal additive manufacturing	46
1.5.3. Powder bed fusion additive manufacturing	52
1.6. Research Objectives	56

Chapter 2. Experimental Procedures	58
2.1. Sample preparation	58
2.1.1. Arc melting	58
2.1.2. Melt spinning	58
2.1.3. Injection casting	59
2.1.4. Atomization	59
2.1.5. SPS	62
2.1.6. Laser PBF AM	62
2.2. Microstructural characterization	64
2.2.1. X-ray diffraction	64
2.2.2. Scanning electron microscopy	64
2.2.3. Transmission electron microscopy	64
2.2.4. Small angle X-ray scattering	65
2.2.5. Extended X-ray absorption fine structure	65
2.3. Thermal and mechanical analysis	69
2.3.1. Differential scanning calorimeter	69
2.3.2. Nano-indentation tests	69
2.3.3. In-situ bending tests	70
2.3.4. Compression test	71
Chapter 3. Development of tailor made metallic glasses by controlling composition	73
3.1. Introduction	73
3.2. Effect of Small Positive Heat of Mixing Between Constituent Elements	77
3.2.1. Microstructural characterization in Ni-Nb-Zr	77
3.2.2. Deformation behavior in Ni-Nb-Zr	91
3.2.3. Enhancement of plasticity by processing control ...	97

3.2.4. Discussion	100
3.3. Effect of Large Positive Heat of Mixing Relationship Between Constituent Elements	101
3.3.1. Microstructural characterization in Ni-Nb-(Y, Gd)	101
3.3.2. Governing factors for manipulating microstructure in phase separating metallic glasses	107
3.3.3. Discussion	112
3.4. Summary	112

Chapter 4. Development of tailor made metallic glasses

by controlling process	114
4.1. Introduction	114
4.2. Printable powder preparation for additive manufacturing	116
4.2.1. Powder preparation	116
4.2.2. Powder property characterization	119
4.2.3. Discussion	125
4.3. Feasibility assessment of laser powder fusion bed additive manufacturing	127
4.3.1. Building strategy	127
4.3.2. Characterization output of PBF AM	129
4.3.3. Mechanical Properties on output of AM	139
4.3.4. Discussion	152
4.4. Summary	156

Chapter 5. Conclusions

158

Bibliography	I
Abstract in Korean	XVI
Acknowledgements	XIX

List of Figures

Figure 1.1 Maximum diameters of BMG rods produced with various alloy systems and the years in which they were discovered. Reprinted from [10] with permission through the Copyright Clearance Center.

Figure 1.2 Schematic illustration of atomic shear transformation in metallic glasses. (a) Free volume mode and (b) Shear transformation zone (STZ) model. Recomposed from [20] with permission through the Copyright Clearance Center.

Figure 1.3 Schematic deformation mechanism maps for metallic glasses. Recomposed from [20] with permission through the Copyright Clearance Center

Figure 1.4 (a) Volume-temperature relationship in transformation among liquid, glass, and crystal. (b) La-Al-Li metallic glass homogeneously deformed to 20,000% in the supercooled region. (b) is recomposed from [37] and [40] with permission through the Copyright Clearance Center.

Figure 1.5 (a) Schematic illustration of the initial process of a shear band. (b) High-resolution TEM image of shear band formation during bend testing of $\text{Fe}_{79.3}\text{B}_{16.4}\text{Si}_4\text{C}_{0.3}$ metallic glass ribbon. Recomposed from [54] with permission through the Copyright Clearance Center.

Figure 1.6 Ashby map of fracture toughness versus strength of

materials. Reprinted from [55] with permission through the Copyright Clearance Center.

Figure 1.7 Various methods of producing BMG matrix composites to improve of plasticity in BMGs

Figure 1.8. TEM images of phase separating metallic glasses (a) $\text{La}_{27.5}\text{Zr}_{27.5}\text{Cu}_{10}\text{Ni}_{10}\text{Al}_{25}$. (b) $\text{Nd}_{30}\text{Zr}_{30}\text{Co}_{30}\text{Al}_{10}$. (c) $\text{Ni}_{54}\text{Nb}_{23}\text{Y}_{23}$. and (d) $\text{Zr}_{35}\text{Gd}_{20}\text{Al}_{23}\text{Ni}_{22}$. The image shown in (b) is a dark-field image, while the others are all bright field images. The insets are selected diffraction patterns(SADP) corresponding to each observed regions. Reprinted from [73, 74, 78] and [79] with permission through the Copyright Clearance Center.

Figure 1.9. Schematic illustration of (a) Gibbs free energy change by mixing(ΔG^{mix}), (b) miscibility gap in binary system, and (c) microstructure formed by phase separation during on the compositions of alloy melt.

Figure 1.10. Schematic diagrams showing spatial variations in concentration variation and morphology evolution ($t_1 < t_2 < t_3$) during phase separation by two different mechanisms: (a) nucleation and growth and (b) spinodal decomposition. Reprinted from [64] with permission through the Copyright Clearance Center.

Figure 1.11. Part fabrication through additive manufacturing technology.

- Figure 1.12. Metal additive manufacturing process according to feedstock dimension and process temperature.
- Figure 1.13. (a) Weld generation after single-pass laser scanning, (b) map of weld metal microstructures according to temperature gradient and solidification rate. Recomposed from [100] with permission through the Copyright Clearance Center.
- Figure 2.1. (a) Arc discharge machine installed in laboratory and (b) schematic diagram of arc melting process utilized for the preparation of master alloys with desired compositions.
- Figure 2.2. Overview of gas atomization instruments in KITECH.
- Figure 2.3. Mlab cusing machine and 3D model
- Figure 2.4. Overview of small angle X-ray Scattering instruments in the Pohang Accelerator Laboratory
- Figure 2.5. Overview of extended X-ray absorption fine structure instruments in the Pohang Accelerator Laboratory
- Figure 2.6. Self-designed experimental equipment for in-situ bending test.
- Figure 3.1. Additional alloying elements having positive heat of mixing between constituent elements ; (a) small positive (Zr), and (b) large positive (Y, Gd).
- Figure 3.2. High resolution TEM images and SADPs obtained from melt spun (a) $\text{Ni}_{60}\text{Nb}_{40}$ and, (b) $\text{Ni}_{60}\text{Nb}_{30}\text{Zr}_{10}$ ribbons.
- Figure 3.3. SAXS patterns obtained from melt spun (a) $\text{Ni}_{60}\text{Nb}_{30}\text{Zr}_{10}$

and, (b) $\text{Ni}_{60}\text{Nb}_{20}\text{Zr}_{20}$ ribbons.

Figure 3.4. Fourier transform magnitude around (a) Ni for $\text{Ni}_{60}\text{Nb}_{40-x}\text{Zr}_x$ and, (b) Nb for $\text{Ni}_{60}\text{Nb}_{40-x}\text{Zr}_x$ alloy (x=0, 10, 20 at%).

Figure 3.5. EXAFS spectra $k^3\chi(k)$ versus k curves of (a) Ni K-edge for $\text{Ni}_{60}\text{Nb}_{40-x}\text{Zr}_x$ and (b) Nb k-edge for $\text{Ni}_{60}\text{Nb}_{40-x}\text{Zr}_x$ alloy (x=0, 10, 20 at%).

Figure 3.6. Coordination numbers around element of (a) Ni K-edge for $\text{Ni}_{60}\text{Nb}_{40-x}\text{Zr}_x$ (b) Nb k-edge for $\text{Ni}_{60}\text{Nb}_{40-x}\text{Zr}_x$ alloy (x=0, 10, 20 at%)

Figure 3.7. XANES spectra for (a) Ni K-edge and (b) Nb K-edge and (c) fitting data of Zr20, (d) weight factor for each alloy.

Figure 3.8. (a) Cumulative probability distribution of strain burst sizes and, (b) β and S_c values for each alloy.

Figure 3.9. Shear steps formed on the surfaces of (a) Zr0 and, (b) Zr20 and, (c) the number of shear bend events for (a) and (b).

Figure 3.10. Compressive stress-strain curves for injection-cast samples with diameter of 1 mm.

Figure 3.11. DSC traces obtained from (a) melt-spun $\text{Ni}_{60}\text{Nb}_{40-x}\text{Y}_x$ (x= 0, 10, 20 at.%) and (b) $\text{Ni}_{60}\text{Nb}_{40-x}\text{Gd}_x$ (x= 0, 10, 20 at.%) ribbons.

Figure 3.12. (a) TEM BF image of melt-spun $\text{Ni}_{60}\text{Nb}_{20}\text{Y}_{20}$ ribbon. (b) and (c) SADPs obtained from region with a diameter of

500 nm including dark area ① and bright matrix ② at the same time and 200 nm including only ①, respectively. (d) DF image obtained by positioning the objective lens aperture on the outer halo ring in (c). (e) TEM BF image, (f) and (g) SADPs for the region with a diameter of 500 nm encompassing ③ and ④ and 200 nm including only ③, respectively. (h) DF image obtained by positioning the objective lens aperture on the outer halo ring in (f). Ni-Nb rich amorphous phase in each alloy (① and ③) shows brighter contrast.

Figure 3.13. (a) and (b) Schematic diagram of phase separated microstructures of $\text{Ni}_{60}\text{Nb}_{20}\text{Y}_{20}$ and $\text{Ni}_{60}\text{Nb}_{20}\text{Gd}_{20}$, respectively. (c) and (d) Metastable miscibility gap for the liquid phase at pseudo-binary section of $\text{Ni}_{60}\text{Nb}_{40-x}\text{Y}_x$ and $\text{Ni}_{60}\text{Nb}_{40-x}\text{Gd}_x$ ($0 \leq x \leq 40\text{at.}\%$), respectively. The former was calculated by thermodynamic parameters, while the latter was constructed based on microstructural differences between $\text{Ni}_{60}\text{Nb}_{20}\text{Y}_{20}$ and $\text{Ni}_{60}\text{Nb}_{20}\text{Gd}_{20}$. Dashed lines represent the glass transition temperature (T_g) of $\text{Ni}_{60}\text{Nb}_{40}$.

Figure 4.1. Powder preparation procedure.

Figure 4.2. Layering ability of powders on the build-platforms; (a) poor and (b) good.

Figure 4.3. Morphology of as-atomized powder; (a) plane-view, (b) cross-section view, (c) powder with particles smaller than

25 μm and (d) powder with particles larger than 106 μm .

Figure 4.4. Characteristics of prepared powders ; (a) Morphology of powders of each size and (b) XRD results of powders of each size.

Figure 4.5. Comparison of surface properties of (a) as-atomized powder and (b) acid-treated powder.

Figure 4.6. Phase composition of parts as-built (a) from amorphous powder and (b) from crystallized powder

Figure 4.7. Microstructures of parts as-built from amorphous powder: (a) BSE image of 1-1(90W-500mm/s) part, (b) BSE image of 1-2(90W-750mm/s) part, (c) BSE image of 1-3 (90W-1,000mm/s) part, (d) BSE image of 1-4(90W-1,600mm/s) part, (e) SE image of 1-1(90W-500mm/s) part, and (f) SE image of 1-4 (90W-1,600mm/s) part

Figure 4.8. Microstructures of as-built parts from crystallized powder: (a) SE image of 90W-1,000mm/s part from crystallized powder, (b) BSE image of (a), (c) SE image of 90W-1,600 mm/s part from crystallized powder, and (d) BSE image of (c)

Figure 4.9. Estimation of thermal cycles and phase evolutions of bulk metallic glass part during laser PBF process; (a) cross-sectional view of weld zone, and (b) competition between thermal cycle and crystallization kinetics of BMG weld zone

- Figure 4.10. The shapes and conditions of three different samples fabricated by varying the hatch distance (65 μm , 85 μm , and 125 μm).
- Figure 4.11. (a) XRD patterns and (b) DSC curves of samples fabricated by suction-casting (SC), spark plasma sintering (SPS), and 3D printing.
- Figure 4.12. Optical microscopy images of samples fabricated by suction-casting (SC), spark plasma sintering (SPS), and 3D printing.
- Figure 4.13. Vickers hardnesses obtained from samples fabricated by suction-casting (SC), spark plasma sintering (SPS), and 3D printing.
- Figure 4.14. Macro-hardnesses obtained from samples fabricated by suction-casting (SC), spark plasma sintering (SPS), and 3D printing.
- Figure 4.15. Correlation between $\ln[\ln(1-f)^{-1}]$ and τ_{max} , V^* obtained from samples fabricated by suction-casting (SC), spark plasma sintering (SPS), and 3D printing.
- Figure 4.16. (a) The cumulative probability distribution of strain burst sizes, (b) β and Sc values for SC, SPS, AM.
- Figure 4.17. (a) Schematic of the thermal histories and (b) total free volumes of SC, SPS, AM.
- Figure 4.18. (a) Optical microscopy images after macroindentation and (b) the stress-strain curves of uniaxial compression tests

of SC, SPS, and AM.

Figure 5.1. Summary of this study

List of Tables

Table 1.1 Standard classification of additive manufacturing (Ref. from [92])

Table 1.2. Commercialized metal AM technologies

Table 1.3. Comparison of metal additive manufacturing process(*
Process time : time generally required for making
 $125 \times 125 \times 125 \text{ mm}^3$ cubit product)

Table 3.1. Summaries of characteristic changes in various alloy systems with additional element having positive heat of mixing with one or more constituent elements ; maximum diameter for glass formation(D_{\max}) fracture strain in compressive mode(ϵ_p) and heat of mixing among constituent elements

Table 3.2 Calculated chemical short range order parameter for $\text{Ni}_{60}\text{Nb}_{40-x}\text{Zr}_x$ alloy($x=0, 10, 20 \text{ at\%}$)

Table 4.1. Powder properties in relation to packing behavior

Table 4.2. Process parameter of laser PBF AM

Table 4.3. Summary of β and Sc values for SC, SPS, and AM.

Chapter 1. Introduction

1.1. Metallic glasses

1.1.1. Definition of metallic glasses

An "amorphous" solid is a solid in which there is random packing with no long-range order of the locations of the atoms. Numerous types of solid materials can be found or prepared in an amorphous form. For example, common window glass is an amorphous ceramic and many polymers (i.e., polystyrene) are amorphous. Amorphous solids can be formed by methods other than melt quenching, such as evaporation, sputtering, electro-/chemical deposition or the sol-gel method. Meanwhile, the standard definition of a "glass" refers only to the solid phase formed by any technique, having an amorphous structure, which exhibits glass transformation behavior [1]. Under these definitions, all glasses are amorphous, but not all amorphous solids are necessarily glasses.

Generally, the term "glass" refers to amorphous oxides, mostly silicates. To avoid uncertainty, other classes of glass often are referred to with a modifier, such as the term "metallic glass" to refer to amorphous metallic alloys.

Metallic materials are traditionally regarded crystalline in nature, possessing translational symmetry. That is, their constituent

atoms are arranged in a regular and periodic manner in three dimensions. Metals are difficult to prepare in an amorphous state. Unless a material has a high melting temperature (as ceramics do) or a low crystallization energy (as polymers tend to have), its cooling rate must be extremely rapid. As cooling proceeds, the material changes from a supercooled liquid, with properties one would expect from a liquid state material, to a solid. The temperature at which this transition occurs is called the glass transition temperature or T_g .

1.1.2. Development of metallic glasses

The first synthesis of an amorphous phase in the Au-Si system by rapid quenching techniques for chilling metallic liquids at very high rates of 10^5 to 10^6 K/s was reported by Duwez in 1960 [2]. Since the first report of an amorphous alloy, a great number of glass forming alloys have been discovered. Amorphous alloys show characteristic physical features, such as high strength, corrosion resistance, and electromagnetic properties, which are significantly different from the corresponding crystalline alloys due to their different atomic configuration [3]. However, due to the requirement of rapid solidification to avoid crystallization, amorphous alloys can normally be produced in the form of either thin ribbons or fine powders. This limits the application of amorphous alloys to special purposes, such as magnetic or brazing materials [4].

No pure metals and few metallic alloys are natural

glass-formers. A major challenge, therefore, is to obtain glassy alloys in bulk form in a simple operation such as casting. The critical thickness of bulk metallic glass (BMG) is defined as the maximum possible value of the minimum dimension (such as the diameter of a rod) that permits the sample to be fully glassy. However, to enable bulk molding, research has focused on slowing cooling rates to increase the critical casting thickness. In 1974, Chen obtained a critical casting thickness of 1 mm in Pd-T-P (T = Ni, Co, Fe) [5], realizing as well a slightly greater thickness with $\text{Au}_{55}\text{Pb}_{22.5}\text{Sb}_{22.5}$ in 1982 [6]. In the early 1980s, Turnbull et al. produced glassy ingots of $\text{Pd}_{40}\text{Ni}_{40}\text{P}_{20}$ with a diameter of 5 mm using surface etching followed by heating and cooling cycles. By processing the materials in a boron oxide flux, they increased its critical casting thickness to 1 cm, thus producing the first BMG [7]. Most BMG-forming compositions have been discovered since 1990, when the Inoue group carried out systematic searches for bulk glass formation in multicomponent alloys [8]. This was followed by a report of a Zr-based alloy [9]. During the last nearly 20 years, Inoue et al. have been able to produce several new BMGs using various alloy systems based on engineering metals such as Ti, Mg, Fe, Co, Ni and Cu. The maximum diameters obtained in the various alloy systems and the years in which they were discovered are presented in Figure 1 [10].

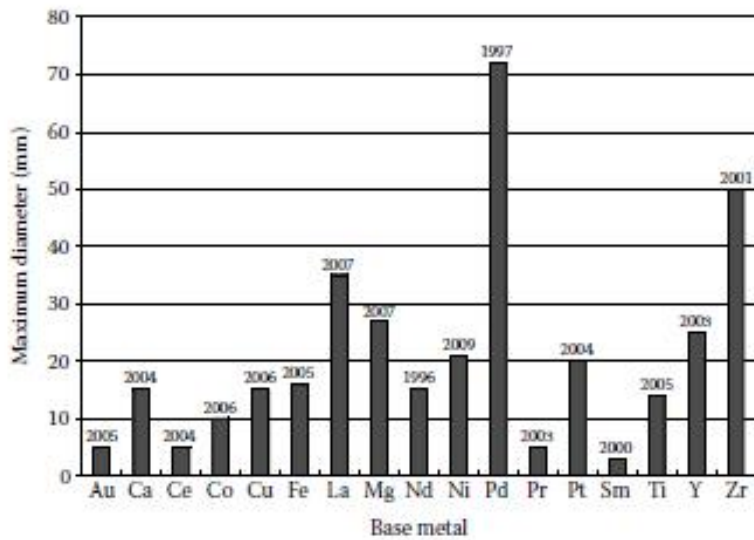


Figure 1.1 Maximum diameters of BMG rods produced with various alloy systems and the years in which they were discovered. Reprinted from [10] with permission through the Copyright Clearance Center.

1.1.3. Application of metallic glasses

Metallic glasses exhibit very high strength (both in tension and compression), very high hardness, a large elastic elongation limit, excellent corrosion resistance, and a good combination of soft magnetic properties. Although melt-spun glassy ribbons have somewhat similar properties, BMGs exhibit some special characteristics.

(1) BMGs are suitable for structural applications such as sporting goods (golf club heads, tennis rackets, baseball bats, bicycle frames, etc.) due to their high strength [11]. With no constringency during solidification, BMGs offer the possibility to be formed into net-shape products directly from their liquid states. In addition, superior surface flatness can be gained, owing to the absence of grain boundaries [12]. Direct net-shape-forming technology permits low-cost production of complex parts without any precision finishing. Superior surface flatness reduces wear and energy loss due to friction. From these performance and cost standpoints, BMGs are appealing for the production of small precision parts, such as gears for micro-motors [12]. This motor using BMG gear parts has a 313 times longer lifetime than that of a conventional motor with steel gear parts. Such excellent durability is thank to the high strength and superior surface flatness of BMG gear parts. In addition, there have been reports on the fabrication of diaphragm for pressure sensors ($Zr_{55}Al_{10}Ni_5Cu_{30}$) [13]

and pipes for a Coriolis mass flowmeter (CFM) ($\text{Ti}_{50}\text{Cu}_{25}\text{Ni}_{15}\text{Zr}_5\text{Sn}_5$) [14] using the high Young' modulus and strength of metallic glasses. High yield strain, a low loss coefficient and resilience are desirable, while low process-zone size and low ductility are unimportant at a small scale, crucially for micro electro mechanical system(MEMS) fabrication. One great advantage of BMGs is the ease with which complex shapes can be formed in a supercooled liquid state. BMGs exhibit good micro-forming ability because of their deformation mode of a Newtonian viscous flow or a similar phenomenon. Although the 3D structure necessary for large vertical displacement is difficult to fabricate through conventional MEMS processes, a microactuator capable of such vertical displacement using the good micro-forming ability of BMGs would give rise to new MEMS functions and applications.

(2) BMGs are suitable for chemical applications such as fuel-cell separators (hydrogen permeable membranes for reformers used to separate hydrogen from gas mixtures) owing to their high strength, superior corrosion resistance, and viscous deformability. Owing to the required high corrosion resistance, Ni-based BMGs have been chosen from among the metal - metal systems for these types of applications. The corrosion rates of typical Ni-based BMGs in a diluted sulfuric acid solution (simulating actual PEMFC conditions around 368 K) are one order of magnitude lower than those of stainless steel (SUS316L).

Tests using a $\text{Ni}_{60}\text{Nb}_{15}\text{Ti}_{15}\text{Zr}_{10}$ BMG prototype fuel cell separator [15, 16] showed that it generated a high voltage at the actual operation current, with no degradation during a durability test conducted at a current density of 0.5 A/m^2 for 350 h.

(3) BMGs are suitable for magnetic applications such as power distribution transformers, linear actuators, choke coils, magnetic cores, high-frequency magnetic-shielding sheets, and so forth. A BMG produced from $\text{Fe}_{73}\text{Ga}_4\text{P}_{11}\text{C}_5\text{B}_4\text{Si}_3$ showed excellent soft magnetic properties ($J_s = 1.32 \text{ T}$; $\mu_{\text{max}} = 110,000$; $H_c = 3.3 \text{ A/m}$) that can be improved ($\mu_{\text{max}} = 160,000$; $H_c = 2.7 \text{ A/m}$) by annealing. Soft-magnetic BMGs with high permeability and low coercivity are appropriate materials for the magnetic yokes of such linear actuators [17]. Fe-based BMGs show high μ and low H_c values and are therefore appropriate for low-loss magnetic cores for choke coils [18].

(4) BMGs can be used in biomedical applications such as implants in the human body and surgical instruments. Glassy materials are highly biocompatible, inert (they should have a high corrosion resistance), and non-allergenic, which makes them particularly suitable for medical components. However, the mismatch of the modulus of elasticity (Young's modulus) between metallic parts and human tissues is still a problem that remains unsolved.

1.2. Deformation of metallic glasses

In conventional crystalline metals with long-range ordered atomic structures, plastic deformation is mediated by their well-defined defects, such as dislocations, causing the deformation to be initiated at a low energy level. However, the deformation of metallic glasses without long-range translational symmetry is mediated by local atomic rearrangement, referring to the direct process of the breaking and rebuilding of atomic bonds [19]. The exact nature of this local atomic motion accommodating shear strain in metallic glasses is not completely comprehended yet, but two different models of the fundamental unit in local atomic rearrangement have been proposed based on the free volume theory [20] and shear transformation zone (STZ) theory [21]. The metallic bonding characteristic of metallic glasses enables their atomic structures to be considered as a simplified hard-sphere model, as suggested by Bernal [22], compared to the complex bonding in covalent or ionic glasses. In this model, the atomic structure of metallic glass (or metallic liquid) is described as dense random packing of atomic hard spheres. A schematic illustration of the fundamental unit models for local shear transformation is shown in Figure 1.2.

In the atomistic view of metallic glass, the total volume of metallic glass can be separated into the volume occupied by atomic spheres and the vacant volume among the spheres ("free volume"

[23]). In the free volume theory [20] on the deformation of metallic glasses, a nearest neighbor environment with a relatively large free volume close to the atomic volume is the potentially preferred site for the diffusive jump of atoms, as shown in Figure 1.2 (a). The diffusive atomic jumps induced by shear stress leave behind flow defects with a relatively low packing density, resulting deformation-induced strain softening by mechanical dilatation. Although follow-up studies [24-26] have suggested that the deformation motion of metallic glass involves the cooperative motion of multiple atoms instead of single-atom motion in this model, the free volume model provides clear insight into the strain softening and shear localization of metallic glass at low temperatures while, also providing a quantitative analysis of the dilatation of metallic glass from the flow defect creation and annihilation process [24, 27].

Unlike a single-atomic diffusive jump in the free volume theory, a local cluster of atoms undergoing inelastic shear distortion (STZ) is regarded as the fundamental unit for the deformation of metallic glasses in STZ theory [19, 21], as shown in Figure 1.2 (b). Based on atomistic simulations and sheared bubble raft experiments [28], Argon introduced the concept of STZ as the spontaneous and cooperative reorganization of a small cluster of randomly close-packed atoms. According to this view, STZ is not an instant event defined in a local volume as compared to a structural defect in metallic glasses [19]. Computational modeling studied [26, 29, 30] and experimental

investigations [31-34] have estimated STZ size to be a few tens to a few hundred atoms, varying according to the simulated (or tested) alloy compositions and testing methods. Analogous to the diffusive jumps in free volume theory, the operation of STZ is also significantly affected by local atomic configuration (or the distribution of free volume).

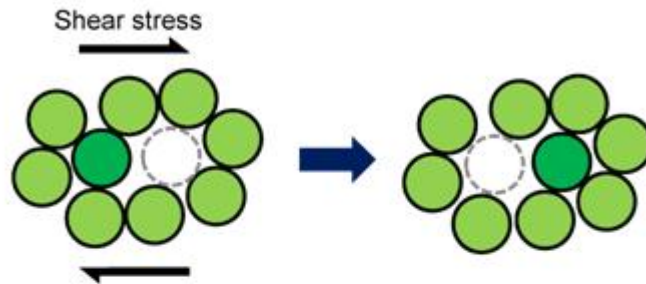
Although the free volume model and the STZ model adopt different atomic motions as the underlying mechanism of metallic glass deformation, these two distinct models share many common features that provide fruitful insights into the macroscopic deformation of metallic glasses [29]. The general equations of a macroscopic flow in both models can be expressed by Eq. 1.1, although the specific factors in the expression differ slightly depending on the model.

$$\dot{\gamma} = A \cdot \exp\left(-\frac{Q}{RT}\right) \sinh\left(\frac{\tau V}{kT}\right) \quad (\text{Eq. 1.1})$$

Here, $\dot{\gamma}$, τ , k and T are the shear strain rate, applied shear stress, Boltzmann constant, and temperature, respectively. Also, A is a proportional constant bearing the influences of the attempt frequency, the characteristic strain (γ_0), and the fraction of material deformed via the activated process (diffusive jumps or STZ operation). Here, Q is the characteristic activation energy of the corresponding processes in the models, and V is the characteristic volume, equal to "the product

of the characteristic strain and the STZ volume" for the STZ operation and "half of the atomic volume" for the diffusive atomic jump, respectively. The hyperbolic sine term in Eq. 1.1 originates from the consideration of forward operations of the processes competing with backward operations, implying the elastic response and cyclic deformation of metallic glass in the mechanisms of both models. The exponential term implies that both mechanisms are thermally activated such that the stress and flow characteristics of the deformation are significantly influenced by temperature. Both mechanisms also result in increased free volume (dilatation process) in the local volume, where the processes are activated. The accumulation of local dilatation leads to macroscopic mechanical behaviors such as strain softening and shear localization in metallic glass. In contrast to various atomistic mechanisms pertaining to the external conditions underlying the deformation of crystalline materials, the deformation of metallic glass is thought to be governed by a single mechanism, whether a diffusive atomic jump or STZ operation.

(a) Free volume theory



(b) Shear transformation zone (STZ) theory

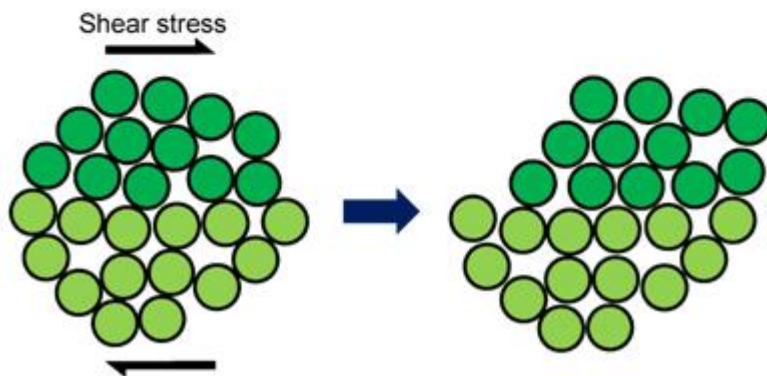


Figure 1.2 Schematic illustration of atomic shear transformation in metallic glasses. (a) Free volume mode and (b) Shear transformation zone (STZ) model. Recomposed from [20] with permission through the Copyright Clearance Center.

1.2.1. Deformation mode of metallic glasses

The temperature, stress, and strain rate affect the deformation response of metallic glasses as shown in the schematic deformation mechanism map in Fig. 1.3 as suggested by Spaepen [20]. At high temperatures (from the melting temperature downward to about T_g) and low strain rates the deformation is homogeneous. The glass deforms in a Newtonian viscous manner, whereas at lower temperatures and higher strain rates it becomes inhomogeneous and takes place via the formation of shear bands. As shown in Fig. 1.3, at low stresses, the viscous flow is initially supplanted by viscoelastic deformation and then by linear elastic deformation as the temperature is decreased. Viscous flowing, during which the strain rate scales linearly with the stress, is the dominant deformation mechanism at temperatures below T_g (i.e., $T < T_g$). Although the elastic moduli of metallic glasses do not differ greatly from those of oxide glasses, their propensity for viscoelastic deformation does. The viscoelasticity of metallic glasses is caused by recoverable atomic adjustments occurring in response to applied stress. Thus, it should be noted that atomic rearrangement in metallic glasses is relatively easy in comparison to oxide glasses owing to the atomic unit and the essentially non-directional bonding in the former.

In the inhomogeneous flow region, permanent deformation is confined to small shear bands. These bands have a thickness on the order of approximately 10 to 20 nm, and within such a band the shear

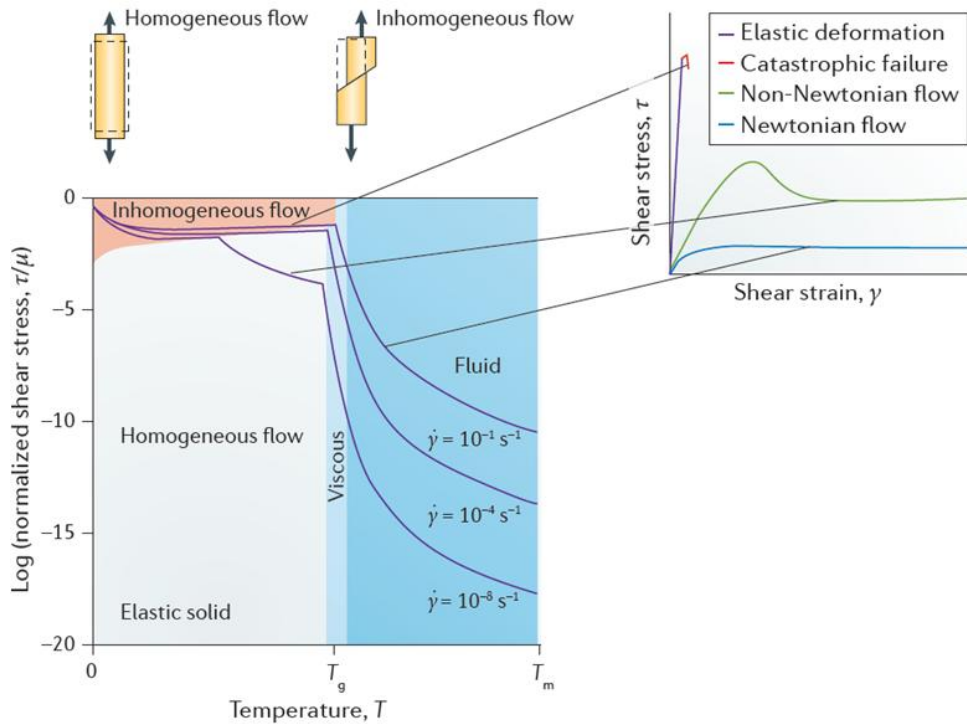


Figure 1.3 Schematic deformation mechanism maps for metallic glasses. Recomposed from [20] with permission through the Copyright Clearance Center

strain can be quite large. In tension testing, shear bands form at an angle relative to the tensile axis approximately equal to that corresponding to the maximum shear stress. The tensile flow behavior of metallic glass is also characterized by a yield point. That is, the stress required to propagate a band is less than that needed to initiate it. Tensile strength is, therefore, coincident with the development of the first shear band. Multiple bands can form if the stress state is not conducive to geometrical instability, as it is in a tensile test [35].

(1) Homogeneous Deformation: The homogeneous deformation of a metallic glass occurs when the operations of flow defects (diffusive atomic jump or STZ operation) are distributed homogeneously throughout the whole volume of the alloy; it is typically observed at temperatures near the glass transition temperature (T_g) of the alloy. As shown in Figure 1.4 (a), a metallic glass at elevated temperatures shows macroscopic volume (ΔV) expansion, which involves the influence of primary (α)- or secondary (β)-relaxations [36]. The thermally activated relaxation behaviors lead to the accumulation of locally dilated volume, and the metallic glass at temperatures near T_g has sufficient highly dilated local regions distributed homogeneously in the sample. This enables the spontaneous and homogeneous activation of flow defects throughout the sample and a macroscopic homogeneous plastic flow. Through homogeneous deformation at an

elevated temperature, the alloy can be elongated by more than 10,000% [37] as shown in Figure 1.4(b). The exceptional process ability of metallic glasses at elevated temperatures (especially in the supercooled liquid region) is applied in the thermoplastic forming technique for the precise processing of metallic glasses from the macroscale to the nanoscale [38].

Homogeneous deformation near or in the supercooled liquid region (the temperature region between T_g and T_x , where T_x is the crystallization onset temperature; Figure 1.4 (a)) shows a clear transition between Newtonian flow (with strain rate-independent viscosity) and non-Newtonian flow (with strain rate-dependent viscosity) behavior. In contrast, the samples compressed with a relatively high strain rate show stress-overshoot behavior before approaching steady-state conditions. The stress-overshoot phenomenon originates from the unbalanced condition of free volume creation and annihilation [27, 39] in a non-Newtonian flow. The hasty and excessive creation of a free volume occurs at the initial deformation stage until the peak stress induces softening (a decrease in the flow stress) and the material gradually approaches steady-state conditions.

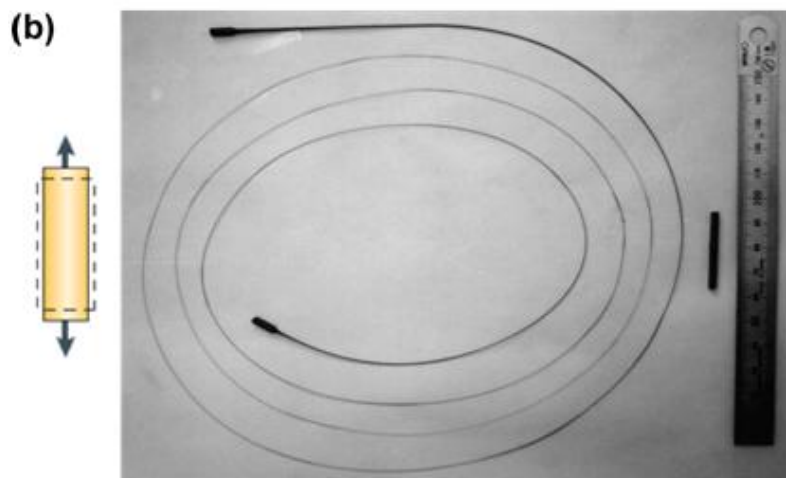
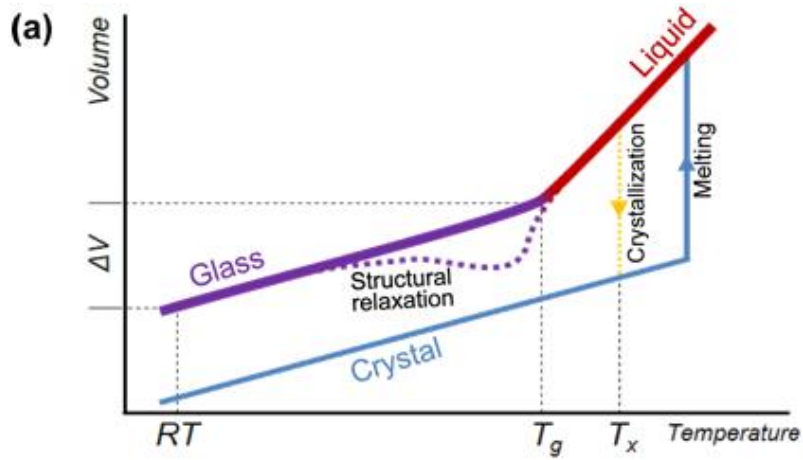


Figure 1.4 (a) Volume-temperature relationship in transformation among liquid, glass, and crystal. (b) La-Al-Li metallic glass homogeneously deformed to 20,000% in the supercooled region. (b) is recomposed from [37] and [40] with permission through the Copyright Clearance Center.

(2) Inhomogeneous Deformation: In contrast to the homogeneous deformation of metallic glass at an elevated temperature discussed in the previous section, the macroscopic plastic deformation of metallic glass at low temperatures near room temperature is mediated by thin band-shape instabilities accommodating largely concentrated shear strains, termed "shear bands". The spontaneous shear localization to form shear bands in metallic glasses originates from the shear softening nature of the alloys. If a local volume in a metallic glass sample is plastically deformed through local shear transformation, it also undergoes dilatation and become softer than the surrounding undeformed regions, which eventually results in the self-focusing concentration of plastic strains into a thin shear band in the direction of the maximum shear stress. After initiation, shear bands generally operate very rapidly and can accommodate displacement apparently up to nearly the millimeter scale [41]. They are generally considered a major cause of the extremely limited plasticity of metallic glass. Therefore, the control of shear bands to induce multiple instances of nucleation and to block their rapid propagation has attracted an enormous amount of research interest to improve the plasticity of metallic glass [40, 42].

Various summaries of shear band formation have been suggested based on theoretical considerations and computational simulations [43-45]. One such scenario is introduced here, focusing on the intrinsic structural inhomogeneity of metallic glasses as an origin

of shear band initiation [44], rather than pre-existing extrinsic flaws or casting defects [43]. When a sufficiently large population of STZs is homogeneously activated in a metallic glass matrix under high stress, the STZs will eventually exceed the percolation limit, with the percolated STZs then forming a thin band in an intensively dilated state along the direction of the maximum shear stress (Figure 1.5 (a)). Subsequently, shear strains would be highly concentrated in the softened band-shape region rather than in the relatively dense and hard surrounding regions, resulting in the rapid development of the band into a mature shear band with a thickness of a few tens of nanometers (Figure 1.5 (b)).

In comparison to conventional crystalline metals, metallic glass exhibits lower Young's modulus values and higher elastic strain limits (~2%), indicating that they are remarkably more capable of storing elastic strain energy per unit volume (i.e., resilience). The enormous elastic strain energy which can be stored in metallic glass during loading up to the yield point is released by yielding through the small volume fraction of the alloy within the shear bands, causing a substantial temperature increase. Evidence of a temperature increase in the shear bands is often observed in metallic glass in the form of vein patterns from a liquid-like shear flow on the fracture surface [46] and fractures accompanied by sparking [47]. There is also evidence obtained by direct thermographic measurements [48, 49]. However, the alternative concept of "cold" shear bands was suggested recently in

contrast to "hot" shear bands with substantially elevated temperatures [50, 51]. From the precisely displacement-controlled testing of the compressive deformation of bulk metallic glass samples, it was reported that the dominant shear band can operate in a stick-slip manner and that these acceleration-deceleration cycles of shear band sliding cause only negligible increases in the temperature [45, 52, 53]. Because hot shear bands generally develop with runaway instability, the controlled and serrated sliding of the major shear band is also an significant condition for multiple shear bands potentially to contribute to plastic deformation. Thus, insights cold shear bands as well as hot shear bands provides physical understanding into the shear instability processes and offers useful information for those attempting to improve the plasticity of metallic glass [54].

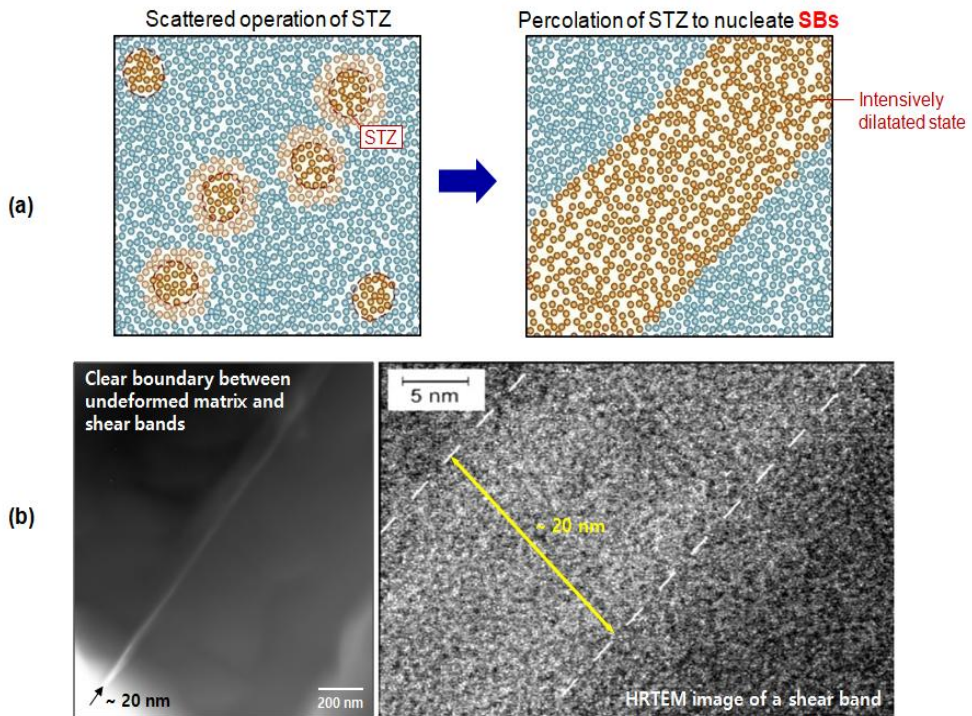


Figure 1.5 (a) Schematic illustration of the initial process of a shear band. (b) High-resolution TEM image of shear band formation during bend testing of $\text{Fe}_{79.3}\text{B}_{16.4}\text{Si}_4\text{C}_{0.3}$ metallic glass ribbon. Recomposed from [54] with permission through the Copyright Clearance Center.

1.2.2. Plastic deformation of metallic glasses

Metallic glass materials have attracted tremendous levels of interest with regard to structural applications due to their excellent mechanical properties, such as (i) high strength much closer to the theoretical limit compared to their crystalline counterparts, (ii) a large elastic strain limit of approximately $\sim 2\%$ as compared to a limit of approximately $\sim 0.2\%$ for crystalline materials, and (iii) exceptional fracture toughness ranging from highly brittle to extremely tough. On account of their remarkable combination of mechanical properties, those materials possess a unique status among structural materials, as briefly summarized in Figure 1.6 [55].

However, metallic glass does not exhibit ductility because these materials do not contain any dislocations or slip planes. The limited macroscopic plastic deformability of BMGs is correlated with highly localized deformation processes, such as shear banding, where a high amount of plastic strain is accumulated in a very thin region exhibiting strain softening/thermal softening behavior [48]. Although the local plastic strain in a shear band is very high, the overall room-temperature plastic deformability is disappointingly low [56]. A critical issue in the relation to the utilization of BMGs is, therefore, to improve their plasticity and to modify their microstructure to address the brittleness problems. When BMGs undergo extensive deformation, they show traces of many shear bands. The guiding principle thus far has been to facilitate the formation of multiple

shear bands so that the strains do not become concentrated in one or a few shear bands and thus cause enormous problems, not the least of which by evolving into cracks.

- (+) Exceptional yield strength

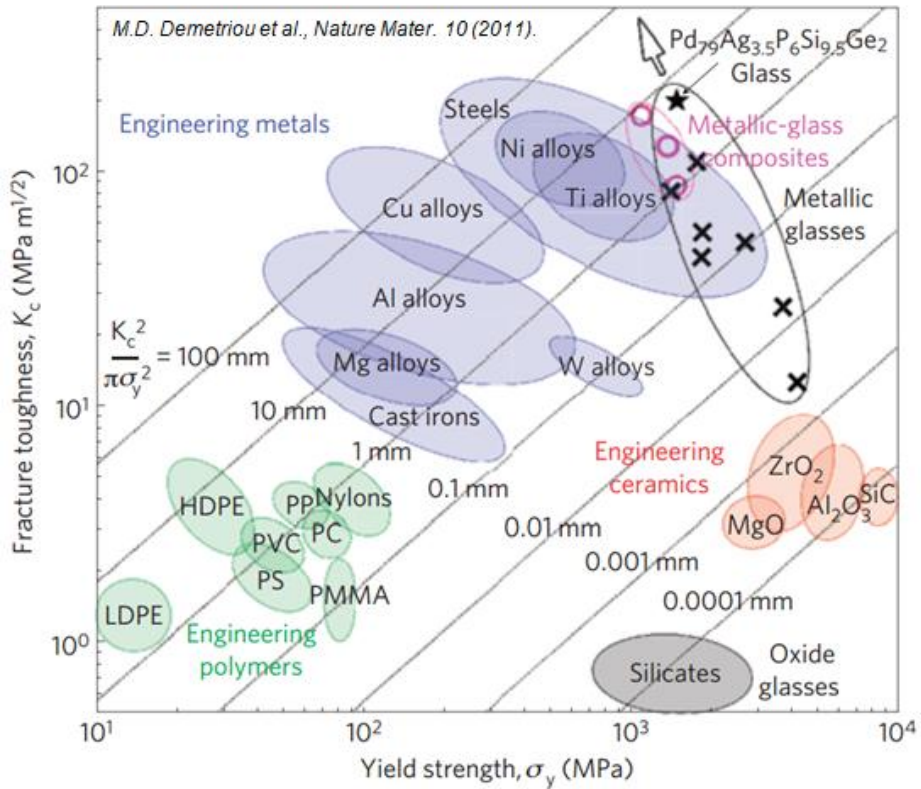


Figure 1.6 Ashby map of fracture toughness versus strength of materials. Reprinted from [55] with permission through the Copyright Clearance Center.

1.3. Improvement of plasticity of bulk metallic glasses

A composite is defined as any material that consists of two or more materials deliberately integrated to form heterogeneous structures with desired or purposed properties [57]. Composite materials are desirable because, by combining materials, it is possible to obtain properties that no single material can provide. In traditional metallurgy, a suitable matrix can be the only basis necessary upon which to optimize the microstructure and properties through the dispersion of a second phase. This is also the case with metallic glass. BMGs with a composite microstructure, consisting of a crystalline and amorphous phase, show better performance under mechanical stress than monolithic glass materials. The second crystalline phase, such as powders, particles, fibers, or in-situ formed precipitates distributed in the amorphous matrix, may act as initiation sites for shear bands, resulting in the formation of multiple shear bands throughout the specimen and possibly restricting the propagation of shear bands.

BMG composites are designated as in-situ or ex-situ composites depending on the manner in which they are obtained, as briefly summarized in Figure 1.7. In in-situ composites, the second phase precipitates out of the metallic glass either during casting or the subsequent processing of the fully glassy alloy. Accordingly, the interface between the matrix and the crystalline reinforcement is very

strong. Whereas, in the ex-situ method, the reinforcement phase is added separately during the casting/processing of the alloy and remains “as-is” without highly interaction with the matrix. Consequently, the link between the matrix and the reinforcement may not be very strong. Moreover, the volume fraction of the reinforcement phase is smaller in the in-situ method and could be much higher in the ex-situ method.

1.3.1. Ex-situ formed bulk metallic glass composites

The ex-situ method of making the BMG composites is very important because allows the introduction of a very large volume fraction of the second crystalline phase. The types of reinforcements used are pure metals (titanium, copper, tungsten, molybdenum, and nickel), alloys (1080 steel, brass, and stainless steelss), and nonmetallic materials (SiC, graphite and diamond). Long and continuous fibers, whisker, and particulates are used. Particulates and short fiber are added directly to the melt and composites are produced. However, in the case of long and continuous fibers, the melt infiltration technique is most normally used.

1.3.2. In-situ formed bulk metallic glass composites

In-situ composites are usually developed by modifying the chemical composition of the alloy. When the alloy composition is chosen in that manner that it does not correspond precisely to the

actual glass-forming composition, the product of solidification will not be a homogeneous glassy phase. Instead, a crystalline phase will coexist with the glassy phase. This process has been applied in a number of cases to produce in-situ composites [58 - 62]. In this method, the alloy is melted and cast directly into the mold. If the composition digresses substantially from the glass-forming composition range, the second (crystalline) phase forms, and its volume fraction is determined by the extent of deviation from the glass-forming composition range. The shape of the crystalline phase is usually dendritic because it forms directly from the melt. Instead of directly casting from the liquid state, if the alloy is homogenized in the semiliquid (liquid + solid) region and then cast, the crystalline phase obtained will have a spherical shape [61], and this is expected to enhance the mechanical properties. If the second phase is obtained during subsequent processing of the fully solidified casting, the microstructure of the phase can be controlled. The grain size and shape of the second phase may differ. For example, if the glassy alloy is annealed at a low temperature, the grain size of the crystalline phase will have nanometric dimensions [63]. Thus, there are various methods to obtain the proposed size and shape and volume fraction of the reinforcement phase through this way.

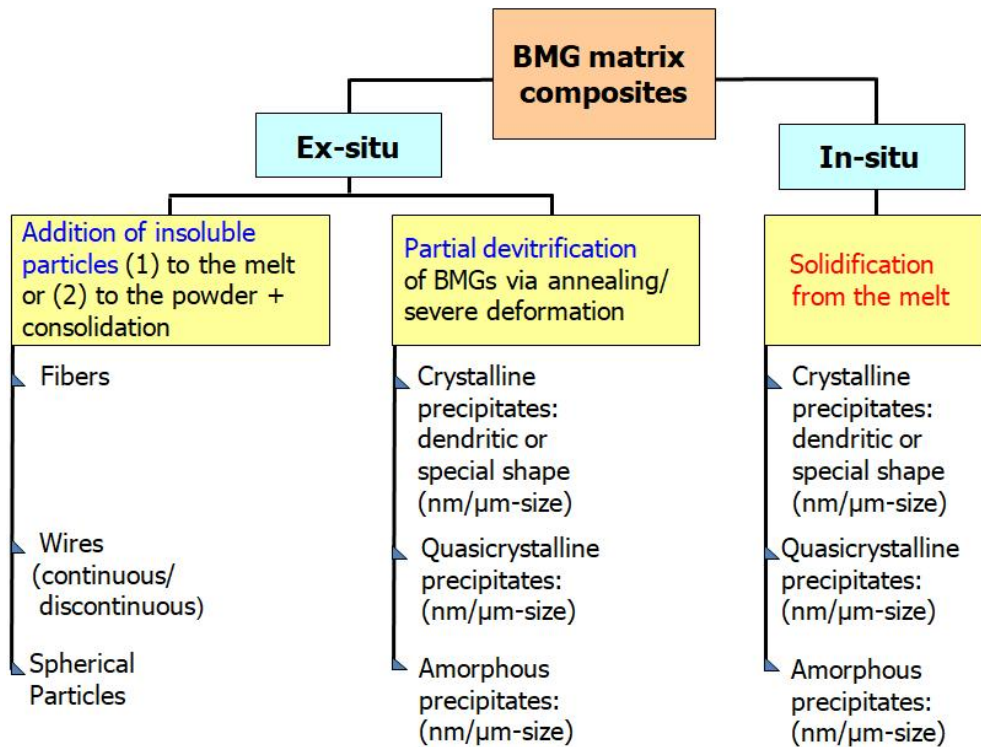


Figure 1.7 Various methods of producing BMG matrix composites to improve of plasticity in BMGs

1.4. Phase separation in metallic glasses

Given that metallic glasses materials are thermodynamically unstable, they undergo structural changes during cooling from liquid melts or during heating from the frozen-in glassy state [64]. From this viewpoint, phase separation in metallic glass can occur by (i) liquid - liquid separation during cooling from the liquid melts or (ii) by solid-state separation in frozen-in glass during heating. Earlier reports [65-70] on phase separation in metallic glasses mostly have dealt with the latter, while the occurrence of phase separation in frozen-in glass (having only negative mixing enthalpies among the constituents) during heating is questionable [64]. In contrast to the separation in frozen-in glass, clearly-separated two-glass structures in metallic glasses have been widely reported in the alloy systems with an intentionally-included atomic pair with a large positive enthalpy of mixing [64, 71-80].

It is well known that an atomic pair with a large positive enthalpy of mixing relationship forms a miscibility gap with high critical temperatures (\sim binodal line) in the equilibrium binary system. Moreover, liquid-state phase separation can occur at temperatures exceeding the liquidus temperature when the composition of a melt is in the miscibility gap. However, the relationships between large negative mixing enthalpy among the constituent elements are generally favorable for stabilizing the liquid phase and securing high

glass-forming ability (GFA) in an alloy [81]. An alloy with an atomic pair with a large positive enthalpy of mixing relationships would likely show deterioration of the GFA; moreover, phase separating metallic glass materials can be designed by enhancing the GFA of each separate liquid phase with the aid of additional alloying elements. Kündig et al. [79] was the first to report a two-amorphous-phase structure formed by liquid-liquid phase separation during cooling from liquid melts in the La-Zr-Al-Cu-Ni system with a large mixing enthalpy relationship between La and Zr. Two quaternary systems inside the quinary system, La-Al-Cu-Ni and Zr-Al-Cu-Ni, have good glass-forming abilities, and their combination enables the liquid-state phase separation during cooling from the melt into La-rich and Zr-rich phase with sufficient glass-forming ability for solidification into an amorphous state by rapid quenching (e.g., melt-spinning). An example of a La-Zr-Al-Cu-Ni as-spun ribbon is shown in Figure 1.8 (a), and the phase-separated amorphous structure can be directly observed by electron microscopy. From analogous alloy designs, various types of phase separating metallic glass have been reported in several alloy systems, such as Y-Ti-Al-Co [77, 82], Cu-Zr-Al-Y [80], Nd-Zr-Al-Co [78], Ni-Nb-Y [74, 83], Gd-Ti-Al-Co [84], Gd-Hf-Co-Al [71], Cu-Zr-Al-Gd [72], Gd-Zr-Al-Ni [73] and Zr-Gd-Co-Al [76].

These phase separating metallic glass materials exhibit some unique characteristic due to their unusual dual-amorphous structure

with distinct chemistry. Park et al. [80] reported that the precise control of amorphous heterogeneity in Cu-Zr-Al-Y phase separating metallic glasses into atomic scale can enhance the plasticity of the alloys by affecting local viscous flow behavior during shear deformation. Nd-Zr-Al-Co [78] and Gd-(Hf,Ti,Y)-Co-Al [85] phase separating metallic glasses were reported to show some unique magnetic behavior depending on the shape of the separated amorphous phases. Moreover, phase separating metallic glasses can be used as precursor materials for a dealloying process (selective dissolution) for fabricating multi-component amorphous nanoparticles [86] and nanofoam materials [87]. This is also the main concern of this study with regard to the applications of phase separating metallic glasses.

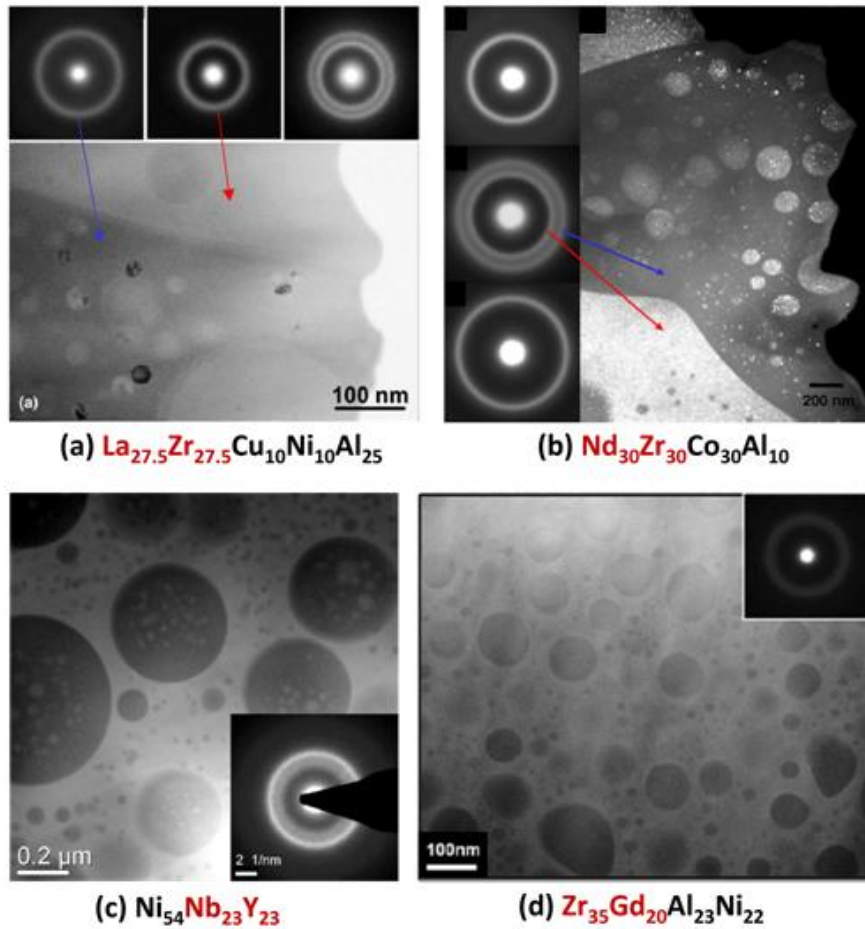


Figure 1.8. TEM images of phase separating metallic glasses (a) $\text{La}_{27.5}\text{Zr}_{27.5}\text{Cu}_{10}\text{Ni}_{10}\text{Al}_{25}$. (b) $\text{Nd}_{30}\text{Zr}_{30}\text{Co}_{30}\text{Al}_{10}$. (c) $\text{Ni}_{54}\text{Nb}_{23}\text{Y}_{23}$. and (d) $\text{Zr}_{35}\text{Gd}_{20}\text{Al}_{23}\text{Ni}_{22}$. The image shown in (b) is a dark-field image, while the others are all bright field images. The insets are selected diffraction patterns(SADP) corresponding to each observed regions. Reprinted from [73, 74, 78] and [79] with permission through the Copyright Clearance Center.

1.4.1. Thermodynamic background phase separation

This section provides a brief thermodynamic description of the stability condition for a multicomponent system [64, 88] (as in typical phase separating metallic glass materials). For a closed system at constant temperature T and pressure P , the criterion of equilibrium is given by the minimization of the Gibbs free energy.

$$(\delta G)_{P,T,n_i} \geq 0 \quad (\text{Eq. 1.2})$$

where n_i is the number of moles of component i in a multi-component system. Hancock [89] demonstrated that the criterion of stability for a multicomponent liquid with respect to infinitesimal composition fluctuations at constant T and P values can be expressed in terms of the conditions of the following diagonal determinants:

$$G_{11} \geq 0 \quad (\text{Eq. 1.3})$$

$$\begin{vmatrix} G_{11} & G_{12} \\ G_{21} & G_{22} \end{vmatrix} \geq 0 \quad (\text{Eq. 1.4})$$

$$\begin{vmatrix} G_{11} & G_{12} & \cdots & G_{1m} \\ G_{21} & G_{22} & \cdots & G_{2m} \\ \vdots & \vdots & & \vdots \\ G_{m1} & G_{m2} & \cdots & G_{mm} \end{vmatrix} \geq 0 \quad (\text{Eq. 1.5})$$

The last condition is trivial, as the determinant in Eq. 1.5 associated with the G_{ij} matrix is always null when applying the

Gibbs-Duhem equation:

$$n_1 G_{1i} + n_2 G_{2i} + \dots + n_m G_{mi} = 0 \quad (\text{Eq. 1.6})$$

The stability condition also can be expressed using the stability function ψ in terms of the molar Gibbs free energy G_m of the system and the mole fraction of component i ($X_i = n_i / \sum n_i$), as follows:

$$\psi = \begin{vmatrix} \frac{\partial^2 G^m}{\partial X_2^2} & \dots & \frac{\partial^2 G^m}{\partial X_2 \partial X_i} & \dots & \frac{\partial^2 G^m}{\partial X_2 \partial X_m} \\ \vdots & & \vdots & & \vdots \\ \frac{\partial^2 G^m}{\partial X_i \partial X_2} & \dots & \frac{\partial^2 G^m}{\partial X_i^2} & \dots & \frac{\partial^2 G^m}{\partial X_i \partial X_m} \\ \vdots & & \vdots & & \vdots \\ \frac{\partial^2 G^m}{\partial X_m \partial X_2} & \dots & \frac{\partial^2 G^m}{\partial X_m \partial X_i} & \dots & \frac{\partial^2 G^m}{\partial X_m^2} \end{vmatrix} \geq 0 \quad (\text{Eq. 1.7})$$

If $\psi > 0$, the liquid is stable, and any small composition fluctuations will decay back reversibly with time. If $\psi < 0$, however, the liquid is unstable and cannot be persistent against infinitesimal composition fluctuations. It will then undergo phase separation by spinodal decomposition. The spinodal composition can be determined by the criterion $\psi = 0$. If the G_m value of a system is given in terms of the mole fraction, with the stability function, it can be determined whether the liquid is stable against an infinitesimal fluctuation in the

composition (spinodal decomposition) or not. For a simplified binary system consisting components A and B, the molar Gibbs free energy can be written as follows:

$$G_m = X_A G_A^0 + X_B G_B^0 + \Delta G^{mix} \quad (\text{Eq. 1.8})$$

$$\Delta G^{mix} = \Delta H^{mix} - T\Delta S^{mix} \quad (\text{Eq. 1.9})$$

When $\Delta H^{mix} \gg 0$, the region of instability (range between points a and d in Figure 1.9 (a)) appears at low temperatures (e.g. $T = T_2$), where the ΔH^{mix} term becomes dominant relative to the $T\Delta S^{mix}$ term, while the region of immiscibility vanishes at high temperatures over a critical temperature, T_c . The stability function in the binary solution can be expressed by the reduction of Eq. 1.9 as follows:

$$\psi = \frac{\partial^2 G^m}{\partial X_2^2} \geq 0 \quad (\text{Eq. 1.10})$$

This means that spinodal decomposition occurs between the inflection points (between points b and c in Figure 1.9 (a)). The miscibility gap (binodal curve) and spinodal curve in a temperature-composition space (Figure 1.9 (b)) can be delineated from the equilibrium compositions and inflection points in the curve,

respectively, depending on the temperature. The practical shapes of miscibility gaps are generally asymmetrical, unlike the idealized case shown in Figure 1.9 (b). To express the molar Gibbs free energy and Gibbs free energy change with mixing in a multi-component system with immiscibility near that in practical cases, various models have been suggested with extended consideration of complex configurations in the system [88]; these solutions can be used for the thermodynamic calculation of the miscibility gap.

Chang et al. [84] assessed the existence of a miscibility gap and spinodal curve in a Gd-Ti-Al-Co quaternary system through description of the Gibbs free energies of liquid solution phases by the sub-regular solution model using the Redlich - Kister formula [90]. They succeeded in evaluating the Gibbs free energy surface of a multi-component system at partial compositional sections of a quaternary phase tetrahedron, suggesting a pseudo-binary section of the miscibility gap between two ternary compositions of Gd-Al-Co and Ti-Al-Co. The thermodynamic assessment of the miscibility gap and spinodal line in phase separating metallic glass materials provides fruitful information with regard to controlling the phase-separated structure through manipulation of the compositional and kinetic variables in the alloying and casting process. This will be intensively investigated in Chapter 3.3.

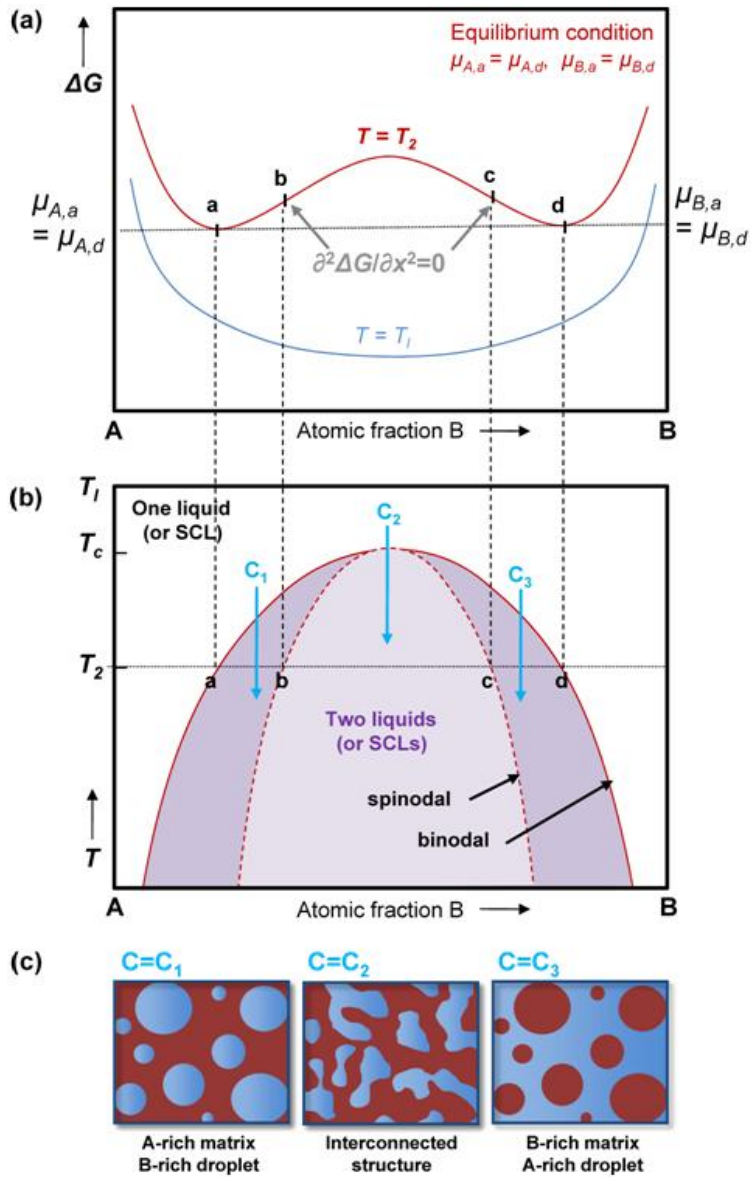


Figure 1.9. Schematic illustration of (a) Gibbs free energy change by mixing (ΔG^{mix}), (b) miscibility gap in binary system, and (c) microstructure formed by phase separation during on the compositions of alloy melt.

1.4.2. Mechanism of phase separation

If a stable alloy melt at a high temperature over $\sim T_c$ penetrates into the miscibility gap by cooling, the mixture of two liquid phases can be more stable than a homogeneous single liquid phase, and some of these fluctuations can irreversibly grow to decrease the Gibbs free energy, as indicated in Figures 1.9 (a) and (b). The miscibility gap can be split up two regions, a region between the binodal and spinodal lines (metastable) and the other inside the spinodal line (unstable). In the metastable region, an infinitesimal composition fluctuation is involved by an increase in the Gibbs free energy, which will reversibly decay. To separate a homogeneous liquid phase into two liquid phases with equilibrium compositions to minimize the Gibbs free energy, the process should overcome the energy barrier for nucleation. Therefore, the typical phase-separation mechanism in this metastable region can be explained by “nucleation and growth” (Figure 1.10 (a)). In this mechanism, phase separation is initiated by the formation of energetically stable solute-rich domains (nuclei), which require large thermal fluctuations to overcome the nucleation energy barrier. The energy barrier originates from the formation of a distinct interface between the nuclei and the surrounding matrix by nucleation. After the formation of nuclei over a critical size, phase separation proceeds via the growth of those nuclei through diffusion of the solute from the matrix. From the beginning of the phase separation process (nucleation), droplet phases

have compositions that largely differ from the matrix composition. The resulting droplet microstructure shows a homogeneous distribution of spherical droplet phases in the matrix.

In the unstable liquid region within the spinodal line, phase separation takes place through spinodal decomposition via up-hill diffusion (Figure 1.10 (b)), and infinitesimal fluctuations do not reversibly decay. Instead, the fluctuations extend spatially and irreversibly without energy barriers to overcome. Therefore, spinodal decomposition does not occur in a thermally activated process, and it spontaneously proceeds as the continuous growth of composition fluctuation through inverse (up-hill) diffusion against the concentration gradient to reduce the Gibbs free energy. The probability of infinitesimal fluctuations is homogeneously distributed throughout the alloy melt and the amplitude of composition fluctuations continuously grows. According to Cahn's linearized theory [91], especially in the early stage of decomposition, the concentration fluctuation with a particular dominant wavelength grows exponentially with time only in terms of the amplitude, corresponding to maximum growth rate [64]. Depending dominantly on the undercooling and diffusivity of the constituting elements, only a single Fourier component among the assorted fluctuation wavelengths survives, especially at the early stage of spinodal decomposition, and this component governs the characteristic scale length of the fluctuating domains. At this stage, the phase domains have no clear interface and show a unbroken

network structure with hyperbolic interfaces, characterized by negative Gaussian curvature having both concave and convex instances of curvature. With an increase in the concentration difference between the two phase domains, the interfacial energy corresponding to the gradient energy increases. To reduce the total interfacial energy of the system, coarsening of the domain structure takes place. Depending on the diffusivity and viscosity of the molten melt, different growth mechanisms are expected to dominate the coarsening kinetics, resulting in various morphologies of phase separated metallic glasses. The well-defined interconnected structure of spinodal decomposition is a transient structure, which self-similarly coarsens for a limited duration and consequently breaks into fragmented structures.

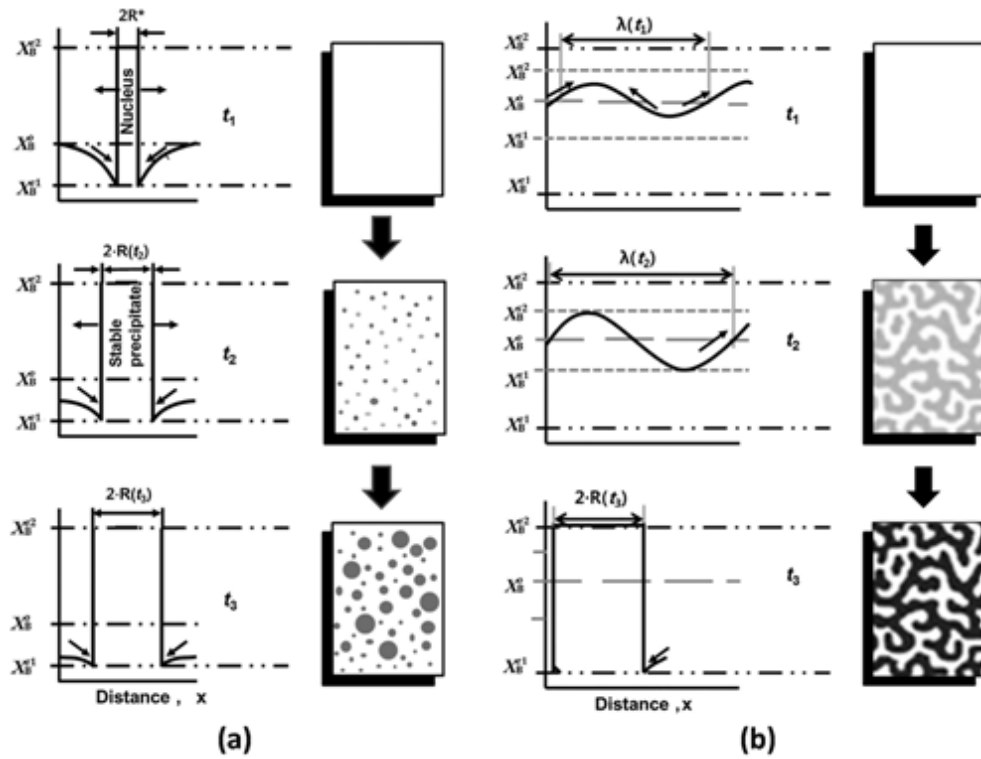


Figure 1.10. Schematic diagrams showing spatial variations in concentration variation and morphology evolution ($t_1 < t_2 < t_3$) during phase separation by two different mechanisms: (a) nucleation and growth and (b) spinodal decomposition. Reprinted from [64] with permission through the Copyright Clearance Center.

1.5 Additive manufacturing

1.5.1. Type of additive manufacturing

Additive manufacturing (AM) technology is defined as the process of joining materials to make parts from 3-dimensional model data, usually layer upon layer, as opposed to conventional manufacturing and formative manufacturing methodologies in the ISO/ASTM 52900-15 standard. Several Additive manufacturing technologies have been commercialized, and they are classified into the seven standard technologies as summarized in Table. 1.1.

Regardless of the Additive manufacturing technology, physical 3-dimensional parts are fabricated from digital 3-dimensional models. In detail, the Additive manufacturing part fabrication procedure is presented in Fig. 1.11. 3-dimensional models are obtained from either CAD software or reverse engineering tools. Topology optimization and a lattice structure can be extensively applied owing to the layer-wise manufacturing principle. Part functionality and structural properties are simulated through computer-aided engineering, and the optimized 3-dimensional model is converted into printable file formats, such as STL or AMF with error correction. Support, orientation, and multiple parts packaging are conducted. Subsequently, the STL file is sliced and the G-code is generated. Parts are built by selected additive manufacturing technology: the process can be monitored and analyzed in-situ, and feed-back can be provided. Additive manufacturing parts

do not meet industrial requirements; however, post-processing and post-additive manufacturing processes are applied to improve the quality and properties of the fabricated parts.

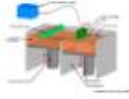
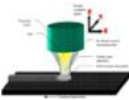

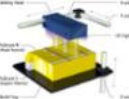

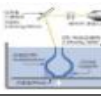

Standard Classification	Definition	Feedstock
Binder jetting 	A liquid bonding agent is selectively deposited to join powder materials	Polymer Ceramic Metal
Directed Energy Deposition 	Focused thermal energy is used to fuse materials by melting as they are being deposited	Polymer Metal
Material extrusion 	Material is selectively dispensed through a nozzle or orifice	Polymer Ceramic Polymer composite
Material jetting 	Droplets of build material are selectively deposited	Polymer
Powder bed fusion 	Thermal energy selectively fuses regions of a powder bed	Polymer Metal
Vat photo-polymerization 	Liquid photopolymer in a vat is selectively cured by light-activated polymerization	Polymer composite
Sheet lamination 	Sheets of material are bonded to form a part	Polymer Metal

Table 1.1 Standard classification of additive manufacturing (Ref. from [92])

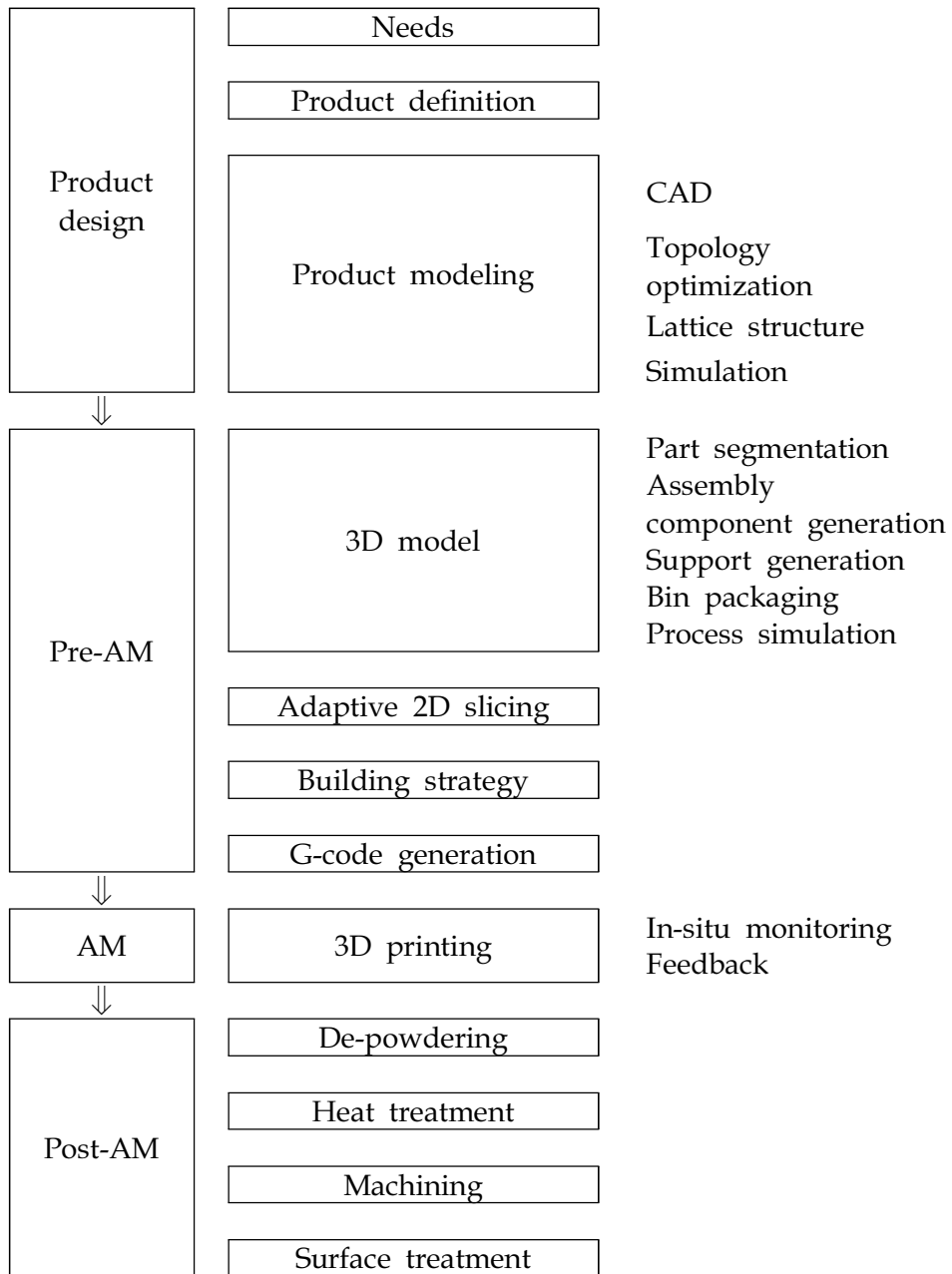


Figure 1.11. Part fabrication through additive manufacturing technology.

1.5.2. Metal additive manufacturing

In addition to the standardized classification, additive manufacturing technology is classified in terms of the material feedstock used. Examples include the polymer additive manufacturing, ceramic additive manufacturing, metal additive manufacturing, and composite additive manufacturing types. Among them, metallic parts are fabricated from metallic feedstock in metal additive manufacturing. Commercialized metal additive manufacturing technologies are summarized in Table 1.2.

Powder bed fusion additive manufacturing, directed energy deposition additive manufacturing, sheet lamination additive manufacturing, and binder jetting have all been commercialized. As shown in Fig. 1.12, the processing temperature and feedstock change among additive manufacturing processes. Pre-placed metal foil is bonded to a pre-patterned layer through ultrasonic welding. Vibrational energy imparts friction at the interface, and solid-state mechanical bonding is successfully achieved [93]. After bonding, a 2-dimensional pattern is obtained by laser cutting. One advantage of metal sheet lamination additive manufacturing is that it can be easily used to build complex composite products, such as those with a multi-layer structure and a wire-embedded architecture. Metallic wires can be used for directed energy deposition additive manufacturing. Wire raw material is externally fed into a molten pool, which is locally generated by high density energy sources, such as a laser,

electron beam [94], or transferred arc [95]. Multiple wires are utilized alternately or simultaneously. Diverse consolidation mechanisms are used in powder based metal additive manufacturing. Melting and solidification are used for both powder bed fusion additive manufacturing and directed energy deposition additive manufacturing. Solid-state consolidation through solid-state sintering process or liquid phase sintering process is also made for powder bed additive manufacturing. In the case of binder jetting additive manufacturing, powders do not seriously undergo a thermal cycle but are bound together using an externally supplied adhesive binder. As-built products obtained by the subsequent melting and solidification route result in near-full density (~ 100% densification); however, thermally induced distortion, defective microstructures, and anisotropic microstructures need to be carefully manipulated. Solid-state consolidation of powder bed additive manufacturing can be accomplished through solid-state sintering process or liquid phase sintering process. Selective laser sintering and hot isotropic pressing are potential cases of solid-state sintering processes. Various binary powder systems consisting of a base metal powder and an additive metal powder with a lower melting point are used for liquid phase sintering processing. During the laser irradiation cycles, the process of the melting, spreading, and solidification of the lower melting point additive metal powder results in consolidation of the base metal powder as in conventional liquid phase sintering process. However, a

time constraint within several micro-seconds can be applied in additive manufacturing technology. Otherwise, porous additive manufacturing primitives fill the lower melting point secondary phase through a post pressure-less or pressurized infiltration process. In the case of Al-AlN composite fabrication, binder burn-out and nitridization of an SLS primitive precede the infiltration of molten Al. Binder jetting metal additive manufacturing utilizes solid-state consolidation. The binder is added onto the surface of pre-placed powders in the powder bed and then infiltrates into the powders. Polymerization of the binder then successively consolidates the powders. In most cases, binder jetting additive manufacturing primitives undergo the same post-processing steps as a metal powder injected green body, localized binder burn-out and sintering process. In Table 1.3, the characteristics of typical metal additive manufacturing processes are summarized. Full density 3-dimensional products are successfully manufactured by these processes, except for binder jetting additive manufacturing. It still takes a substantial processing time to build products, and further improvements in the properties of the as-built products are essentially required [92].

Standard Classification	Consolidation Mechanism	Feedstock	Energy Source
Powder Bed Fusion	High energy density rays are scanned on pre-placed powder layer. Melting-solidification is primary consolidation mechanism	Powders	Laser e-Beam
Directed Energy Deposition	Powders or wires are melted with laser, e-beam, or arc, Molten feedstock is selectively deposited and solidified to form 3D parts	Powders Wires	Laser e-Beam Arc
Binder Jetting	Binding agent is selectively dropped on pre-placed powder layer. Adhesive bonding is consolidation mechanism	Powders	-
Sheet Lamination	Sheet feedstock is bonded and 2D pattern is generated by laser cutting, Friction welding by ultrasound is joining mechanism	Sheets	Ultra-sound

Table 1.2. Commercialized metal AM technologies

Process temperature	T_m	Metallurgical bonding (melting-solidification)	Powder bed fusion Directed energy deposition	
	$0.5T_m$	Metallurgical bonding (sintering)	Powder bed sintering	
	RT	Mechanical/chemical bonding (material flow/adhesion)	Cold spraying/ Binder jetting	Sheet lamination
			POWDER	WIRE

Figure 1.12. Metal additive manufacturing process according to feedstock dimension and process temperature.

ASTM	Process (Maker)	Process time *	Properties		
			Accuracy (mm)	Relative density (%)	Surface roughness (Ra/um)
Binder Jetting	Digital part materialization (ExOne)	10 hours	+/- 2.0	> 95	~ 9
Powder Bed Fusion	Electron beam melting (Arcam AB)	12 hours	+/- 0.2	> 99	~ 20
	Directed metal laser sintering (EOS)	24 hours	+/- 0.05	> 99	~ 9
Directed Energy Deposition	Laser engineered net shaping (Optomec)	10 hours	+/- 0.125	> 99	~ 25
Sheet Lamination	Ultrasonic additive manufacturing (Fabrisonic LLC)	24 hours	+/- 0.015	> 99	~ 7

Table 1.3. Comparison of metal additive manufacturing process(*
Process time : time generally required for making
125×125×125 mm³ cubit product)

1.5.3. Powder bed fusion additive manufacturing

Powder bed fusion (PBF) additive manufacturing technology is commonly used because it is easy and complete, and it offers the ability to form net-shaped structures during the fabrication of complex 3D parts. Metal PBF utilizes the melting-solidification reaction as the consolidation mechanism during full-density part fabrication. A laser or e-beam is used as the energy source. In the case of laser PBF, a high energy density laser is scanned across the powder bed by either a galvano-mirror system or an overhead gantry system. The ray interacts with powders in the powder bed, and the absorption and reflection of the ray by the powders is well described by the ray-tracing model [96]. Single-pass laser scanning results in a weld, as schematically illustrated in Fig. 1.13 (a). This type of weld is composed of the weld metal, the heat-affected zone, and the base metal, and the structure of the weld varies according to the applied thermal cycles and corresponding microstructural evolutions. As the laser directed at the powders moves, the powders are rapidly heated and melted during a heating cycle, after which the molten pool is solidified to form weld metal during the cooling cycle. The microstructural evolution of weld metal is largely dependent on the temperature gradient and solidification rate. A weld metal microstructure map of conventional alloys is shown in Fig. 1.13 (b). In general, the cooling rate of a molten pool, which is the product of the temperature gradient and solidification rate, ranges from 10^4 K/s

to 10^8 K/s [97]. This is far faster than the cooling rates of conventional manufacturing technologies based on melting solidification. As the directed laser source moves, a bead is generated on the powder layer of the previously built part of the surface which is covered with powder. The bead shape is largely dependent on the laser parameters. Balling triggered by Plateau-Rayleigh instability is problematic [98]. The formation of a ball-like weld deteriorates the morphology of the fabricated part and leads to the formation of defective microstructures.

The building of parts by PBF additive manufacturing is regarded as fusion welding with overlapping multi-pass laser irradiation on the powder layer. The single pass weld bead morphology depends on the energy density of the laser and the powder packing density. Among various energy densities, the volumetric energy density (E_v) and linear energy density (E_L) are usually used as measures of the heat input,

$$E_v = \frac{P}{vht} \quad (\text{Eq. 1.11})$$

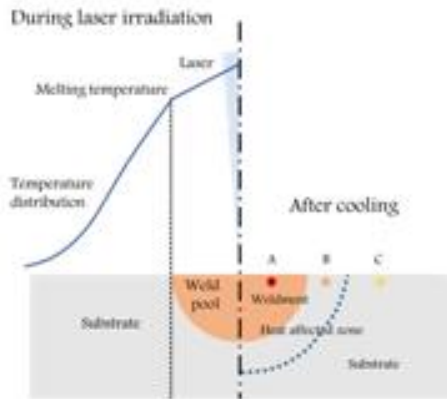
$$E_L = \frac{P}{v} \quad (\text{Eq. 1.12})$$

where P is the laser power, v is the scan rate, h is the powder layer thickness, and t is the Hatch distance.

Part building is regarded as the build-up of single-pass welds. Owing to the morphological features of a single-pass weld, lateral overlapping and vertical overlapping are necessary to achieve full

density part fabrication in multi-pass fusion welding. The Hatch distance is the off-set distance between neighboring laser scans, and it should be smaller than the weld metal width. The optimum Hatch distance is suggested to be 0.7 of the beam width [99]. The building strategy is another important factor affecting the building properties of parts. The building strategy consists of the tool-path for 2-dimensional pattern formation and vertical variation layer by layer.

(a)



(b)

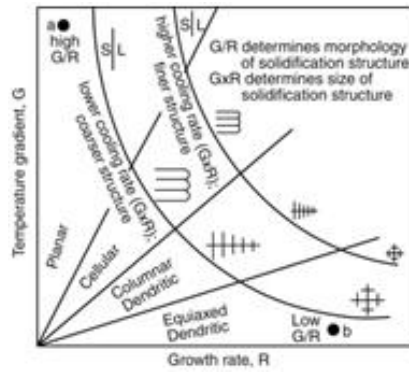


Figure 1.13. (a) Weld generation after single-pass laser scanning, (b) map of weld metal microstructures according to temperature gradient and solidification rate. Recomposed form [100] with permission through the Copyright Clearance Center.

1.6. Research Objectives

Since the first report of metallic glass in 1960, the potential of these materials in industrial application has been examined from various angles. To this end, the first order of research was to identify good glass forming alloys in conventional metallic systems, such as Fe, Ti, Mg, and Cu. Over many years, intensive work has been conducted to find general rules pertaining to alloy designs with high GFA. Indeed, the ability to cast rods with diameters exceeding 1 cm was achieved for various alloy systems, including Fe-based alloy system. Currently, there is a strong demand to address the limited ductility of glass forming alloys, which is essential for their application as structural materials.

The main focus of this research is to understand how to develop tailor-made metallic glasses by controlling alloy composition as well as process. In order to do so, tailoring atomic scale microstructure of metallic glasses together with an efficient processing method are needed for the enhanced mechanical properties of metallic glasses. From the preliminary researches, it was concluded that the BMG composites with nanometer to micrometer 2nd phases was prone to premature failure during compression tests or work-softening behavior after yielding because of their intrinsic (highly localized deformation: shear bands) and extrinsic (defect: poor interparticle bonding, interphase boundary and porosity) problem. Therefore, a

new concept of the heterogeneous microstructure (atomic scale heterogeneity by constituting elements and gradient relaxation behavior) and one-step processing method (casting or additive manufacturing) were adopted to overcome the aforementioned problem.

This work carefully presents tailor-made design guidelines for the application of glass forming alloys as a structural materials based on evaluating structure-property relationship. These guidelines concern two main objectives that must be met: (1) control of the atomic scale amorphous structure through composition control, identification of plasticity change and suggestion of potential deformation mechanisms, and (2) the overcoming of the scale limitations of glass forming alloys with reasonable plasticity through process control method, such as additive manufacturing. The primary goals of this research are three fold: (1) to design novel bulk metallic glass with enhanced plasticity by introducing a new concept of atomic scale heterogeneity through constituting elements and gradient relaxation behavior, (2) to understand the mechanical behaviors in terms of the correlation with microstructure and mechanical properties, and (3) to clarify the basic deformation mechanism that operate in metallic glasses with atomic scale heterogeneity.

Chapter 2. Experimental Procedures

2.1. Sample preparation

2.1.1. Arc melting

Alloy ingots with the desired compositions were prepared by the arc melting method with a constant arc voltage of 20 V and the arc current of 150 A [Figure 2.1(a)]. Pure elements (≥ 99.9 % purity) were placed on water-cooled copper hearth and were melted under a Ti-gettered argon atmosphere with a total pressure of 40 kPa (99.999 % purity) [Figure 2.1(b)]. The mixtures of elements were melted by arc plasma from a tungsten electrode and were re-melted at least 4 times after flipping to produce homogeneously alloyed buttons. The weight loss during the melting process was controlled to be less than 1% of the initial weight.

2.1.2. Melt spinning

The arc-melted ingots were crushed into small pieces and inserted in a quartz tube with a small nozzle (less than 1 mm in diameter). The tube was installed in a the melt-spinning apparatus, and then the chamber was evacuated and back-filled with argon gas at a pressure of 50 kPa. The pieces were inductively re-melted, and the molten alloys were quenched by injection of the melt onto a

rotating copper wheel with a linear velocity of 40 m/s. The resulting ribbons were 30 μm thick and 6 mm wide on average.

2.1.3. Injection/Suction casting

To obtain rod-shaped bulk samples, the alloy ingots were placed in a water-cooled copper mold and were melted by arc plasma and were injection/suction-cast into the mold with cylindrical cavities of various diameters ranging from 1 mm to 3 mm and heights ranging from 30 mm to 50 mm.

2.1.4. Atomization

To produce powder for AM, a high capacity gas atomizer (KITECH, Republic of Korea) using Ar gas was employed for the production of high purity metallic glasses composed of $\text{Zr}_{65}\text{Cu}_{17.5}\text{Al}_{7.5}\text{Ni}_{10}$, and the mother alloy was first prepared by using a vacuum induction melting furnace. The prepared mother alloy was heated up to about 1,400°C in an argon atmosphere using a vacuum induction melting furnace and a magnesia crucible to produce a liquid metal. The molten metal, an orifice of diameter 3 mm, was sprayed with Ar gas of pressure 65 bar to form a powder. The fabricated powder was automatically separated according to particle size. [Figure 2.2]

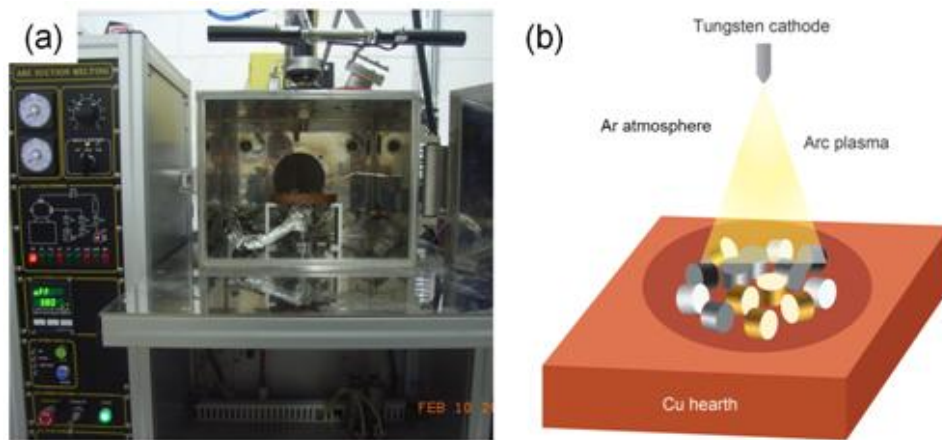


Figure 2.1. (a) Arc discharge machine installed in laboratory and (b) schematic diagram of arc melting process utilized for the preparation of master alloys with desired compositions.

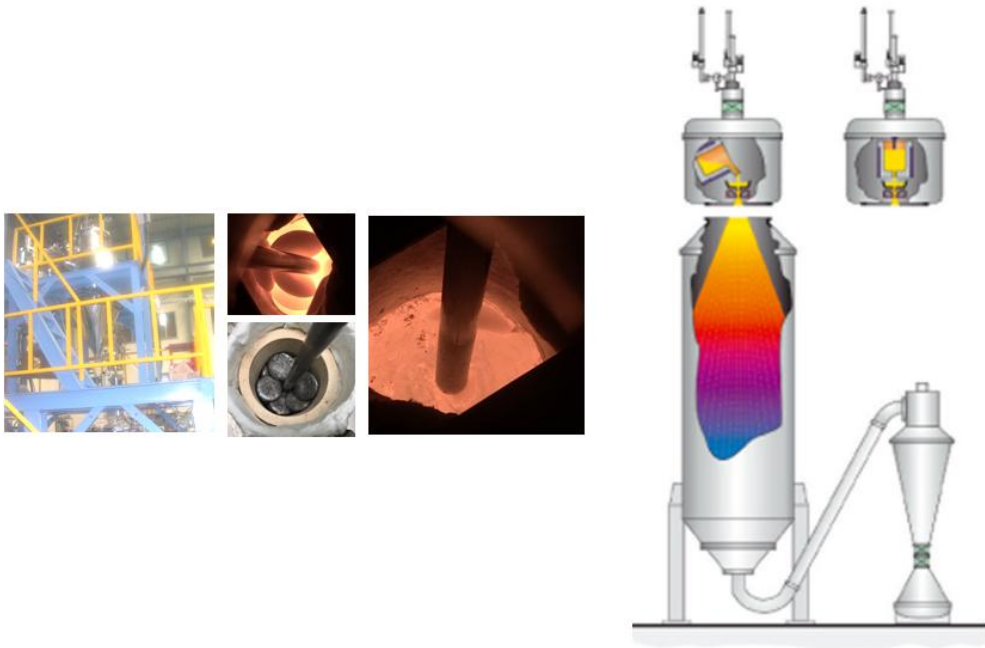


Figure 2.2. Overview of gas atomization instruments in KITECH.

2.1.5. SPS

Spark plasma sintering (SPS) is considered a high-speed powder consolidation process because the sintering step is finished within a few minutes. Metallic glass powders were filled in a graphite mold, and sintering of the powders was performed by SPS (KITECH, Republic of Korea). The vacuum condition applied during the sintering process was 5.0×10^{-3} torr with a pressure of 45MPa. To optimize the sintering temperature, the powders were heated to 700, 800, 900, 1000°C and they were maintained at these temperatures for 2, 4, 6, 8, and 10 min.

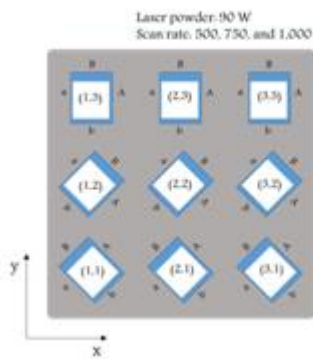
2.1.6. Laser powder bed fusion AM

For additive manufacturing, an Mlab cusing machine (ConcepLaser, Germany) was used. (Fig 2.3 (a)) A parts model is shown in Fig 2.3 (b) and (c). The laser PBF machine's laser power was 90 W, the scan speed were 500, 750, 1,000, and 1,600 mm/s. The layer thicknesses were 25 and 50 μm , and the hatch distance was 85 μm .

(a)



(b)



(c)

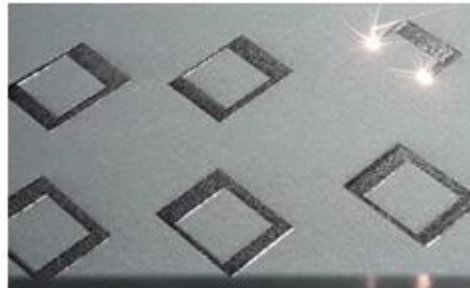


Figure 2.3. Mlab curing machine and 3D model

2.2. Microstructural characterization

2.2.1. X-ray diffraction

Initial characterization of the alloys was performed by X-ray diffraction (XRD), using a diffractometer (XRD, Bruker, New D8 Advance, Germany) with a Cu K α radiation source ($\lambda=1.5405 \text{ \AA}$). The diffractometer was calibrated using a silicon powder. XRD patterns collected from cross sections of bulk rod samples, ribbon samples, or powders, typically with $2\theta = 20^\circ \sim 90^\circ$, with a scanning rate of 4 degrees per minute. X-ray diffraction experiments are used routinely to identify the structural phases present in samples.

2.2.2. Scanning electron microscopy

Scanning electron microscopy (SEM, Hitachi, SU70, Japan) analysis was performed to characterize the morphology of the as-atomized powder. To observe the microstructure and morphology, the samples were fixed on an aluminum alloy or brass holder by electrically conductive adhesives, such as silver paste or carbon tape.

2.2.3. Transmission electron microscopy

In this work, the transmission electron microscopes (TEMs) used were JEOL 2100F and ARM1300S (in KBSI, Daejeon). Phase identification was done by selected area diffraction pattern (SADP) analysis and the chemical composition was also analyzed by energy

dispersive spectrum (EDS) analysis (Oxford INCA Energy 6498) linked with JEM 2100F. The operating voltages were 300 KeV in the JEOL 2100F and 1250 KeV in ARM1300S. Thin foils for TEM were prepared by electrolytic electro jet polishing of the center part of each specimen in a solution of 15 % perchloric acid and 85 % ethanol at 243 K. Ion milling was performed (Gatan, PIPS 691), by double-sided Ar⁺ ion-beam etching at 2.0~3.5 kV acceleration voltage.

2.2.4. Small angle X-ray scattering

The presence of nanoscale heterogeneities in samples was investigated by small angle X-ray scattering (SAXS) measurements in transmission mode at the 4C beamline of the Pohang Light Source II (PLS-II, 3.0 GeV, Pohang, Republic of Korea) [Figure 2.4]. The distance to a detector was set to be 5 m and an incident X-ray beam with the wavelength(λ) of 1.608 Å ($\Delta\lambda/\lambda = 1.5 \times 10^{-2}$) was applied. The obtained two-dimensional scattering data was averaged azimuthally to yield the plot of intensity against the scattering wave vector; $q = 4\pi\sin(\theta/2)/\lambda$, where θ is the scattering angle.

2.2.5. Extended X-ray absorption fine structure

For detailed analysis of the atomic structure of the samples, X-ray absorption fine structure (XAFS) measurements were performed at the 7D beamline of the PLS-II [Figure 2. 5]. The X-ray absorption spectra of the constituent elements were obtained in transmission

mode under ambient conditions. All element foils were also measured as a reference to calibrate for any inconsistency in the energy shifts during the data collection. To eliminate the higher-order harmonics, a Si (311) monochromator crystal was detuned to 70% in intensity for each element edge. The obtained data were processed using the IFEFFIT1.2.12 suite of Athena software [101]. The smooth pre-edge functions were removed by a linear extrapolation method to avoid instrumental background and absorption from other edges [102]. The resultant element-resolved absorption ($\mu(E)$) data was normalized afterwards using atomic-like absorption profiles followed by careful fits to the obtained data using the Artemis software contained in the IFEFFIT software package.



Figure 2.4. Overview of small angle X-ray Scattering instruments in the Pohang Accelerator Laboratory

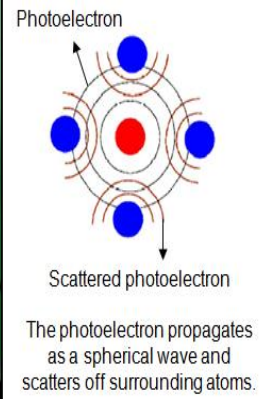


Figure 2.5. Overview of extended X-ray absorption fine structure instruments in the Pohang Accelerator Laboratory

2.3. Thermal and mechanical analysis

2.3.1. Differential scanning calorimeter

A differential scanning calorimetry (Perkin Elmer DSC 8500) which has a temperature scanning range from room temperature to approximately ~ 1023 K, was used to identify the phase transformations such as glass transition and crystallization. Each sample was enclosed in an aluminum or copper pan and was placed in a Pt holder. An empty pan was placed in the other Pt holder for a reference. The whole system was purged with high purity argon gas to minimize sample oxidation. As the temperature of the two pans was increased, the sample could undergo exothermic or endothermic reactions, which would cause a temperature difference to develop between the two holders. The heat released or absorbed during the phase transformation was recorded as a function of the average temperature. The heating rates for non-isothermal scans were 20 and 40 K/s. The temperature and enthalpy were calibrated using pure In and Zn standards. In isothermal mode, the temperatures of the sample and the reference were raised to the pre-setting temperature and maintained isothermally. Both non-isothermal and isothermal DSC can be used to study phase transformation kinetics.

2.3.2. Nano indentation tests

Nano-indentation tests (Hysitron TI 750 TriBlIndenter) were

performed on the fine-polished cross-section of the ribbon samples at the constant loading rate of 1 mN/s up to the maximum load 8 of mN using a conical-type indenter tip with a radius of 2 μm . For statistical analysis of the strain burst sizes, at least 400 pop-ins per sample were gathered from the load (F) versus displacement (h) curves of the nano-indentation test results.

2.3.3. In-situ bending test

For in-situ observation of shear banding events, bending tests were carried out on the ribbon samples using a self-designed experiment setup whose operation procedure is summarized as follows. At the beginning of the test, ribbon samples were fixed between two platens (one fixed and the other movable) and bent by moving the movable platens towards the fixed platens. As the formation of shear steps at ribbon surface affects the reflection of light, individual events were detectable by optical microscopy. Optical photographic images were taken at a rate of 25 frames per second [Figure 2.6].

2.3.4. Compression test

The mechanical properties of the as-cast samples were measured at room temperature under compressive mode at a strain rate $1 \times 10^{-4} \text{s}^{-1}$ (Housefield; H25K-T). Specimens were machined from injection-cast samples into cylinders 1 mm in diameter and 2.5 mm in

height. The loading surfaces were polished to be parallel with the accuracy of less than 10 μm , and the samples were fixed in a jig designed to ensure parallel ends.

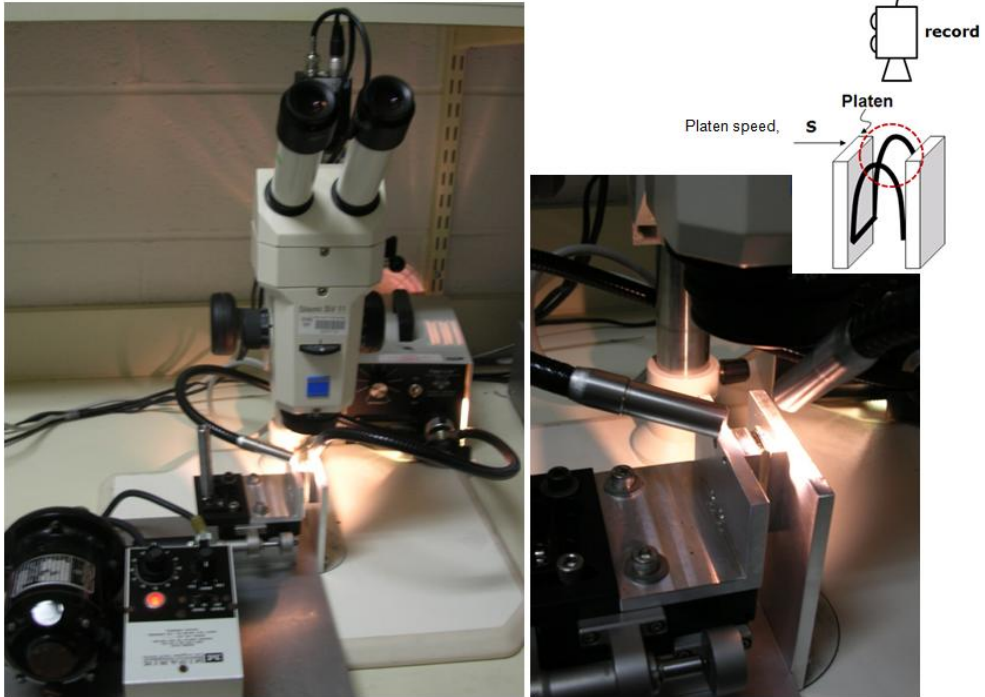


Figure 2.6. Self-designed experimental equipment for in-situ bending test.

Chapter 3.

Development of tailor made metallic glasses by controlling composition

3.1. Introduction

The enhancement of plasticity without losing strength has been recently reported in several monolithic BMGs (Table 3.1). Interestingly, all the alloy systems in presented Table 3.1 possess at least one atomic pair having positive heat of mixing (ΔH^{mix}). Based on the empirical rules for high glass forming ability (GFA) [103], a large negative relationship among constituent elements is required to obtain a high GFA. It can be understood that a negative relationship among the constituent elements can lead to a homogeneous and random mixture of atoms which is favorable for the formation of an amorphous structure. Thus, most studies on BMG alloy design have focused on finding suitable additional elements that have a negative relationship with the constituent elements in various alloy systems to enhance the GFA. However, Table 3.1 shows that the addition of elements having a positive relationship with constituent elements can be favorable for the simultaneous increase of plastic strain and the GFA. Furthermore, recent reports on phase separating MGs with large

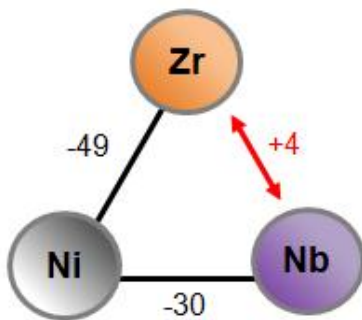
repulsive force between partial constituent elements suggest that an inhomogeneous microstructure composed of two different amorphous phases can contribute to the enhancement of plasticity[104, 105, 80].

In the present study, we systematically investigated the effect of alloying elements a having positive relationship with one of the constituent elements on the atomic structure and plasticity in simple ternary Ni-Nb-(Zr, Y, Gd) alloy systems. Ni₆₀Nb₄₀ was selected as a starting compositions because it exhibits a relatively high GFA even in simple binary systems[106], thereby enabling us to quantitatively study the relationship between the atomic structure and mechanical properties through extended X-ray absorption fine structure (EXAFS) analysis. Alloying elements having different magnitudes of positive relationship with Nb were chosen to compare their effects on microstructures. The values between the elements [107] investigated in this study (Ni, Nb, Zr, Y, and Gd) are summarized in Figure 3.1.

Composition	D_{max} (mm)	ϵ_p (%)	ΔH^{mix}
$Cu_{47}Ti_{33}Zr_{11}Ni_8Si_1$	4	3.5	Nb-Ti (+2 kJ/mol)
$Cu_{47}Ti_{33}Zr_7Nb_4Ni_8Si_1$	5	6.1	Nb-Zr (+4 kJ/mol)
$Cu_{50}Zr_{50}$	2	4.8	Cu-Ag (+2 kJ/mol)
$Cu_{50}Zr_{40}Ag_{10}$	3	6.6	
$Cu_{50}Zr_{43}Al_7$	3	6	Cu-Ag (+2 kJ/mol)
$Cu_{43}Zr_{43}Al_7Ag_7$	8	9	
$Cu_{46}Zr_{47}Al_7$	3	3.2	Zr-Gd (+9 kJ/mol)
$Cu_{46}Zr_{45}Al_7Gd_2$	10	4.3	
$Cu_{60}Zr_{30}Ti_{10}$	2	3.2	Cu-Ag (+2 kJ/mol)
$Cu_{55}Zr_{30}Ti_{10}Ag_5$	3	6.3	
$Mg_{65}Cu_{25}Gd_{10}$	8	1.8	Cu-Ag (+2 kJ/mol)
$Mg_{65}Cu_{20}Ag_5Gd_{10}$	11	2.3	
$Ni_{59}Zr_{20}Ti_{16}Si_2Sn_3$	3	4.1	Nb-Zr (+4 kJ/mol)
$Ni_{59}Zr_{16}Nb_7Ti_{13}Si_3Sn_2$	5	8.4	Nb-Ti (+2 kJ/mol)
$Zr_{70}Cu_{12.5}Ni_{10}Al_{7.5}$	-	8.1	Cu-Ag (+2 kJ/mol)
$Zr_{62}Cu_{12.5}Ni_{10}Al_{7.5}Ag_8$	-	14.5	
$Zr_{57}Ti_5Cu_{20}Ni_8Al_{10}$	-	3.8	Ta-Zr (+3 kJ/mol)
$Zr_{59}Ta_5Cu_{18}Ni_8Al_{10}$	-	9	

Table 3.1. Summaries of characteristic changes in various alloy systems with additional element having positive heat of mixing with one or more constituent elements ; maximum diameter for glass formation(D_{max}) fracture strain in compressive mode(ϵ_p) and heat of mixing among constituent elements

(a) Small positive ΔH^{mix}



(b) Large positive ΔH^{mix}

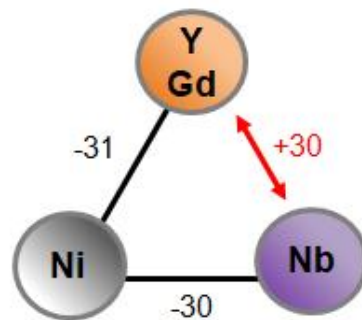


Figure 3.1. Additional alloying elements having positive heat of mixing between constituent elements ; (a) small positive (Zr), and (b) large positive (Y, Gd).

3.2. Effect of Small Positive Heat of Mixing Between Constituent Elements

3.2.1. Microstructural characterization in Ni-Nb-Zr

To elucidate how the addition of an element having a small positive relationship affects the microstructure we substituted Nb in $\text{Ni}_{60}\text{Nb}_{40}$ with Zr which $\Delta H_{\text{Nb-Zr}}^{\text{mix}}$ has of 4 kJ/mol [107] up to 20 at.%. In this study, the microstructures of $\text{Ni}_{60}\text{Nb}_{40-x}\text{Zr}_x$ ($0 \leq x \leq 20$ at.%) were investigated by multi-scale testing methods, including TEM observation and SAXS measurement for nanoscale characterization and XAFS measurement of the atomic structure.

Figure 3.2 (a) and (b) show high resolution TEM (HRTEM) images obtained from ribbon samples of Zr0 and Zr10, respectively. Both of them show typical amorphous structures without any lattice fringes, and no difference in topological inhomogeneity is noticeable. The fast Fourier transformed (FFT) diffraction patterns inserted as insets in each image also confirm a lack of crystallinity. To investigate whether there are chemical heterogeneities within a volume larger than that which can be investigated via electron microscopy, SAXS measurements were carried out for Zr10 and Zr20 ribbons. Figure 3.3 shows the SAXS patterns of these alloys. Both patterns exhibit power-law regions at the low q -range and following plateaus at $q \geq \sim 2 \times 10^{-2} \text{ \AA}^{-1}$, which are the typical patterns of monolithic MGs

without any chemical heterogeneity whose width is over 1nm, which is the minimum detectable size in SAXS.

To characterize the changes in the atomic structure of $\text{Ni}_{60}\text{Nb}_{40-x}\text{Zr}_x$ upon Zr addition, we also conducted EXAFS analysis of Zr0, Zr10, and Zr20, which is a particularly powerful experimental technique for atomic scale chemical analysis. The resultant datasets were fitted to yield the coordination number around one atom and the interatomic distance. More specifically, the normalized EXAFS functions, $k^3\chi(k)$, were extracted first from the absorption cross-sections, where $\chi(k)$ is the EXAFS equation consisting of various parameters as follows [108],

$$\chi(k) = \sum_j \frac{N_j S_0^2(k) f_j(k) e^{-2k^2\sigma_j^2} e^{-2r_j/\lambda(k)}}{kR_j^2} \sin[2kR_j + \delta_j(k)] \quad (\text{Eq 3.1})$$

Here, $f(k)$ is the back scattering amplitude, and $\delta(k)$ is the phase shift due to the atomic potential, N is the number of neighboring atoms, R is the distance to the neighboring atoms, and σ^2 is the Debye-Waller factor accounting for thermal and static disorder. Also, λ is the inelastic electron mean free path, and S_0^2 is the amplitude reduction factor representing the shake-up and shake-off effect of a central atom. Then, the normalized EXAFS functions were transformed to r-space functions by Fourier transform (FT). The FT of $k^3\chi(k)$ was

obtained using k-windows ranging from approximately 1 to 12 for the Ni K-edge and from approximately 3 to 12 for the Nb K-edge, respectively.

Figure 3. 4 shows the obtained $\text{FT}[k^3\chi(k)]$, in a restricted r approximately 0 to 4 Å, which was set to include only the main peak, thereby allowing separation of the contributions of the first coordination shell around an absorbing atom to EXAFS. The peak intensity of $\text{FT}[k^3\chi(k)]$ is basically related to the coordination number of each atomic pair, however, it is also affected by differences in the interatomic distances between constituting atomic pairs, as each pair yields a broad spectrum in r -space which overlaps the spectra of other pairs. Therefore, only a rough analysis of atomic structure is possible through a qualitative examination of $\text{FT}[k^3\chi(k)]$. Figure 3.4 (a) shows a decrease in the intensity of the main peak for the Ni K-edge with Zr addition, while a slight hump (denoted by an arrow on the right) becomes more obvious. Considering the Goldschmidt's radii of each element (2.48 Å of Ni, 2.92 Å of Nb, and 3.20 Å of Zr), the differences in spectra is probably due to the decrease in the number of Ni-Nb pairs and the simultaneous increase in the number of relatively large Ni-Zr pair, which would result in larger differences in interatomic distances, reducing the peak intensity. On the other hand, the intensity of the main peak for the Nb K-edge increases upon Zr addition, which implies the possibility of a different propensity in the variation of structural parameters.

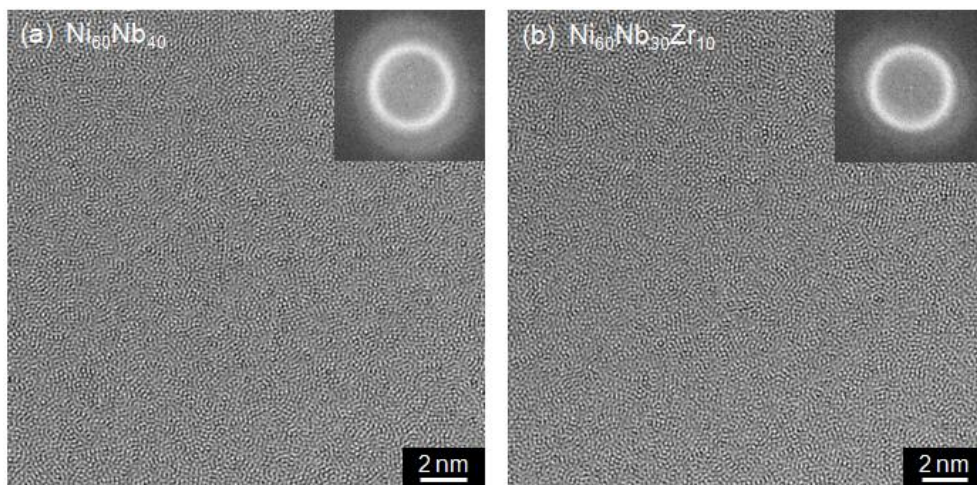


Figure 3.2. High resolution TEM images and SADPs obtained from melt spun (a) $\text{Ni}_{60}\text{Nb}_{40}$ and, (b) $\text{Ni}_{60}\text{Nb}_{30}\text{Zr}_{10}$ ribbons.

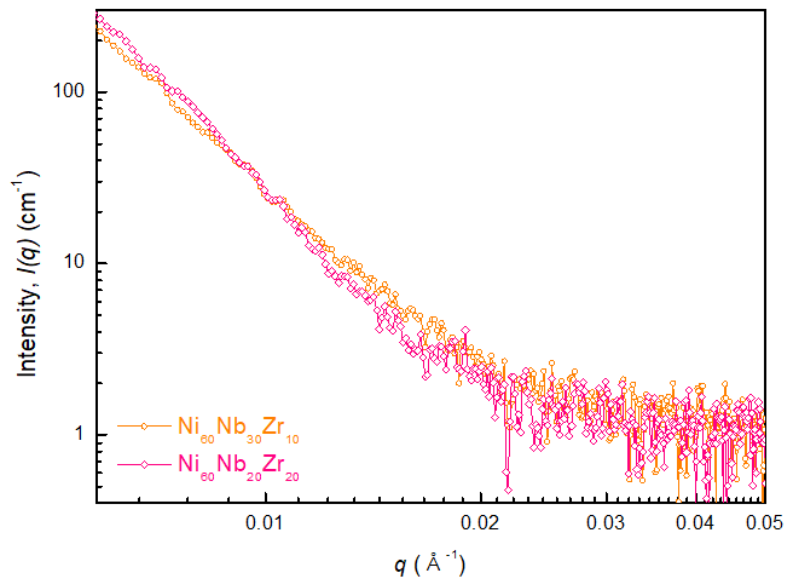


Figure 3.3. SAXS patterns obtained from melt spun (a) $\text{Ni}_{60}\text{Nb}_{30}\text{Zr}_{10}$ and, (b) $\text{Ni}_{60}\text{Nb}_{20}\text{Zr}_{20}$ ribbons.

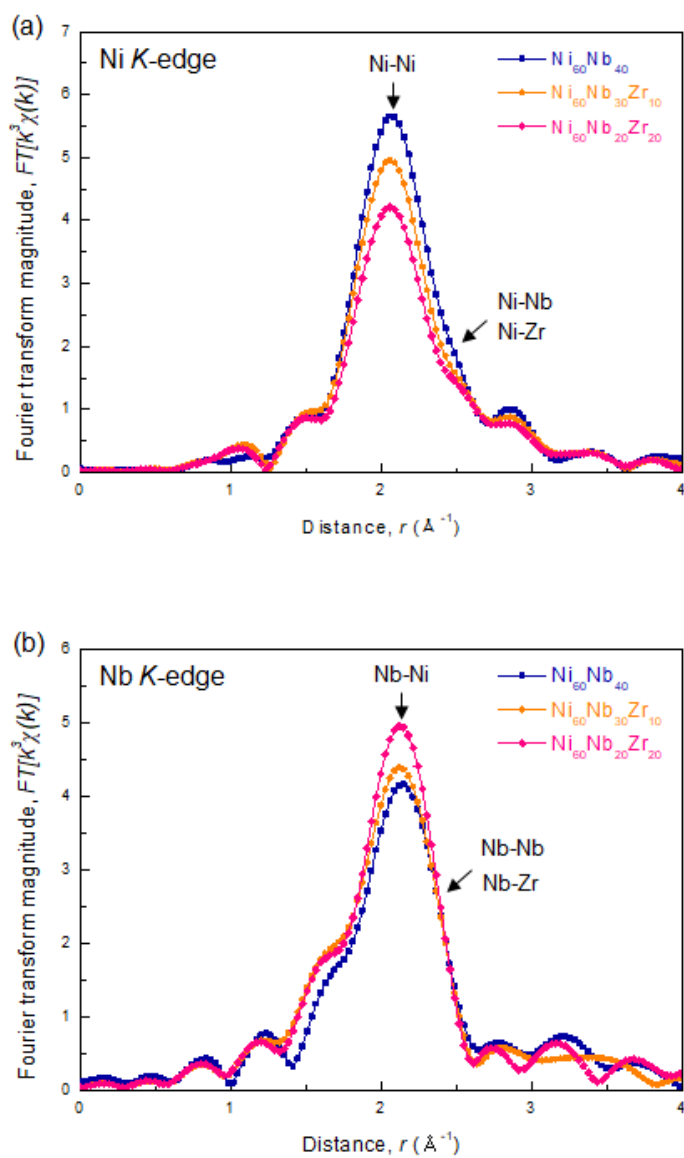


Figure 3.4. Fourier transform magnitude around (a) Ni for $\text{Ni}_{60}\text{Nb}_{40-x}\text{Zr}_x$ and, (b) Nb for $\text{Ni}_{60}\text{Nb}_{40-x}\text{Zr}_x$ alloy (x=0, 10, 20 at%).

For a holistic understanding of variation in atomic structure with the consideration of phase shift ($\delta(k)$), the simultaneous fitting of peaks at both Ni and Nb edges was carried out. The fitting results are presented in Figure 3.5 (a) and (b) for Ni K-edge and Nb K-edge, respectively, showing experimental and calculated data. The calculated coordination numbers and interatomic distances of the alloys investigated in this study are summarized in Figure 3.6. As seen in Figure 3.6 (a), the coordination number of the Ni-Nb pairs continues to decrease throughout the addition of Zr up to 20 at.%, while that of the Ni-Zr pairs increases. On the contrary, the coordination numbers of the Nb-Nb pairs and Nb-Zr pairs change only up to 10 at.% of Zr, remaining steady between Zr10 and Zr20 (Figure 6 (b)). When it comes to the other pairs in each edge, the coordination number of the Nb-Ni pairs continues to increase, although the change is relatively small in comparison to the variation in those of the other pairs. That of the Ni-Ni pairs remains nearly constant without a consistent trend. The results imply that the distribution of elements around Nb does not fully follow the variation in overall composition throughout the course of change in composition. Instead, Nb tends to maintain Nb-Nb pairs or replace Nb-Nb pairs with Nb-Ni pairs rather than Nb-Zr pairs.

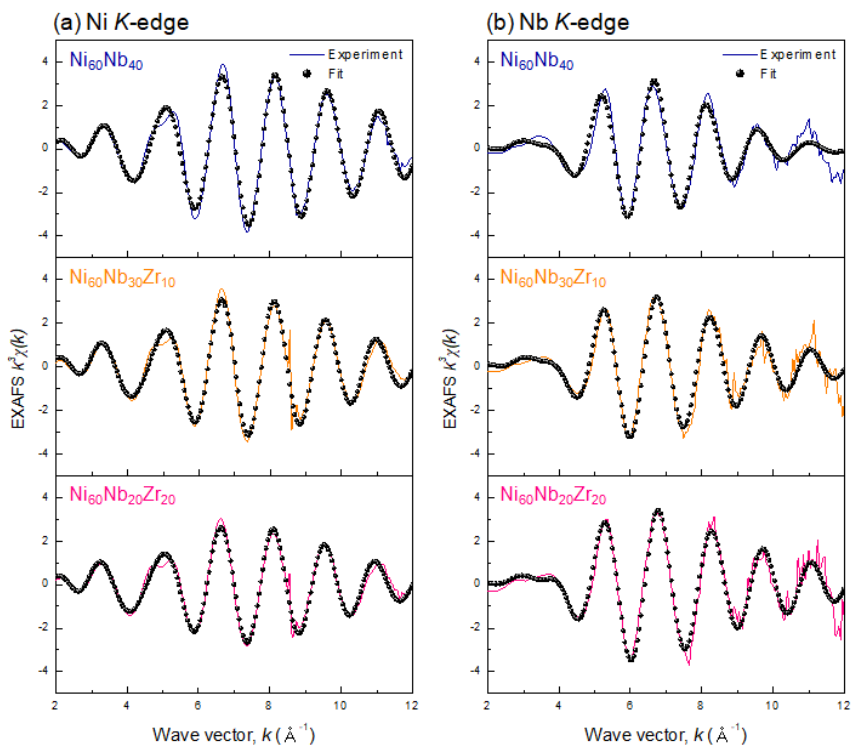


Figure 3.5. EXAFS spectra $k^3\chi(k)$ versus k curves of (a) Ni K-edge for $\text{Ni}_{60}\text{Nb}_{40-x}\text{Zr}_x$ and (b) Nb k-edge for $\text{Ni}_{60}\text{Nb}_{40-x}\text{Zr}_x$ alloy ($x=0, 10, 20$ at%).

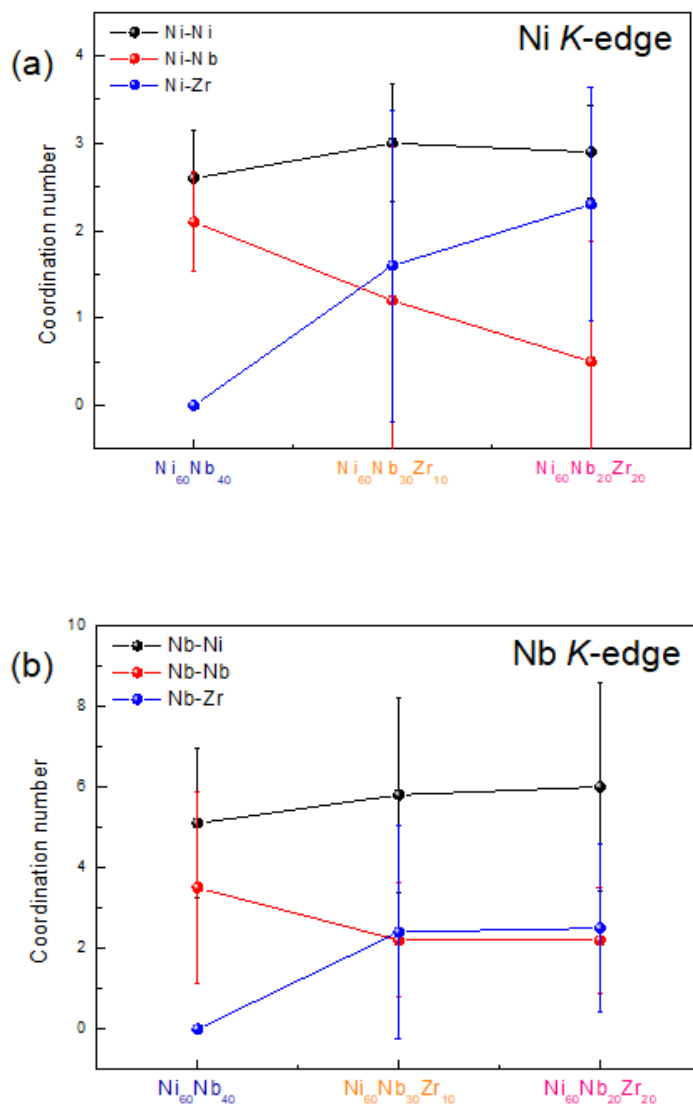


Figure 3.6. Coordination numbers around element of (a) Ni K-edge for $\text{Ni}_{60}\text{Nb}_{40-x}\text{Zr}_x$ (b) Nb k-edge for $\text{Ni}_{60}\text{Nb}_{40-x}\text{Zr}_x$ alloy ($x=0, 10, 20$ at%)

Additionally, change in the degree of local chemical order was investigated by two different methods, both of which give short range order (SRO) parameters. First, the Warren SRO parameter is estimated as

$$\alpha = 1 - Z_{AB}/Z_{AB}^* \quad (\text{eq 3.2})$$

with, $Z_{AB}^* = x_B \langle Z \rangle$ where $\langle Z \rangle$ is the total coordination number defined as $\langle Z \rangle = x_A Z_A + x_B Z_B = x_A (Z_{AA} + Z_{AB}) + x_B (Z_{BB} + Z_{BA})$ [109]. Here, Z_{ij} (i, j = A or B) represents the coordination number of *i-j* atomic pair. When A atom favors A-B pair over A-A pair, Z_{AB} is greater than Z_{AB}^* , yielding a negative value of α [109]. Secondly, the Cargill-Spaepen SRO parameter (η), which was proposed to better distinguish chemical effects from size effects, is calculated by

$$\eta = Z_{AB}/Z_{AB}^{**} - 1 \quad (\text{eq 3.3})$$

with $Z_{AB}^{**} = x_B Z_B Z_A / \langle Z \rangle$ [110]. Here, the preference for hetero-coordination results in a positive value of η [110]. The calculated SRO parameters for Nb-Ni pairs are listed in Table 3.2. Noted that a $\langle Z \rangle$ value of 5 to 7 is smaller than the ideal value of approximately 12 because EXAFS tends to underestimate when disorder is present [111].

Composition	Z_{AA}	Z_{AB}	Z_{BA}	Z_{BB}	$\langle Z \rangle$	Z_{AB}^*	α	Z_{AB}^{**}	η
Ni ₆₀ Nb ₄₀	3.5	5.1	2.1	2.6	7.04	2.816	-0.811	2.297	1.221
Ni ₆₀ Nb ₃₀ Zr ₁₀	2.2	5.8	1.2	3.0	6.06	1.818	-2.19	1.663	2.487
Ni ₆₀ Nb ₂₀ Zr ₂₀	2.2	6.0	0.5	2.9	5.60	1.120	-4.36	0.996	5.026

Table 3.2 Calculated chemical short range order parameter for Ni₆₀Nb_{40-x}Zr_x alloy(x=0, 10, 20 at%)

Since both the negative value of α and the positive value of η represent an inclination to form atomic pairs consisting of dissimilar elements [109, 110], the increase in absolute values of α and η for Nb-Ni pairs upon Zr addition indicates that Nb tends to coordinate with Ni beyond the compositional probability. With the consideration of ΔH^{mix} , it can be inferred from the results that positive ΔH^{mix} between Nb and Zr, which is thermodynamically unfavorable, prevents additional formation of Nb-Zr pairs while inducing preferential bonding between Nb-Ni or Nb-Nb pairs, thereby resulting in atomic scale chemical heterogeneities.

As Nb and Zr have different numbers of electrons in their d-shells, the substitution of Nb by Zr can also affect the electronic structure around the constituting elements; thus, the covalency of the bond is closely correlated with intrinsic brittleness [112, 113]. To explore the variation in electronic structure, the X-ray absorption near edge structure (XANES) spectra for the Ni K-edge and the Nb K-edge are compared as shown in Figure 3.7 (a) and (b), respectively. The insets are enlarged parts of the spectra showing absorption edges that reflect the electronic structure. The XANES spectrum for the Ni K-edge of Zr0 exhibits a shoulder, whereas that of Zr40 shows a hump, which indicates the hybridization of orbitals [114], in other words, the strengthening of the covalent characteristic of a bond [115, 116], whereas those of Ni₆₀Nb_{40-x}Zr_x (0 < x < 40 at.%) lie somewhere in between. In contrast, there was no noticeable change in the XANES

spectra for the Nb K-edge in any of the investigated alloys as shown in Figure 3.7 (b).

To clarify whether the change in the electronic structure obtained from the Ni K-edge is continuous, a linear combination fitting method was used to determine the weight factors of Zr0 and Zr40 in the derivative of normalized absorption ($d\mu(E)/dE$). Figure 3.7 (c) displays the representative fitting result with the experimental data of Zr20. The energy range for fitting was set to be range from 5 eV to 15 eV with the energy threshold (E_0) as a fiducial energy. Figure 3.7 (d) shows the weight factors of Zr40 for each alloy, which correspond well with a linear dotted line showing the weight factors of an ideal phase mixture estimated by a rule of mixture. The regression of data in Figure 3.7 (d) obtained by the least squares fitting method demonstrates that the regression coefficient (R^2) is 0.99, confirming the continuous change of the electronic structure. As the covalent characteristic of a bond contributes to intrinsic brittleness [112, 113], it can be inferred from the continuous change of the XANES spectra that the addition of Zr is disadvantageous to the improvement of plasticity in terms of the electronic structure.

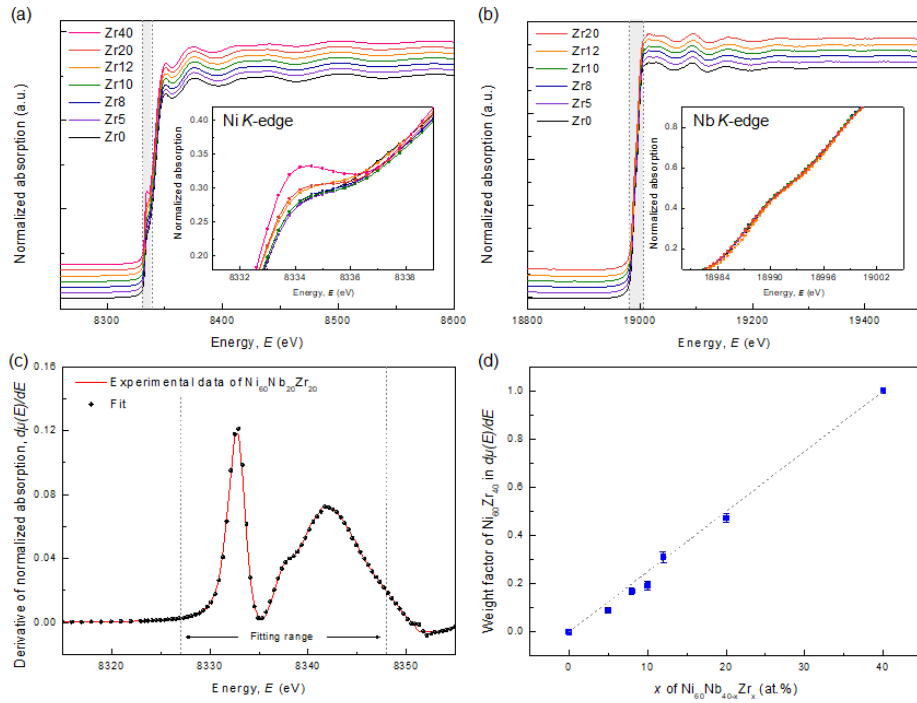


Figure 3.7. XANES spectra for (a) Ni K-edge and (b) Nb K-edge and (c) fitting data of Zr20, (d) weight factor for each alloy.

3.2.2. Deformation behavior in Ni-Nb-Zr

The microstructural analysis clearly shows that atomic scale chemical heterogeneities undetectable at nanoscale are introduced upon the addition of an element having small positive ΔH^{mix} . To investigate the effect of the heterogeneities in the deformation behavior of alloys, nanoindentation tests, and bending tests were carried out on melt-spun ribbon samples of Zr0, Zr10, and Zr20. In nano-indentation testing, strain bursts can occur as a result of either the activation of STZs in local areas where the applied stress approaches intrinsic strength or by heterogeneous shear band formation when the lowest stress along a viable plane exceeds the flow stress. The former would be manifested as a relatively small pop-in, whereas the latter would result in a relatively large pop-in. Hence, the size distribution of strain bursts reflects the dynamic behavior related to the formation and percolation of deformation units. For statistical analysis of strain burst sizes, at least 400 pop-ins per alloy were gathered from the load (F) versus displacement (h) curves of the nano-indentation test results, adopting the collection process described in [117, 118]. The displacement burst size (Δh) associated with a pop-in event was normalized by displacement (h), yielding the strain burst size ($S = \Delta h/h$), to eliminate statistical errors [117, 118]. Figure 3. 8 (a) shows the cumulative probability distributions of strain burst sizes ($P(>S)$) for each sample, which are well fitted by the following empirical relation:

$$P(> S) = AS^{-\beta} \exp - (S/S_c)^2 \quad (\text{eq 3.4})$$

where A is the normalization constant, β is the power-law exponent, and S_c is the cut-off strain burst size at which an exponentially decaying behavior begins out of the power-law relation due to a predominance of chaotic deformation events [117-119]. The fitting curves and resultant parameters are shown as solid lines in Figure 3. 8 (a) and values in Figure 3. 8 (b), respectively.

Interestingly, Zr20 shows a drastically increased β value for size-scaling behavior compared to Zr0 and Zr10 and a sharper drop of $P(>S)$ with increasing S , which indicates that the relatively large population of small strain bursts resulted from the local STZ activation in a self-organized critical state. It is probably due to the atomic scale chemical heterogeneities induced by the addition of Zr beyond a critical limit, since Zr-rich regions are softer than Nb-rich regions; therefore, they function as soft spots where shear deformation tends to occur, and the surrounding Nb-rich region with a relative rigidity would hinder the development of larger strain bursts. Furthermore, Zr20 exhibits a lower value than those of Zr0 and Zr10, implying the easier nucleation of chaotic shear bands [119]. This may be due to the lower energy barrier for shear band nucleation as can be inferred from the reduction of hardness from 12.1 ± 0.4 in Zr0 to 10.4 ± 0.6 in Zr20. Along with the high concentration of

loosely-packed regions accumulated by local STZ events at chemically-induced soft spots, it is expected to result in the formation of multiple shear bands.

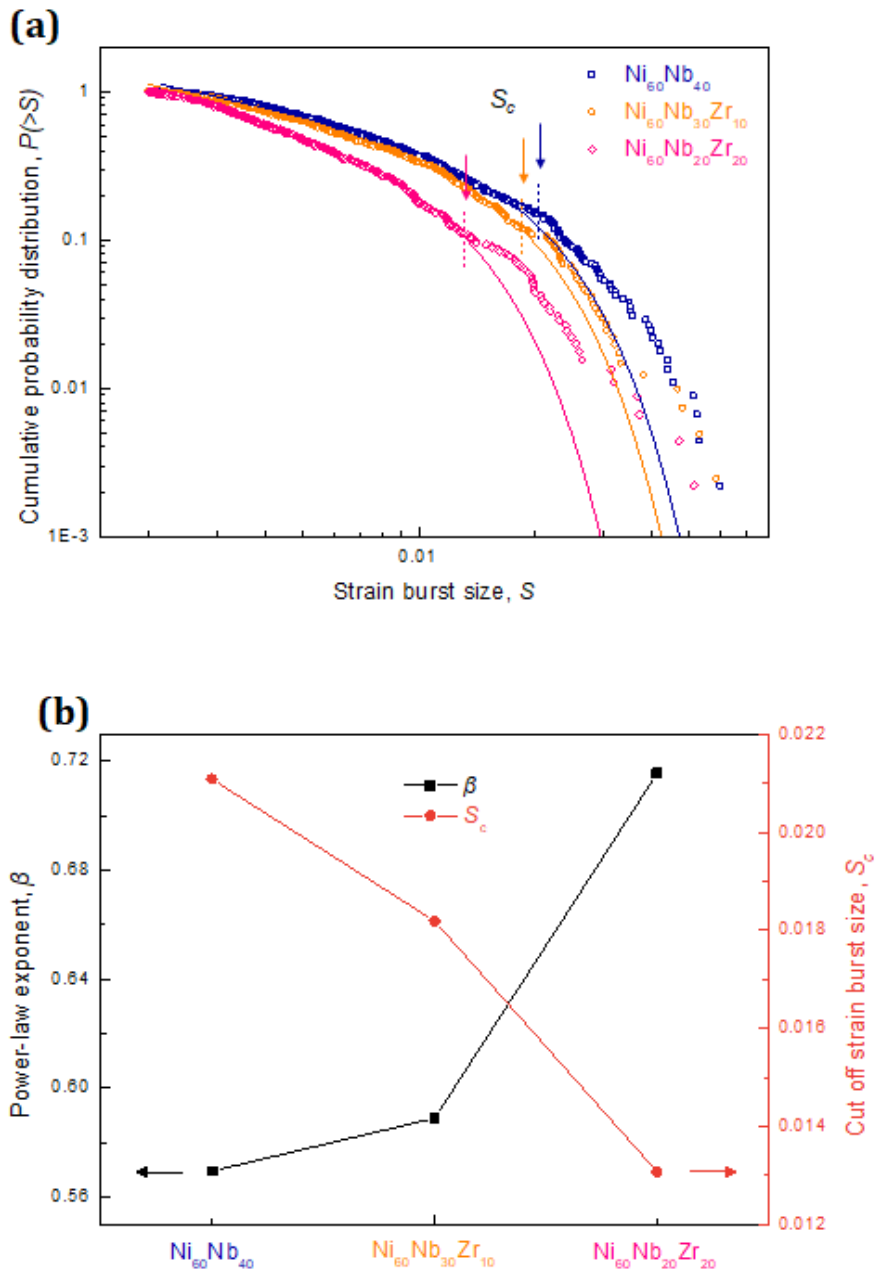


Figure 3.8. (a) Cumulative probability distribution of strain burst sizes and, (b) β and S_c values for each alloy.

Then, the evolution of multiple shear bands in Zr₂₀ was confirmed by in situ observation of shear steps during bending tests. Figure 3.9 shows the remarkable difference between the shear bending behaviors of Zr₀ and Zr₂₀. As seen the inset image of Figure 3.9 (c), melt-spun ribbon samples were fixed between two platens (one fixed and the other movable) and bent by moving the movable platen towards the fixed platen. Because the formation of shear steps in the ribbon surface affects the reflection of light, individual events were detectable by optical microscopy (OM). Figure 3.9 (a) and (b) shows shear steps formed on the surfaces of Zr₀ and Zr₂₀, respectively. Many small shear steps overlapped on the Zr₂₀ surface, thereby obscuring the differentiation between individual shear step (Figure 3.9 (b)). However, only a limited number of shear steps were produced on the Zr₀ surface (Figure 3.9 (a)). Figure 3.9 (c) shows the number of shear banding events that occurred between two points denoted by hollow circles in Figure 3.9 (a) and (b). As seen in the images, Zr₂₀ exhibited a rapid increase in the number of shear banding events reaching approximately 9.2 events/s compared to Zr₀ with approximately 2.5 events/s. The results clearly reveal the formation of multiple shear bands in Zr₂₀ whose microstructure possesses atomic scale chemical heterogeneities, despite the enhanced covalency of a bond which is expected to strengthen brittleness [112, 113].

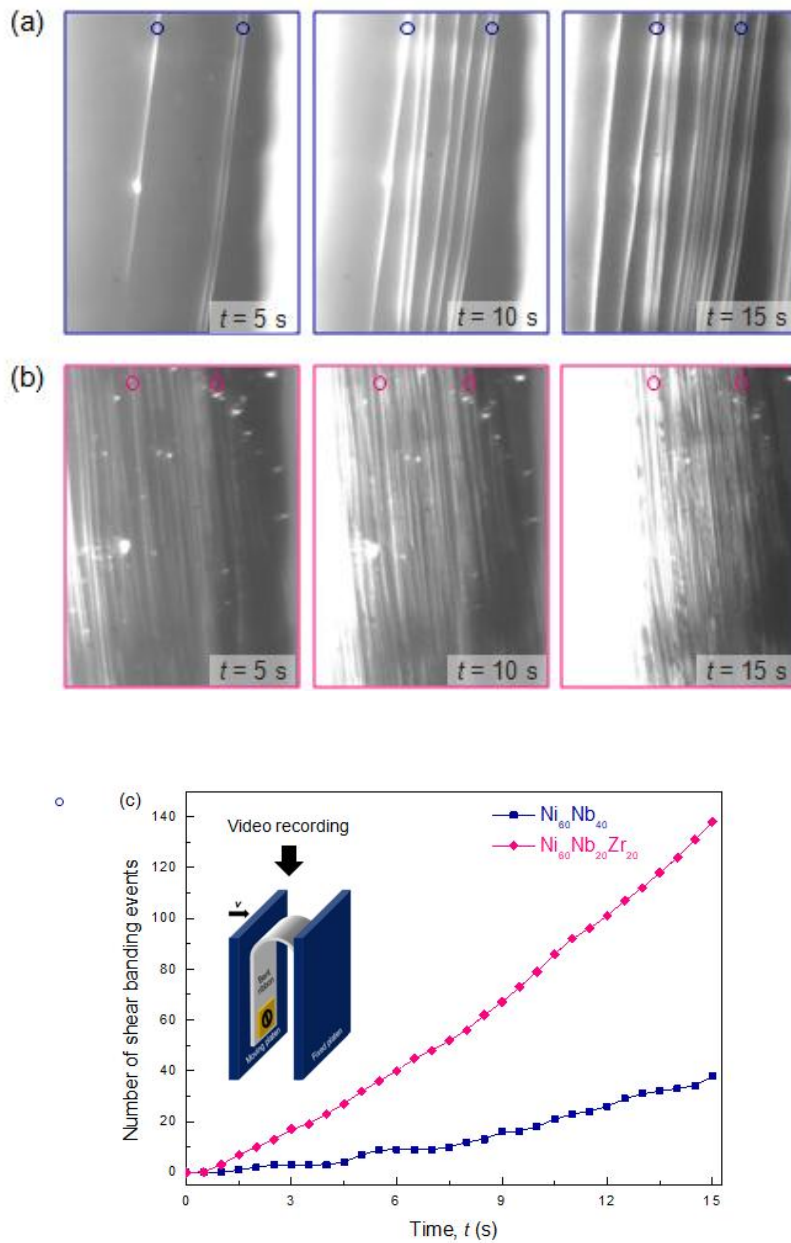


Figure 3.9. Shear steps formed on the surfaces of (a) Zr0 and, (b) Zr20 and, (c) the number of shear bend events for (a) and (b).

3.2.3. Enhancement of plasticity by processing control

Mechanical tests conducted on melt-spun ribbon samples showed that atomic scale chemical heterogeneities are beneficial for the generation of multiple shear bands. Because preferential ordering requires time for atomic arrangement, it can be inferred that the degree of atomic scale heterogeneities would differ in the relations to the cooling rate. To demonstrate the effect of the cooling rate on atomic scale chemical heterogeneities and the resultant plasticity, compression tests were performed on $\text{Ni}_{60}\text{Nb}_{40-x}\text{Zr}_x$ ($x=0, 5, 8, 10, 12, 20$ at.%). Figure 3.10 shows the compressive stress-strain curves for injection-cast samples with a diameters of 1 mm. The elastic strain (ϵ_e) and fracture strength (σ_f) of the Zr0 samples were 2% and 2,958 MPa, respectively, and the plastic strain to failure (ϵ_p) was almost zero. Similarly, Zr5 also failed showing no evidence of macroscopic yielding or plasticity. However, yielding and plastic deformation accompanied by serrated flows were observed for Zr8 and Zr10, with values of 2.4% and 2.7%, respectively. The values of these alloys were also greater than that of Zr0. The mechanical properties began to show deterioration again upon further substitution of Nb by Zr; for Zr15 and Zr20, the ϵ_p values were 0.2% and 0.5%, respectively and the σ_f values were reduced below that of Zr0.

It should also be noted that unlike the Zr20 ribbon sample that generated multiple shear bands during the bending test (Figure

3.9 (b)), the Zr20 rod sample exhibited only a limited number of serrated flows, whereas the Zr10 rod sample showed improved plasticity with many serrated flows. These results highlight that the optimum composition for heterogeneity-induced plasticity changes in relation to the cooling rate, which influences the length scale of chemical heterogeneities. One advantage of monolithic BMGs with improved plasticity due to the presence of atomic scale chemical heterogeneities in the present study is that the yield strength of the MG remains almost the same despite the enhancement of plasticity, as seen in the cases of Zr8 and Zr10 (Figure 3.10).

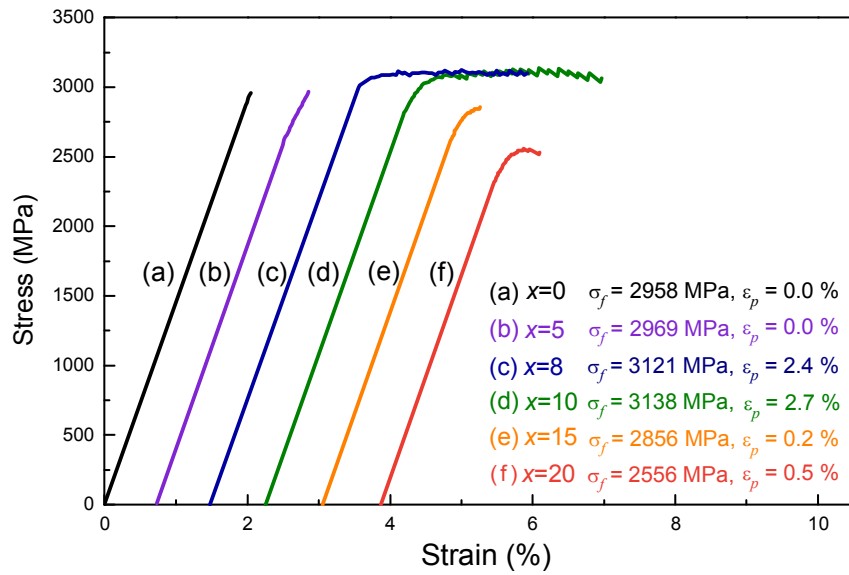


Figure 3.10. Compressive stress-strain curves for injection-cast samples with diameter of 1 mm.

3.2.4. Discussion

In general, the enhancement of plasticity in metallic glass matrix composites reinforced with microscale ductile second phases [120-122] is accompanied by decreased strength due to lower yield strengths of the crystalline phases embedded in the amorphous matrix. However, the results of this study show that simultaneous increase of strength and plasticity is possible with the introducing of atomic scale chemical heterogeneities in monolithic MGs. This is particularly important considering the reports on the improvement of GFA upon minor addition of elements having a small positive relationship with other constituent element because strength, plasticity, and GFA are properties of crucial significance in MGs for structural applications.

3.3. Effect of Large Positive Heat of Mixing Relationship Between Constituent Element

Although it has been reported that the addition of elements having positive ΔH^{mix} with constituent elements can improve GFA by stabilizing the liquid phase through the atomic scale heterogeneity caused by chemical short- and medium-range order [104, 123-127], it is generally expected that increase of additional element having larger positive ΔH^{mix} with constituent elements leads to the deterioration of GFA, causing the formation of crystalline phase or inducing phase separation. To obtain further insight in this regard, we substituted Nb in Ni₆₀Nb₄₀ with rare earth metals (Y,Gd) having a relatively large ΔH^{mix} of 30 kJ/mol [107] with Nb up to 20 at.%. In this study, the microstructural features of these alloys were characterized by thermal analysis and electron microscopy.

3.3.1. Microstructural characterization in Ni-Nb-(Y, Gd)

Figure 3.11 (a) shows the DSC thermograms of melt-spun ribbon samples of Y0, Y10, and Y20 during heating with a heating rate of 0.667 K/s. The DSC traces can be clearly classified into two groups based on the temperature range of the exothermic reactions, i.e., low-temperature exothermic reactions with crystallization onset temperatures(T_x) in the range from 580 to 600 K for Y10 and Y20

and high-temperature exothermic reactions with T_x in the range from 820 to 930 K for the entire alloys. The DSC trace of Ni₆₀Nb₄₀ that exhibits only a high-temperature exothermic reaction without a noticeable low-temperature reaction indicates that the first and second exothermic reactions correspond to the crystallization of Y-rich and Nb-rich amorphous phases, respectively.

Figure 3.11 (b) shows the DSC thermograms of Gd₀, Gd₁₀, and Gd₂₀ measured under the same experimental condition described above. Only high-temperature exothermic reactions were clearly detectable, confirming the presence of Nb-rich amorphous phases. Considering the melting temperature of Gd, which is lower than those of Y and Nb, exothermic reactions at a lower temperature range are expected for potential Gd-rich amorphous phases; however, another crystallization behavior was hardly distinguishable from the obtained DSC traces.

Figure 3.12 (a) shows a TEM bright field (BF) image obtained of a Y₂₀ ribbon sample. The microstructure mainly exhibits interconnected structures with dark particle-like regions and bright matrix-like regions as well as smaller bright particles in the former regions and dark particles in the latter regions. The average width of the interconnected structures is 160 nm and the diameters of particles range from a few nanometers to 50 nm. The particle-like shape of the interconnected structures is probably due to the strong collision of melts onto the copper wheel during melt spinning. The

smaller particles embedded in the interconnected structures imply that the melt separated into two liquids of different compositions first via spinodal decomposition, followed by separation of the second phase at a lower temperature through the nucleation and growth mechanism. Furthermore, the compositions of the dark region indicated by ① and the bright region indicated by ② measured by EDS were $\text{Ni}_{63.7}\text{Nb}_{31.2}\text{Y}_{5.1}$ (Ni-Nb rich) and $\text{Ni}_{69.0}\text{Nb}_{6.1}\text{Y}_{24.9}$ (Ni-Y rich), respectively. From the BF image and composition analysis, it can be concluded that the large positive ΔH^{mix} between Nb and Y resulted in liquid phase separation into Ni-Nb rich and Ni-Y rich amorphous phases.

The SADP in Figure 3.12 (b) was obtained from the area including the region covering dark regions and bright regions. In contrast to the separate crystallization behaviors observed in the DSC measurements (Figure 3.11 (a)), halo rings of different phases are hardly distinguishable in Figure 3.12 (b), which may be attributed to a small difference between the atomic radii of Nb and Y, which would result in the close positioning of halo rings from different phases. The dark field (DF) image shown in Figure 3.12 (d), which was obtained by selective positioning of an objective aperture on the outer halo ring, as indicated in Figure 3.12 (c), reveals the distribution of the Ni-Nb rich amorphous phase more clearly.

On the other hand, the TEM BF image of the Gd20 ribbon contains dark particles embedded in the bright matrix, as shown in

Figure 3.12 (e). Part of matrix is black due to the alignment on the zone axis. The size of the dark gray particles ranged widely from 10 nm to 600 nm. The compositions of the dark particles ③ and the bright matrix ④ measured by EDS were $\text{Ni}_{57.4}\text{Nb}_{36.6}\text{Gd}_6$ (Ni-Nb rich) and $\text{Ni}_{55.8}\text{Nb}_{5.6}\text{Gd}_{38.6}$ (Ni-Gd rich), respectively, confirming phase separation as in $\text{Ni}_{60}\text{Nb}_{20}\text{Y}_{20}$ ribbon. The SADP in Figure 3. 12(f) was obtained from the area including the region covering the dark particles and the bright matrix. Although crystallization peaks were hardly observable in the DSC measurements (Figure 3 11(b)), two halo rings that suggest the presence of two different amorphous phases are clearly observed in Figure 3. 12(f). The DF image in Figure 3. 12(h) with an objective aperture on the outer halo ring, as indicated in Figure 3. 12(g), also reveals the distribution of Ni-Nb rich amorphous phase particles.

The TEM images and SADP of both Y20 and Gd20 ribbon samples show that crystalline phases are present in the bright regions due to the lower GFA of the Ni-(Y, Gd) rich phases in comparison to that of the Ni-Nb rich phases. Therefore, the result indicates that the larger value of a positive relationship in atomic pairs such as Nb-(Y, Gd) is detrimental to the GFA.

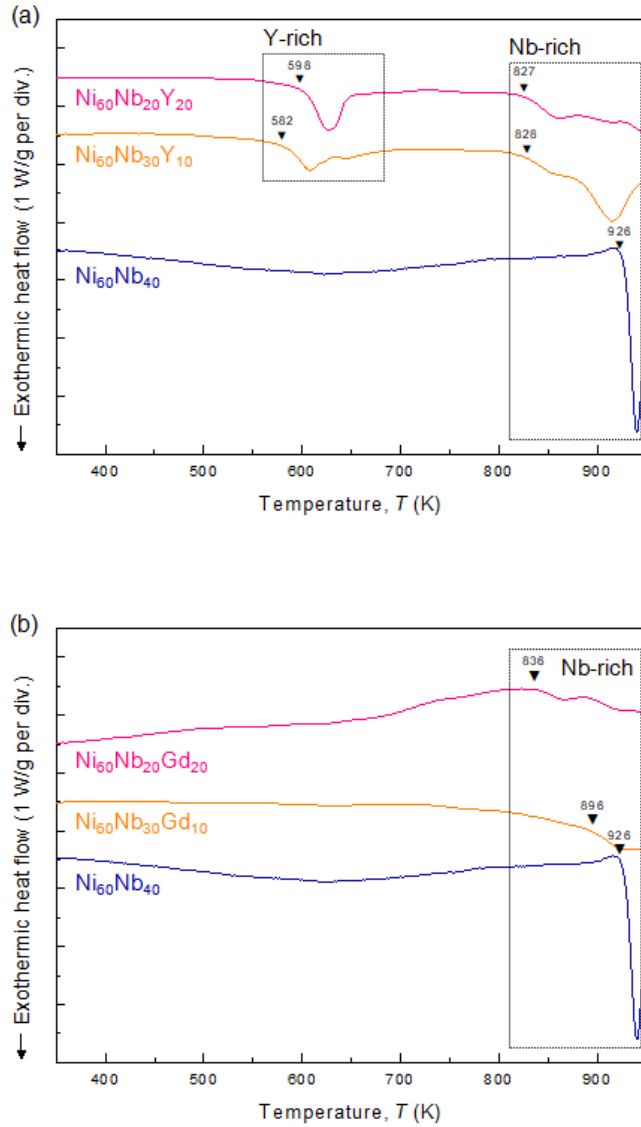


Figure 3.11. DSC traces obtained from (a) melt-spun $\text{Ni}_{60}\text{Nb}_{40-x}\text{Y}_x$ ($x = 0, 10, 20$ at.%) and (b) $\text{Ni}_{60}\text{Nb}_{40-x}\text{Gd}_x$ ($x = 0, 10, 20$ at.%) ribbons.

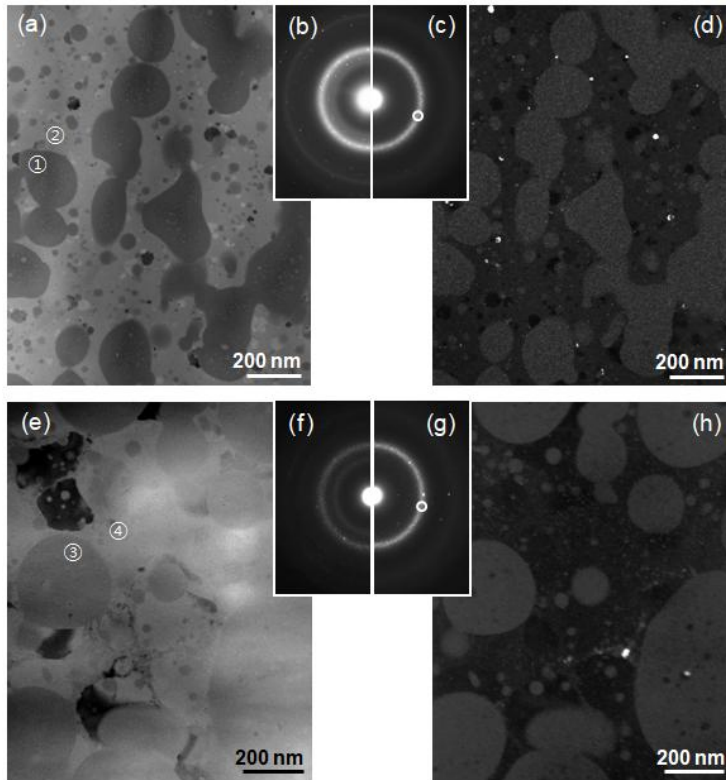


Figure 3.12. (a) TEM BF image of melt-spun $\text{Ni}_{60}\text{Nb}_{20}\text{Y}_{20}$ ribbon. (b) and (c) SADPs obtained from region with a diameter of 500 nm including dark area ① and bright matrix ② at the same time and 200 nm including only ①, respectively. (d) DF image obtained by positioning the objective lens aperture on the outer halo ring in (c). (e) TEM BF image, (f) and (g) SADPs for the region with a diameter of 500 nm encompassing ③ and ④ and 200 nm including only ③, respectively. (h) DF image obtained by positioning the objective lens aperture on the outer halo ring in (f). Ni-Nb rich amorphous phase in each alloy (① and ③) shows brighter contrast.

3.3.2. Governing factors for manipulating microstructure in phase separating metallic glasses

Figure 3.13 (a) and (b) summarizes the microstructures of Y20 and Gd20, respectively, which were investigated by TEM observation. The primary structure of each alloy reveals the phase separating mechanism of each alloy; the interconnected structure of Y20 originates from spinodal decomposition, whereas the droplet-like structure of Gd20 is attributed to the nucleation and growth mechanism [84]. In addition, the size of primary phases is related to the amount of time until the phase-separated liquid phases vitrify, thereby providing indirect information on the critical temperature for phase separation [84, 128]. Moreover, the crystallinity is determined by the GFA of each phase. To deepen our understanding of phase separating MGs, we constructed the metastable miscibility gap of each alloy, which has a close correlation with the microstructural evolution and phase separation kinetics [84]. For the Ni-Nb-Y ternary alloy system whose thermodynamic parameters have been previously reported [129], we thermodynamically assessed the miscibility gap using the CALPHAD method in conjunction with Thermo-Calc software. On the contrary, for the Ni-Nb-Gd ternary alloy system whose parameters are not completely available, we constructed a schematic diagram of the miscibility gap in consideration of microstructural differences between Y20 and Gd20.

Figure 3.13 (c) shows the metastable miscibility gap for the

pseudo-binary section between the Ni₆₀Nb₄₀ and Ni₆₀Y₄₀ compositions consisting of binodal and spinodal curves developed by thermodynamic assessment in which only the liquid state (including the supercooled liquid state) and its phase separation were considered. Only interactions among constituent elements in the liquid phase were applied in the thermodynamic calculation of the miscibility gap. The molar Gibbs free energy of a liquid phase (G^{Liq}) can be expressed as the sum of (1) the Gibbs free energy of the pure elements in liquid state (${}^0G_k^{Liq}$), (2) the Gibbs free energy changes contributed from the ideal mixing entropy and (3) the excess Gibbs free energy (${}^{xs}G^{Liq}$), as follows:

$$G^{Liq} = \sum_k x_k {}^0G_k^{Liq} + RT \sum_k x_k \ln x_k + {}^{xs}G^{Liq} \quad (\text{eq 3.5})$$

Here, x_k is the mole fraction of element k. The ${}^0G_k^{Liq}$ values of the pure elements k (=Nb, Ni, Y) in liquid state were taken from the SGTE-Pure database [130], and ${}^{xs}G^{Liq}$ is described by the quasi-regular solution model using the Redlich - Kister polynomials [131] as follows:

$$\begin{aligned}
{}^{xs}G^{Liq} &= x_{Nb}x_{Ni}\sum_{\nu}{}^{\nu}L_{Nb, Ni}^{Liq}(x_{Nb} - x_{Ni})^{\nu} + x_{Ni}x_Y\sum_{\nu}{}^{\nu}L_{Ni, Y}^{Liq}(x_{Ni} - x_Y)^{\nu} \\
&+ x_{Nb}x_Y\sum_{\nu}{}^{\nu}L_{Nb, Y}^{Liq}(x_{Nb} - x_Y)^{\nu} + x_{Nb}x_{Ni}x_Y(x_{Nb}{}^oL_{Nb, Ni, Y}^{Liq} + x_{Ni}{}^1L_{Nb, Ni, Y}^{Liq} \\
&+ x_Y{}^2L_{Nb, Ni, Y}^{Liq}
\end{aligned} \tag{eq 3.6}$$

where ν is the order of the term considered, ${}^{\nu}L_{m,n}^{Liq}$ is the temperature and composition-dependent interaction parameter in liquid state for m-n atomic pairs at the order ν , and $L_{Nb, Ni, Y}^{Liq}$ is the ternary interaction parameters of the liquid state. All the interaction parameters for the binary and ternary pairs used in this study were taken from by N. Mattern et al. [129]. The critical boundary for spinodal decomposition is achieved by the calculation of the stability function (ϕ) [132] using the Mathematica program which is given as

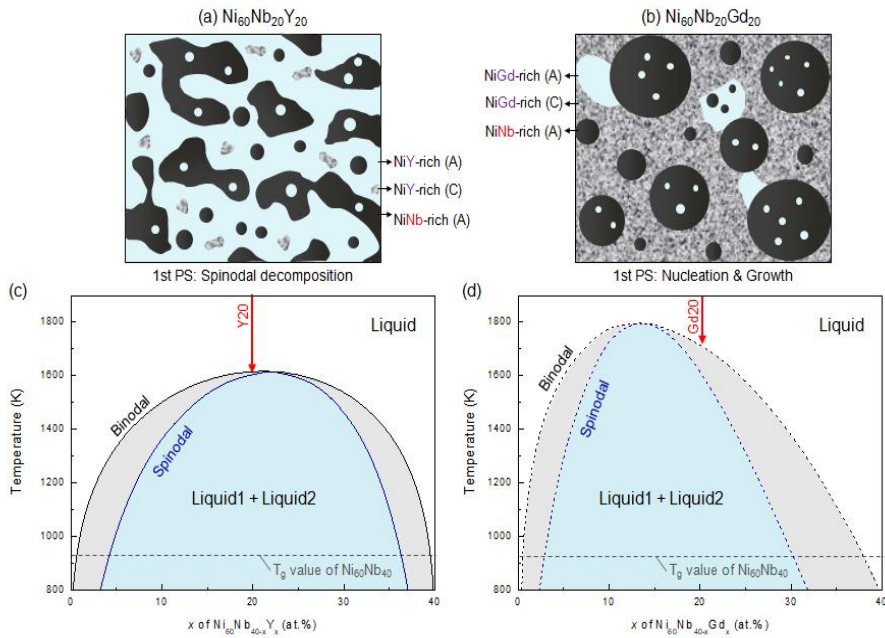
$$\phi = \begin{vmatrix} \frac{\partial^2(G^{Liq}/RT)}{\partial X_{Ni}^2} & \frac{\partial^2(G^{Liq}/RT)}{\partial X_{Ni}\partial X_{Nb}} \\ \frac{\partial^2(G^{Liq}/RT)}{\partial X_{Nb}\partial X_{Ni}} & \frac{\partial^2(G^{Liq}/RT)}{\partial X_{Nb}^2} \end{vmatrix} \tag{eq 3.7}$$

The negative value of ϕ at a certain composition indicates that the alloy system is thermodynamically unstable, in other words, that the composition is in the spinodal decomposition range of the miscibility gap [84, 128]. Thus, the compositional boundary for

spinodal decomposition corresponds to the alloy composition where $\phi = 0$ [128]. The resultant miscibility gap is nearly symmetric; thus, Y20 is expected to undergo phase separation by spinodal decomposition which is in good agreement with the observed microstructure.

The schematic diagram of the miscibility gap for the pseudo-binary section between the $\text{Ni}_{60}\text{Nb}_{40}$ and $\text{Ni}_{60}\text{Gd}_{40}$ compositions was then obtained by comparing the microstructural features of Gd20 with those of Y20, as shown in Figure 3. 13 (d). To be specific, because Ni-Nb rich particles are embedded in the Ni-Gd rich matrix, we can infer that the liquid phase of Gd20 is separated by the nucleation and growth mechanism [84].

In addition, the greater size of dark gray particles in Gd20 in comparison to the width of the interconnected layers in Y20 implies the possibility of Gd20 having a higher critical temperature for phase separation than Y20 [128]. Hence, the metastable miscibility gap is expected to have an asymmetrical shape whose critical temperature is higher than that of $\text{Ni}_{60}\text{Nb}_{40-x}\text{Y}_x$.



① Composition/ ② Symmetry	③ Critical temperature	④ Glass-forming ability
Phase separating mechanism	Size	Crystallinity

Figure 3.13. (a) and (b) Schematic diagram of phase separated microstructures of $Ni_{60}Nb_{20}Y_{20}$ and $Ni_{60}Nb_{20}Gd_{20}$, respectively. (c) and (d) Metastable miscibility gap for the liquid phase at pseudo-binary section of $Ni_{60}Nb_{40-x}Y_x$ and $Ni_{60}Nb_{40-x}Gd_x$ ($0 \leq x \leq 40$ at.%), respectively. The former was calculated by thermodynamic parameters, while the latter was constructed based on microstructural differences between $Ni_{60}Nb_{20}Y_{20}$ and $Ni_{60}Nb_{20}Gd_{20}$. Dashed lines represent the glass transition temperature (T_g) of $Ni_{60}Nb_{40}$.

3.3.4. Discussion

Based on these results, it can be concluded as shown in the table inserted in Figure 3. 13, that the microstructural variation upon the addition of elements having large positive ΔH^{mix} with the constituent elements depends on four variables: ① the composition of an alloy, ② the symmetry of the miscibility gap which determines the phase separating mechanism, ③ the critical temperature influencing the size of phase separated structures, and ④ the GFA of each phase governing the crystallinity.

3.4. Summary

We investigated the effect of alloying elements having different magnitudes of positive ΔH^{mix} with constituent elements on the microstructure and mechanical behavior of MGs. The findings can be summarized as follows. (1) A large positive ΔH^{mix} between constituent elements induces phase separation and deteriorates GFA drastically as seen in Ni-Nb-(Y, Gd) alloy system. The phase separated microstructures of an alloy relies on four different variables (the composition of an alloy, the symmetry of the miscibility gap, and the critical temperature, and the GFA of each phase governing the crystallinity) and lead to a weak interface resulting in extreme brittleness. (2) When a limited amount of an alloying element having

small positive ΔH^{mix} (Zr) is added, atomic scale chemical heterogeneities can evolve because positive ΔH^{mix} between Nb and Zr promotes preferential coordination of Nb with Nb or Ni instead of Zr. These heterogeneities lead to the enhancement of plasticity by facilitating the formation of multiple shear bands in conjunction with a high concentration of potential sites for shear band nucleation (chemically-induced soft spots). As the length scale of heterogeneities depends on the cooling rate, the optimum composition for plasticity can vary in samples of different diameters. In 1 mm bulk specimens, Zr8 and Zr10 samples that had fully amorphous phase exhibited improved ε_p up to approximately 3% with high σ_f of about 3,100 MPa. These results provide an effective guideline for manipulating microstructures and improving mechanical properties (ε_p and σ_f) as well as GFA through the alloying of elements having positive ΔH^{mix} with constituent elements.

Chapter 4.

Development of tailor made metallic glasses by controlling process

4.1. Introduction

Conventional manufacturing technologies still have limitations, such as dimensions of amorphous parts, design freedom of parts, and necessity of tools. Additive manufacturing technology is emerging as an alternative in contrast with traditional manufacturing methodologies. Parts are built in the bottom-up manner. Therefore, complex designed BMG parts are directly built without any tools in powder bed fusion additive manufacturing.

In the melting-solidification pathway, molten BMG should be cooled faster than the critical cooling rate. On the other hand, solid-state crystallization should be avoided in powder metallurgy technology of amorphous powder feedstock. In order to overcome constraints, metal powder bed fusion (PBF) additive manufacturing (AM) was considered in the present study. Metal powders are layered on build platform at a certain thickness. After that, a sliced 2D model from a 3D model is translated onto the powder layer by laser scanning. A physical 3D part is directly built in layer-wise fabrication.

In laser welding, the heating-cooling thermal cycle is largely dependent on the energy density of the laser and it is as fast as approximately 10^5 K/s. Thus, complex and large BMG parts maybe built when process parameters are optimized and both solidification crystallization and solid-state reheating crystallization are avoided. This study focused on assessing the feasibility of using BMG powder for laser PBF AM. Phase evolutions, microstructural features, and mechanical properties were investigated in relation to laser processing parameters.

With respect to the powder feedstock, powder properties have critical influences on processing ability and the properties of fabricated parts. Optimum powder characteristics, such as powder size distribution and morphology, need to be indentified. Practically, the economics of laser PBF AM is primarily determined by the cost of materials. Therefore, unused powders in remaining in the building chamber are recycled after parts are built. Inaddition, BMG powder characterization and the recyclability of unused BMG powder were considered from the viewpoint of process qualification. In the case of BMG powder, phase composition as well as chemical composition and physical powder properties should be monitored during recycling.

4.2. Printable powder preparation for additive manufacturing

4.2.1. Powder preparation

Figure 4.1 shows a protocol for feedstock powder preparation. Top-cut sieving with 106 μm -mesh sieve was conducted for as-atomized powder and then the powder was classified into -25 μm , +25/-53 μm , +53/-75 μm , and +75/-106 μm powders. Powder flowability and packing density were measured according to ASTM standard test procedures [133]. Powder buildability was finally evaluated using a PBF machine. As-atomized and classified powders were not layered. Therefore, acidic pre-treatment and heat-treatments were conducted. The atomized powders were immersed in oxalic acid for 30 minutes and were then rinsed with distilled water 3 times. Two different peak temperatures were chosen for powder heat treatment. Isothermal heat treatments were conducted at 423 K for 2 hours and 873K for 12 hours in a vacuum environment. The former heat-treated powder was amorphous but the latter heat-treated powder was fully crystallized. The 423K heat treatment has no influence on powder layering. The acid-treated powders passing through a 25 μm sieve were well distributed on the build platform but crystallized powders over 53 μm were successfully layered [Figure 4.2].

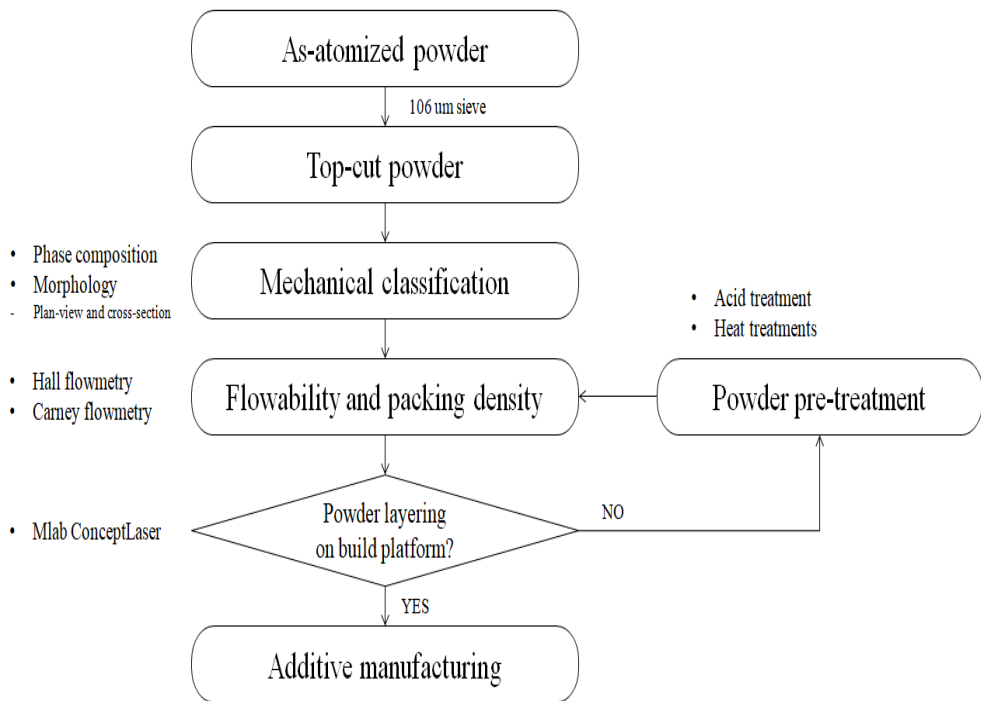


Figure 4.1. Powder preparation procedure.

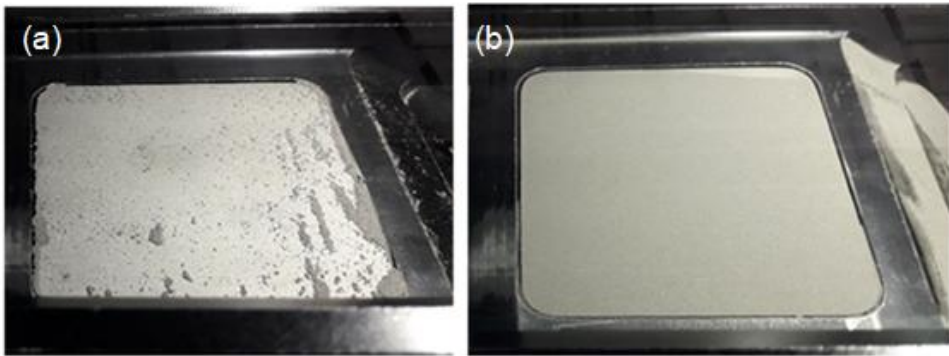


Figure 4.2. Layering ability of powders on the build-platforms; (a) poor and (b) good.

4.2.2. Powder property characterization

The morphologies of the as-atomized powder, powder under 25 μm , and powder above 106 μm are shown in Fig. 4.3. Spherical, elongated, long-tailed, and aggregated particles were observed in as-atomized powder. As the particle size increased, their sphericities were greatly improved but the particles were easily agglomerated. Long-tailed particles were mostly filtered by the 106 μm sieve. Internal pores were frequently observed in the as-atomized powders as shown in Fig. 4.3 (b).

Top-cut and under-cut of as-atomized powder were conducted. Fine powders are prone to agglomerate. On the other hand, layer-wise building results in a stair-case effect, and correspondingly, surface roughness is deteriorated with increased layer-thickness. In this regard, the maximum size of powder feedstock is limited according to powder layering thickness. In fact, metal powders for PBF have a size distribution from 25 μm to 50 μm and powder layering thickness ranges from 25 μm to 50 μm .

The morphologies and phase compositions of the classified BMG powders are presented in Fig. 4.4. The particles of the +25/-32 μm fine powder are spherical, but they still agglomerate. As the powder size increases, the probability of elongated particles and corrugated particles increases. Regarding phase composition, the X-ray diffraction patterns reveal that BMG powder is partially crystallized and crystallinity increases with increasing particle size.

Atomization is the process in which molten liquid is broken into droplets through capillary instability due to interaction with the force gas stream. The morphology of broken droplets is largely dependent on the processing parameters and the thermo-physical properties of the material. The formation of elongated and long-tailed particles is estimated from the Ohnesorge number. Two specific times which are related to capillary instability and spinnability are considered in relation to morphological evolution of molten droplets [134]. In the case of BMG melt, molten liquid is supercooled far below the melting point before vitrification or solidification. The viscosity of a liquid is exponentially increased as supercooling increases, as expected from the Vogel-Fulcher-Tammann (VFT) equation [135]. Therefore, the Ohnesorge number is shifted to prefer spinning of molten droplets to spheroidization as supercooling is enhanced. In the literature [136], the relationship between the molten melt temperature and the long-tailed powder fraction is proven: the lower the molten metal temperature is, the higher the wire fraction is. Molten droplets are rapidly cooled during flight via convective heat transfer with surrounding gas. The cooling rate is largely dependent on the molten droplet size. In the literature [137], the cooling rate of atomized Al-4wt.% Cu powder is estimated by secondary dendrite arm spacing measurement. As the droplet size increases, the cooling rate markedly decreases: 320 K/s for +150/212 μm powder and 11,000 K/s for -38 μm powder. Accordingly, the prominence of the crystalline

peak in coarse BMG powder can be attributed to the lower cooling rate.

The packing behaviors of the powders are summarized in Table 4.1. All the powders did not flow in both Hall flowmetry and Carney flowmetry tests, except the oxalic acid pre-treated powders. The flowability of the oxalic acid pre-treated +32/-53 μm powder was 11.8 s/50 g through a Carney funnel. In addition, its apparent density was significantly low, but its powder packing density was markedly increased by tapping. The Hausner ratio (tap density/apparent density) is another measure of powder compressibility. In general, a powder having a Hausner ratio greater than 1.25 is considered to flow poorly. Acid pre-treatment of as-atomized BMG powder increases the apparent density and decreases the Hausner ratio. It should be noted that acid pre-treatment of BMG powder has a substantial influence on both its free flowability and packing behaviors.

In PBF AM, powders are pre-placed by a sweeping recoater. Uniform distribution of powders is necessary for laser building. The layering ability of a powder can be defined by its uniform distribution on the build platform in an AM machine. Regardless of size distribution, the as-atomized powders were not placed on build platform. To improve layering ability, powder pre-treatments were carried out; acid treatment and crystallized heat treatment were effective.

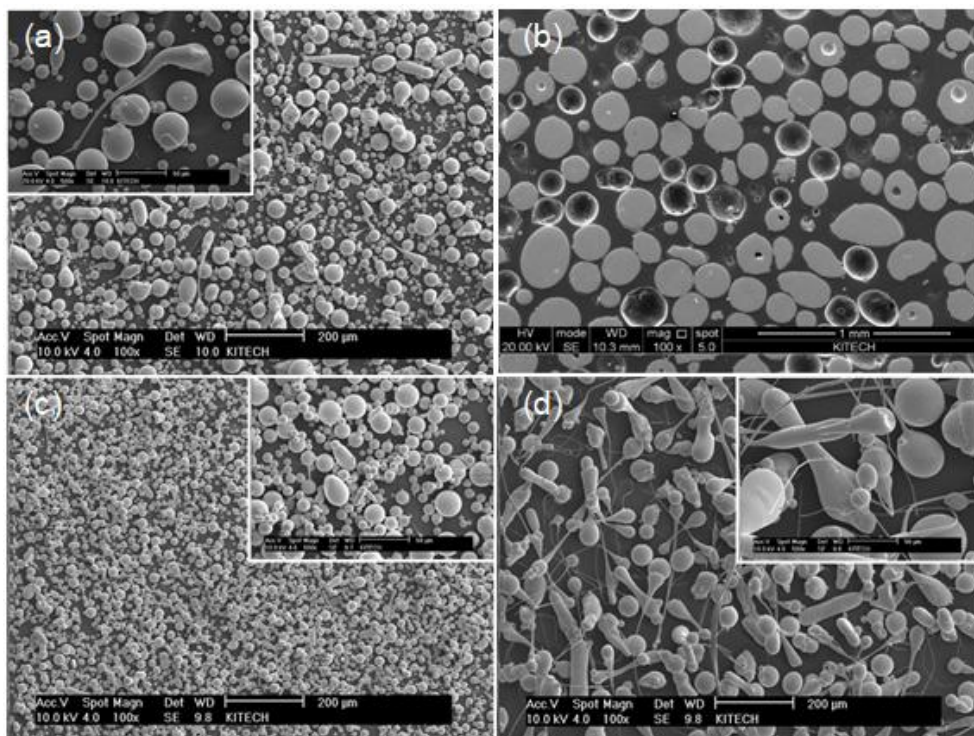
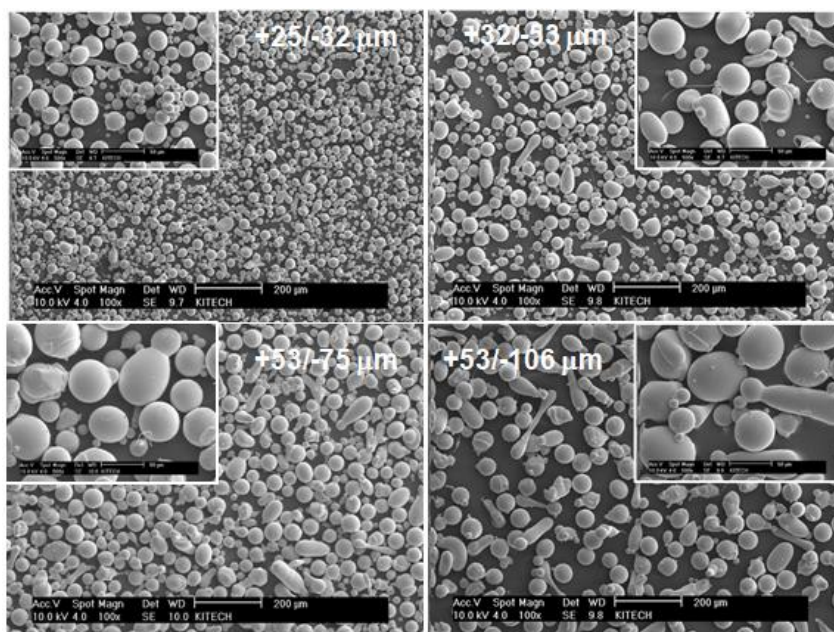


Figure 4.3. Morphology of as-atomized powder; (a) plane-view, (b) cross-section view, (c) powder with particles smaller than 25 μm and (d) powder with particles larger than 106 μm .

(a)



(b)

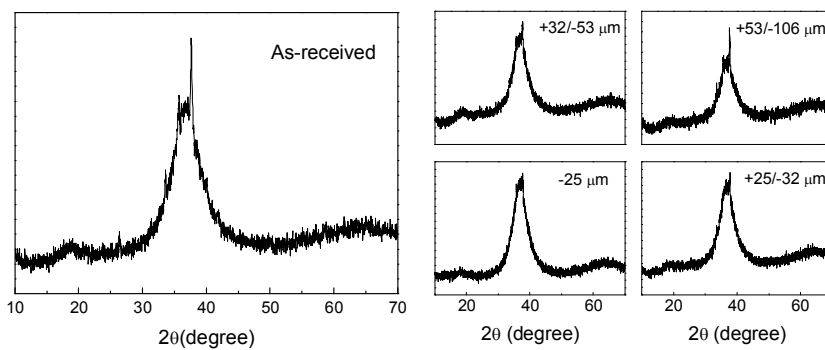


Figure 4.4. Characteristics of prepared powders ; (a) Morphology of powders of each size and (b) XRD results of powders of each size.

Powder feedstock		Flowability		Packing behavior		
Designation	Size	Hall	Carney	Apparent density (A)	Tap density (B)	Hausner ratio (B/A)
As-atomized	+25/ -32	-	-	2.82	4.17	1.48
	+32/ -53	-	-	3.03	4.17	1.38
	+53/ -75	-	-	2.84	4.17	1.47
	+75/ -106	-	-	2.80	4.08	1.46
Oxalic acid treatment	+32/-53	-	11.8	3.48	4.18	1.20
Heat treatment	+53/ -75	-	-	2.96	4.17	1.41

Table 4.1. Powder properties in relation to packing behavior

4.2.3. Discussion

As previously mentioned, no morphological differences after pre-treatments were identified; therefore, powder surface properties have influences on layering ability. In other unpublished result, both pre-treatments improved the layering ability of inert gas atomized STS 316L powder. Thus, removing the surface oxide layer from as-atomized powder reduces interaction between powders.

The surface properties of the powders were further investigated. TEM results were obtained from the as-atomized powder and acid-treated powder via focused ion beam milling. The as-atomized powder was found to be fully amorphous. However, a crystallized layer developed on the surface after acid treatment [Figure 4.5]. It is supposed that such surface crystallization influences inter-particles reactions, although the exact reasons for crystallization and improved buildability have not been clarified in this study. Successful pre-placement of crystallized powder with +53/-75 μm size distribution can be another proof for the effects of surface crystallinity on powder layering ability. In summary, $\text{Zr}_{65}\text{Cu}_{17.5}\text{Al}_{7.5}\text{Ni}_{10}$ BMG powder with appropriate layering ability was prepared by mechanical sieving and powder pre-treatment.

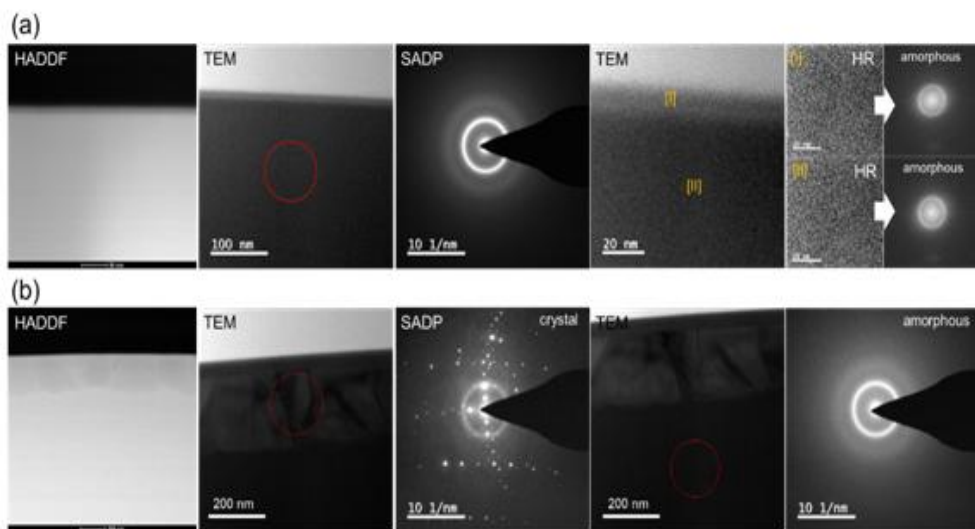


Figure 4.5. Comparison of surface properties of (a) as-atomized powder and (b) acid-treated powder.

4.3 Feasibility assessment of laser powder bed fusion additive manufacturing

4.3.1. Building strategy

Acid-treated amorphous powder with +32/-53 μm size distribution and crystallized powder with +53/-75 μm size distribution were chosen as feedstocks for laser PBF AM. The laser process parameters are summarized in Table 4.2. The powders were baked at 373 K for 2 hours in an inert atmosphere before building. Although it is not a direct indicator for part properties, volumetric energy density is a common measure for the energy input of laser processing. When the laser power, hatch distance, and layer thickness are constant, the volumetric energy density is inversely proportional to the laser scan rate;

$$E = \frac{P}{vht} \quad (\text{Eq 4.1})$$

where E is the volume energy density(J/mm^3), P is laser power(W), v is laser scan rate(mm/s), h is the Hatch distance(mm), and t is the powder layer thickness(mm).

Powder feedstock		Laser parameter		Layer thickness (μmm)	Hatch distance (μmm)	Volumetric energy density (J/mm^3)
Size distribution		Power (W)	Scan rate (mm/s)			
Amorphous powder	+32 /-53 μmm	90	500	25	85	84.7 (1-1)
			750			56.5 (1-2)
			1,000			42.4 (1-3)
			1,600			26.5 (1-4)
Crystallized powder	+53 /-75 μmm	90	500	50	85	42.4 (2-1)
			750			28.2 (2-2)
			1,000			21.2 (2-3)
			1,600			13.2 (2-4)

Table 4.2. Process parameter of laser PBF AM

4.3.2. Characterization output of laser PBF AM

It is worth noting that swelling and severe warping were observed for the 1-1, 2-1, and 2-2 parts (Table 4.2). In particular, spontaneous fracturing occurred for the 2-1 and 2-2 parts during building. The laser scan rate affects the phase composition of the BMG parts Fig. 4.6. As the scan rate decreases, the crystallinity of the as-built part increases. The same behavior was observed for parts fabricated from crystallized powder.

Figure 4.7 shows the microstructures of parts as-built from amorphous powder feedstock: (a), (b), (c), and (d) are back-scattered electron photographs but (e) and (f) are secondary electron photographs. In the back-scattered electron images, three contrasted regions are discerned. The gray region is amorphous, the dark gray region is crystal, and the black region corresponds to pores. The 1-1 part shows a prominent band-like structure having a constant interval which is similar to the Hatch distance. The dark grayed band is crystallized as identified in (a-1) of Fig. 4.7(a). The 1-2 and 1-3 parts have the same crystallized band-like structure but the crystallinity is markedly lowered. Particulate crystals are dispersed in a bank-like structure. The 1-4 part contains little crystalline phase as shown in Fig. 4.7(d). Relatively dense microstructures are observed in the parts. Superficially, the porosity is somewhat higher in 1-1 than 1-4 as seen by comparison of Fig. 4.7 (e) and (f). This implies that the molten pool is sufficiently overlapped laterally and vertically at the given

Hatch distance and powder layering thickness.

The parts built from crystallized powder show quite different microstructures as seen in Fig. 4.8. Coarse pores and particle-shaped microstructures are observed. Coarse pores result from insufficient filling of the molten pool during melting-solidification and partially melted powders are entangled around the coarse pores. In the back-scattered images, the dark gray regions with crystalline phases are of a particular shape. The probability of a crystallized region is high around coarse pores. The dark gray crystallized region is much larger in 2-3 than in 2-4. In the dense region, band-like crystalline regions were not observed for either 2-3 or 2-4. This means that crystallization of the parts as-built from crystallized powder was different from that of parts as-built from amorphous powder.

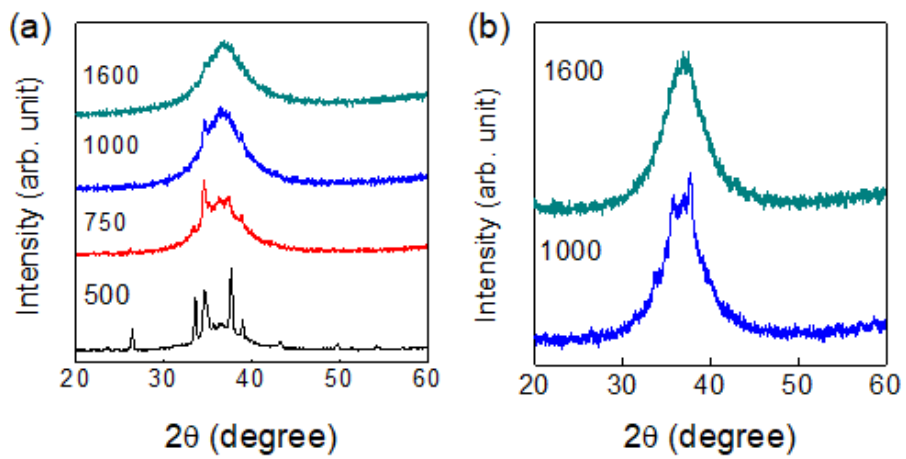


Figure 4.6. Phase composition of parts as-built (a) from amorphous powder and (b) from crystallized powder

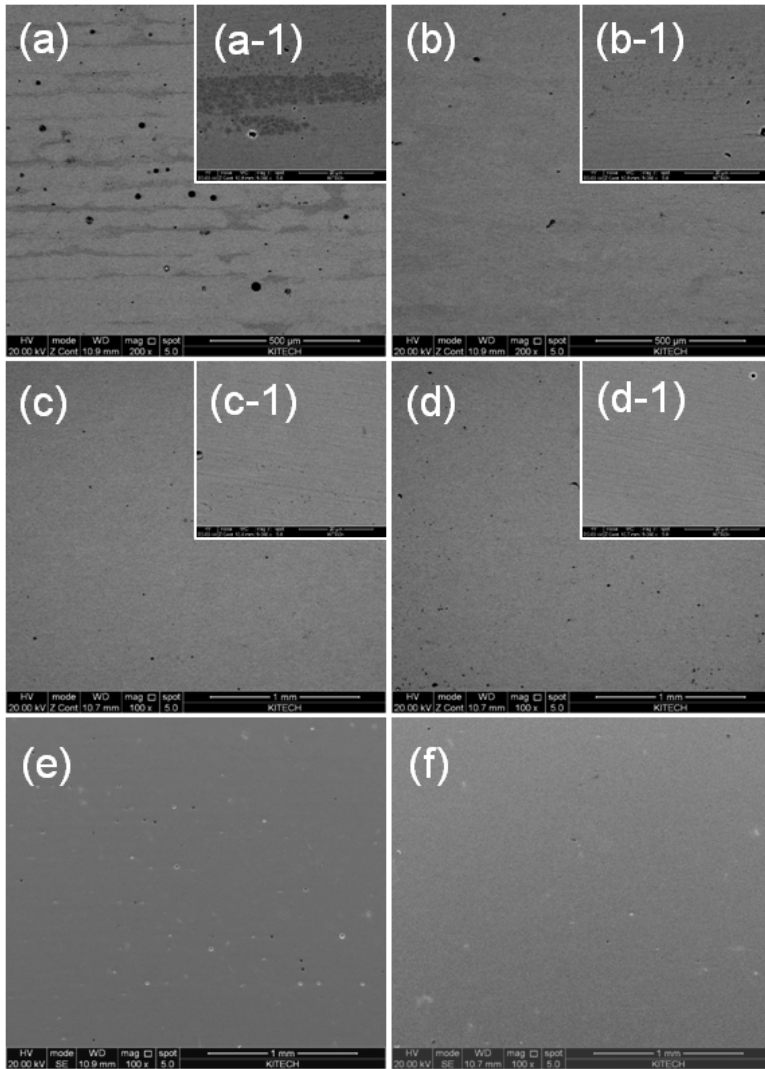


Figure 4.7. Microstructures of parts built from amorphous powder: (a) BSE image of 1-1(90W-500mm/s) part, (b) BSE image of 1-2(90W-750mm/s) part, (c) BSE image of 1-3 (90W-1,000mm/s) part, (d) BSE image of 1-4(90W-1,600mm/s) part, (e) SE image of 1-1(90W-500mm/s) part, and (f) SE image of 1-4 (90W-1,600mm/s) part.

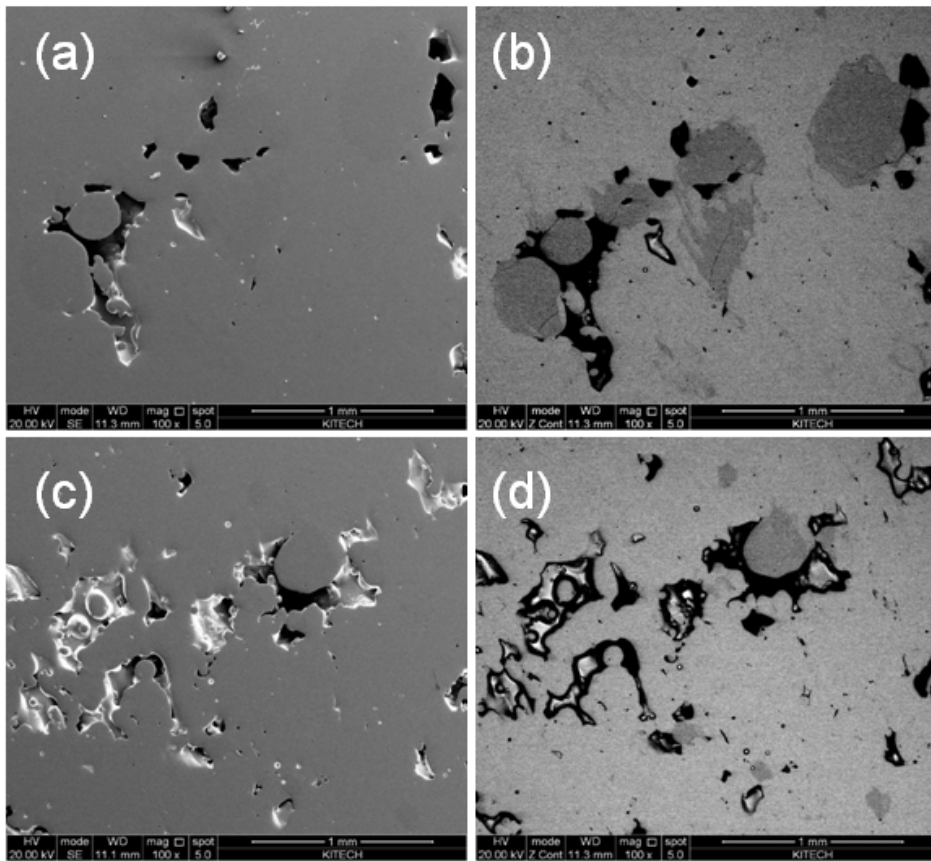


Figure 4.8. Microstructures of parts built from crystallized powder: (a) SE image of 90W-1,000mm/s part from crystallized powder, (b) BSE image of (a), (c) SE image of 90W-1,600mm/s part from crystallized powder, and (d) the BSE image of (c).

Laser powder bed fusion AM was performed using both amorphous powder and crystallized powder. The results show that amorphous parts can be obtained using laser PBF AM. Phase composition and defect microstructure are the target properties for fabrication of the BMG part. Crystallization and defect microstructures are determined in terms of the volumetric energy density of the laser.

In laser PBF AM, a laser is irradiated onto the powder layer and scanned using galvano-mirror system. Owing to the nature of the point source, a spatial temperature gradient is generated, schematically shown in Fig. 4.9 (a). Phase evolution of the weld zone is primarily dependent on peak temperature and cooling rate. After a single sweep of the laser, the weld zone is divided into weld metal, heat affected zone (HAZ), and base metal. The weld metal undergoes melting and subsequent solidification. The peak temperature is lower than the melting temperatures of both HAZ and base metal, and the separation of HAZ and base metal is determined by microstructural changes and phase transformation. Thus, most engineering alloys have complex phase compositions and different microstructures in the weld zone.

Within the scope of this study, crystallization was observed in HAZ regardless of powder feedstock. Regarding the phase evolution of BMG weld, crystallizations in the weld metal and HAZ were different. The molten pool is cooled by conductive heat dissipation. The crystallization start line is determined by the chemical

composition of the BMG material, schematically represented in Fig. 4.9 (b).

If the cooling rate (A-1) is faster than the critical cooling rate that avoids the nose of the crystallization start line, the molten pool is vitrified. In contrast, a molten pool with A-2 cycle results in a crystallized weld metal. Heating rate-dependent crystallization has no influence on the phase composition of the weld metal because the crystallized solid is remelted during heating, implying that the phase composition of the starting powder feedstock is not a decisive factor for the as-built part crystallinity once the powders are fully melted during heating. In addition, vitrification of the molten pool is determined by its cooling rate during laser processing. It enhances the BMG material selectivity because the cooling rate of laser PBF is much higher than that of inert gas atomization. It is empirically supported herein by amorphous part building from the crystallized powder.

On the other hand, the heating and cooling thermal cycles should be considered for the crystallization of HAZ. The B-1 thermal cycle avoids solid-state reheating crystallization but the B-2 cycle intercepts the crystallization start line. The reheating thermal cycle is also dependent on the volumetric energy density. Lower energy density results in a faster reheating thermal cycle. The 1-1 part having volumetric energy density 84.7 J/mm^3 crystallized HAZ, while the 1-4 part with 26.5 J/mm^3 was amorphous. Layer thickness of the

parts from the crystallized powder, were two-times thicker than those from the amorphous powder layer, and the volumetric energy density was accordingly half at the same laser parameters. The crystalline phase was not observed in the fully melted region, corresponding to the results of the amorphous powder part. However, particulate crystalline regions were observed for the crystallized powder parts. This closely related to hatch distance, which is the lateral interval between neighboring laser scans. Molten pool volume decreased with decreasing volumetric energy density. If sufficient overlap exists between weld metals, a discontinuity is formed. If HAZ crystallization occurred before the laser scan and it was not remelted subsequent to the laser scan, a crystal phase remained in the as-built part.

The reason for the 2-3 and 2-4 parts having HAZ crystallization, despite their having lower volumetric energy densities than the 1-4 part, remains unclear. The parts were sequentially formed by building weld metal line-wise on a pre-placed powder layer. Therefore, heat transfer was asymmetric because one side of the molten part was solid and the other side was powder. Heat conduction may be faster through the solid part than the powders. Therefore, crystallization occurred in the powder region. However, the crystallized powder remelted during the subsequent laser scan when there was sufficient overlap, similar to amorphous powders. In contrast, the powder region HAZ was not remelted and remains in the crystallized powder parts. The crystallized regions were mainly

located at discontinuities in the as-built parts.

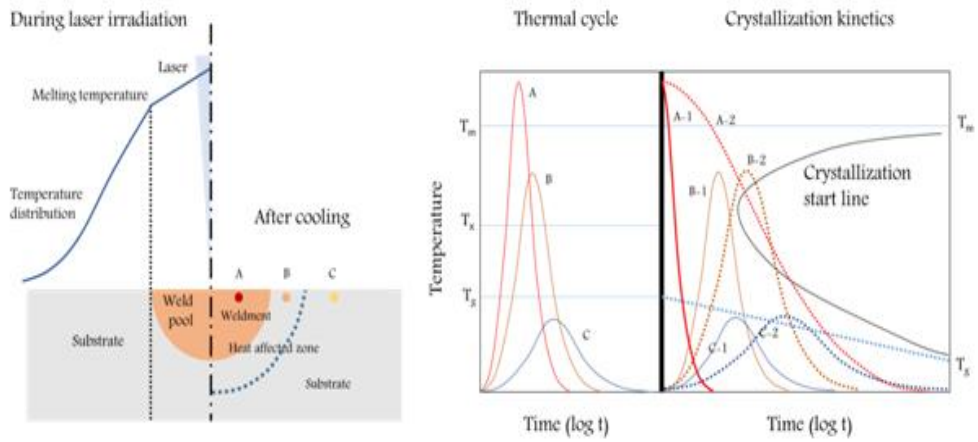


Figure 4.9. Estimation of thermal cycles and phase evolutions of bulk metallic glass parts during laser PBF process; (a) cross-sectional view of the weld zone, and (b) competition between thermal cycle and crystallization kinetics of the BMG weld zone

4.3.3. Mechanical properties on output of AM

To compare relative the mechanical properties of bulk specimens prepared by AM, the volumetric energy density can be changed by controlling the hatch distance of laser PBF AM. As shown in Figure 4. 10, three different samples were fabricated by varying the hatch distance; 65 μm , 85 μm , and 125 μm . we denote these 3D printed samples by their hatch distance as ' δ AM' (e.g. 65 AM for 65 μm hatch distance as shown the table inserted in Figure 4. 10).

Fig 4.11 (a) shows the XRD patterns of samples fabricated by different methods; suction-casting (SC), spark plasma sintering (SPS), and 3D printing. The XRD pattern of each sample consisted of a broad halo peak only; no sharp peaks corresponding to crystalline phase were observed, which indicates that all specimens were composed of a glassy phase. For further investigation, DSC curves were obtained by heating the samples to 850K, at rate is 40K/min, as shown in Fig 4.11 (b). The onset temperature for the crystallization (T_x) of each samples was similar to 756K. However, the crystallization enthalpy (ΔH) of the specimen AM 65 was smaller than that of the suction-cast sample. This should originate from partial crystallization during AM. As the volumetric energy density increased when hatch distance decreased, AM 65 had the highest volumetric energy density, (as depicted in the table inserted in Figure 4. 10.) and it was partially crystallized.



Designation	Laser power (W)	Laser scan speed (mm/s)	Layering thickness (mm)	Hatch distance (μm)	Volumetric energy density (J/mm^3)	Power size (μm)
AM 65	90	1,600	0.025	65	34.6	+32/-53
AM 85	90	1,600	0.025	85	26.5	
AM 125	90	1,600	0.025	125	18.0	

Figure 4.10. The shapes and conditions of three different samples fabricated by varying the hatch distance (65 μm , 85 μm , and 125 μm).

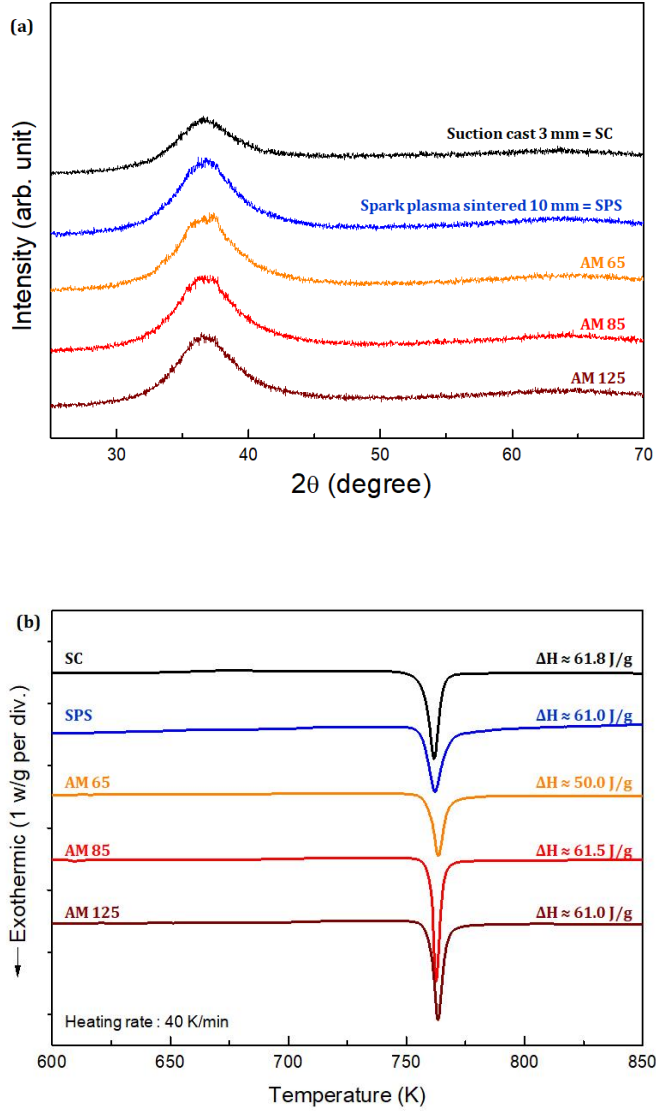


Figure 4.11. (a) XRD patterns and (b) DSC curves of samples fabricated by suction-casting(SC), spark plasma sintering(SPS), and 3D printing.

Figure 4.12 shows optical microscopy images of the specimens. The suction-cast specimens exhibited few pores in the OM images; SPS, and AM 65, and AM 85 showed less than 0.1 % porosity. Only AM 125 (which had the largest hatch distance) exhibited low packing density (approximately 85 %). BMG samples were indented with an applied load of 10kg and the Vickers hardness obtained from the five different samples are shown in Figure 4.13. As indicated in Figure 4.13, the SPS and AM specimen exhibited higher Vickers hardness than suction-cast specimens except for AM 125, which had porous structure. So, for further the analysis of structural differences between specimens made by different processes, we chose AM85 as representative. Increases of micro-hardness in SPS and AM specimens can be rationalized by relaxation of metallic glass during the manufacturing process. During the sintering and AM processes, indispensable additional heat is applied which induces overall relaxation and is known to decrease the free volume and increase the hardness of metallic glass. A slightly smaller hardness value of the AM specimen relative to the SPS specimen infers that the AM process induces less relaxation than the SPS process.

To scrutinize the local properties of specimens, we performed nanoindentation tests of the SC, SPS, and AM specimens; a similar hardness trend with macro-hardness was obtained, as shown in Figure 4. 14.

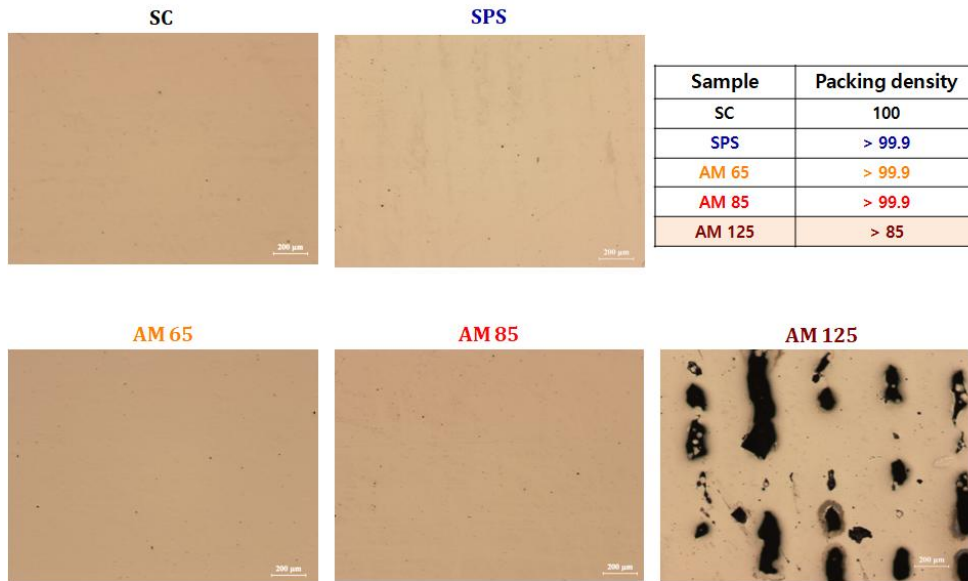


Figure 4.12. Optical microscopy images of samples fabricated by suction-casting (SC), spark plasma sintering (SPS), and 3D printing.

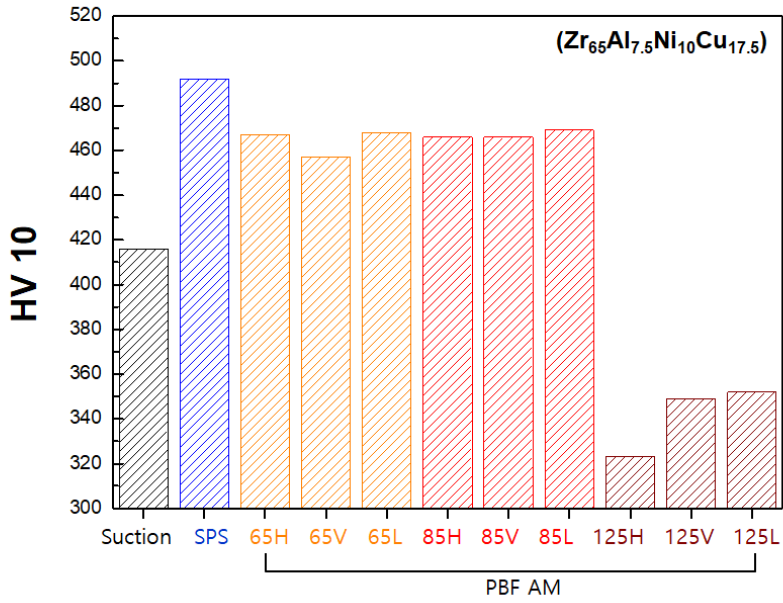
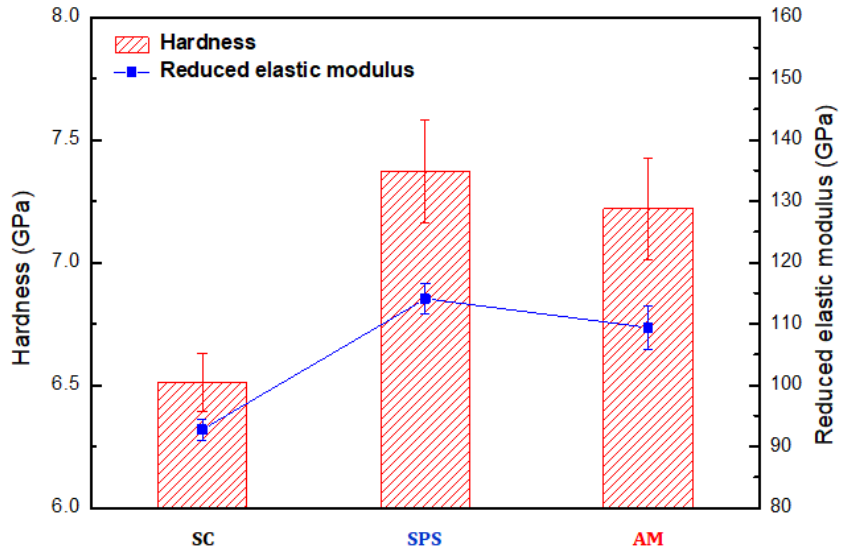


Figure 4.13. Vickers hardnesses obtained from samples fabricated by suction-casting (SC), spark plasma sintering (SPS), and 3D printing.



	Hardness (GPa)	Reduced elastic modulus (GPa)
SC	6.51±0.11	92.8±1.7
SPS	7.37±0.21	114.1±2.38
AM	7.21±0.20	109.4±3.6

Figure 4.14. Macro-hardnesses obtained from samples fabricated by suction-casting (SC), spark plasma sintering (SPS), and 3D printing.

In the load depth curves of the nanoindentation test, the first pop-in event is regarded as the onset of plasticity, and critical shear strength, τ_{\max} , can be estimated as

$$\tau_{\max} = 0.31p_0 = 0.31\left(\frac{6E_r^2}{\pi^3 R^2}P_l\right)^{\frac{1}{3}} \quad (\text{Eq. 4.2})$$

where p_0 and p_m are the maximum and mean pressures of the contact, respectively, and E_r is the reduced modulus.

The cumulative distribution of the estimated τ_{\max} of three specimens (SC, SPS, AM) is illustrated in Figure 4.15. The value of τ_{\max} is consistent with the hardness tendency. Based on Schuh's work, the onset of plasticity during nano-indentation can be analyzed within a nucleation-based statistical framework, so the activation volume V^* can be estimated through the statistical method that relies on the cumulative distribution of the yield strength, as:

$$\ln[\ln(1-f)^{-1}] = \frac{\Delta F^*}{kT} + \ln\left[\frac{kT}{V^*(d\tau/dt)}\right] + \frac{\tau V^*}{kT} \quad (\text{Eq. 4.3})$$

where k is Boltzmann's constant, T the temperature, ΔF^* the Helmholtz activation energy, and V^* the activation energy. From Figure 4.15, which shows a correlation between $\ln[\ln(1-f)^{-1}]$ and τ_{\max} , V^* can be obtained from the slope k (V^*/kT) of the linearly fitted line. Furthermore, Jang et al. suggested the application of a statistical

method to estimate the STZ activation energy in metallic glass, as:

$$W^* = 4R_0 G_0 \gamma_c^2 (1 - \tau/\tau_0)^{3/2} \xi \Omega = \frac{2\tau_0 (1 - \tau/\tau_0) V^*}{3} \quad (\text{Eq. 4.4})$$

where $R_0 \approx 1/4$ and $\xi \approx 3$ are constants, τ and τ_0 are respectively threshold shear resistances at temperatures T and 0 K, G_0 is the shear modulus at 0 K, the average elastic limit $\gamma_c \approx 0.027$, and $\tau_0 \approx 0.036$. The value of τ/τ_0 can be estimated from the constitutive equation:

$$\tau/G = Y_{c0} - Y_{c1} (T/T_g)^{2/3} \quad (\text{Eq. 4.5})$$

where $Y_{c0} = 0.036 \pm 0.002$, $Y_{c1} = 0.016 \pm 0.002$, and the shear modulus G of the a metallic glass has a weak temperature dependence.

The slope of the AM specimen showed the smallest value, which suggests that the AM specimen had smaller STZ activation energy than the other two specimens. The smaller STZ activation energy means that it is easier to activate the STZ and nucleate shear bands, especially at the same composition. The cumulative distribution function of each specimen is depicted in Figure 4.16 (a).

To investigate the variation in intermittent shear avalanches during plastic deformation, we statistically analyzed pop-in events in the nanoindentation results, as discussed in chapter 3.2.2 (depicted in

Figure 4. 16(b)). SC showed a β value that was far smaller than the ideal value of β (≈ 0.5), which indicates a relatively large portion of serration in chaotic condition. Both SPS and AM exhibited β values close to ideal value, as shown in Table 4.3. However, The Sc value was significantly smaller than those of the other two specimens (SC & SPS). A smaller Sc value indicates that the nucleation of chaotic shear bands became easier, which can be connected with the result of Figure 4.15 (smaller STZ activation energy). Hence, both SC (which has β value smaller than ideal) and AM (which has ideal β value but smaller Sc value) can nucleate chaotic shear bands, form multiple shear bands, and show ductility.

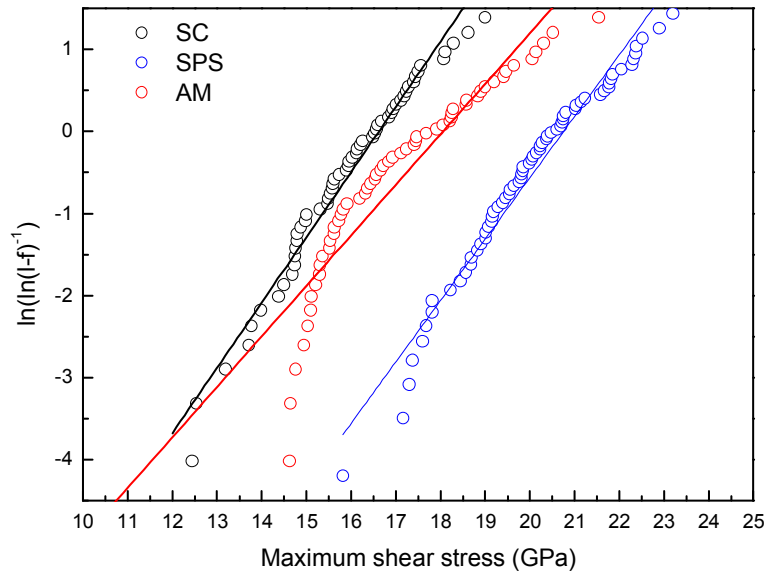


Figure 4.15. Correlation between $\ln[\ln(1-f)^{-1}]$ and τ_{\max} , V^* obtained from samples fabricated by suction-casting (SC), spark plasma sintering (SPS), and 3D printing.

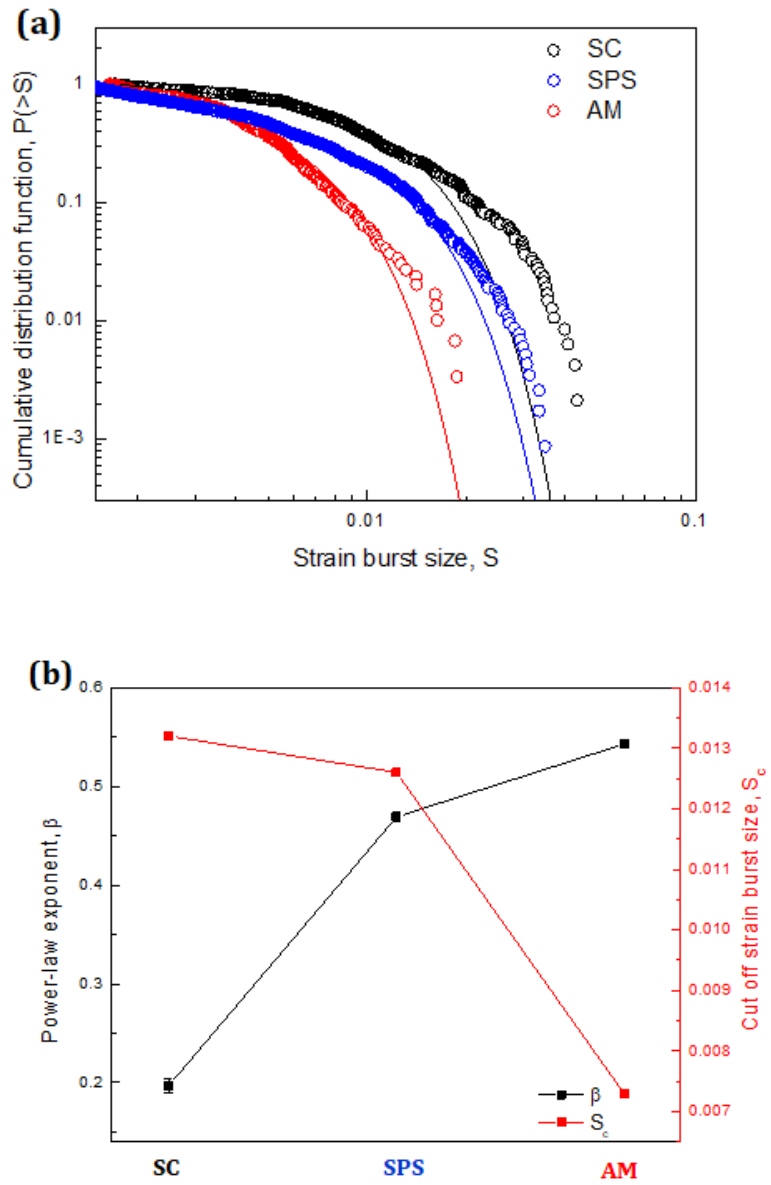


Figure 4.16. (a) The cumulative probability distribution of strain burst sizes, (b) β and S_c values for SC, SPS, AM.

Designation	β	Sc
SC	0.197±0.007	0.0132±0.0001
SPS	0.469±0.001	0.0126±0.0001
AM	0.543±0.004	0.0073±0.0001

Table 4.3. Summary of β and Sc values for SC, SPS, and AM.

4.3.4. Discussion

These mechanical results are attributed to differences of their local structures. The structures of metallic glasses, since they have randomly distributed atomic structures, are significantly affected by thermal history like annealing and cooling rate. Figure 4.17 (a) shows a schematic of the thermal history of each specimen (fabricated by different processes). A 3 mm diameter SC specimen was fabricated by quenching (cooling rate $\approx 10^2$ K/s) and SPS specimen was fabricated by annealing the metallic glass powder at just above the glass temperature. The AM specimen is more complicated because the cooling rate of the melt zone is as fast as 10^5 K/s, but heat is repeatedly applied as the laser passes continuously and causes partial relaxation of the metallic glass. When a metallic glass relaxes, the volume of metallic glass decreases as the total amount of free volume (known as initial deformation site of metallic glass) decreases, as shown in Figure 4.17 (b). Even though some part of the AM specimen relaxed during processing as in the SPS specimen, the AM specimen had parts that passed through fast quenching. Because of this heterogeneity and fast quenching part, the AM specimen contains sites with low activation energy and shear bands that are easy to nucleate.

Optical microscopy images after macroindentation of specimens are shown in Figure 4.18 (a). In the SPS specimen, well-behaved radial cracks were formed at apexes of the indentation,

as normally observed in brittle solids. However, both SC and AM specimens did not show cracks at apexes of indentation, which infers that brittle fracture did not occur under the given conditions.

Figure 4.18 (b) shows the stress-strain curve that was the result of uniaxial compression tests of SC, SPS, and AM specimens. The SC specimen exhibited 1620 ± 20 MPa yield strength and about 1.5 % plasticity (ϵ_f). The SPS specimen only exhibited 1260 ± 20 MPa yield strength even though it had higher hardness than the SC specimen and no plasticity. Normally bulk metallic glasses fabricated by SPS show far less ductility (or even no plasticity) than specimens fabricated by SC. However, the specimen fabricated with AM exhibited 1770 ± 20 MPa yield strength and $\sim 0.3\%$ plasticity. Higher value of yield strength originates from the structural relaxation of AM specimens as shown in hardness trend. However, unlike SPS specimen which also has relaxed structure and showed no ductility, AM specimen exhibited plasticity and some serration which represent arrest of shear bands and formation of multiple shear bands. Higher yield strength and plasticity of AM specimen can be explained by atomic scale heterogeneity which comes from mixture of local fast quenched glass zone from laser fusion and relaxed glass zone from HAZ.

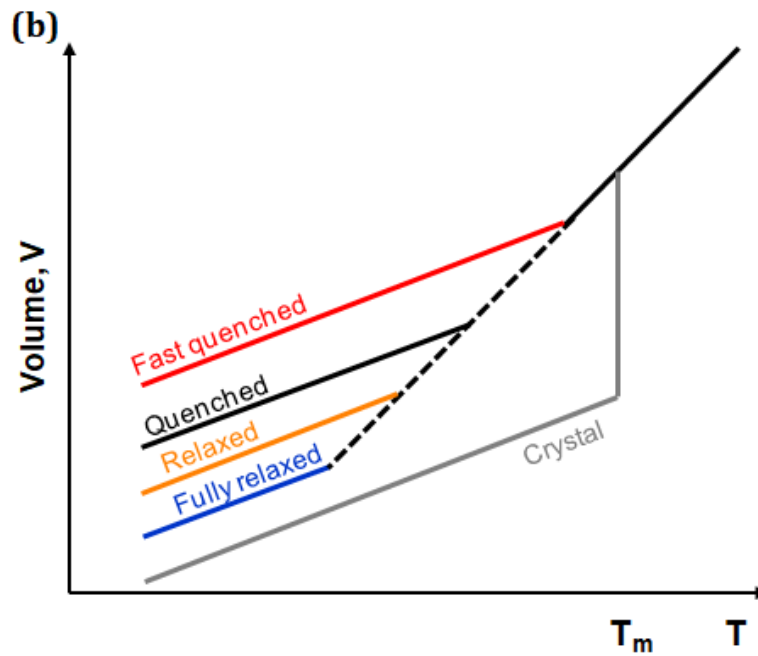
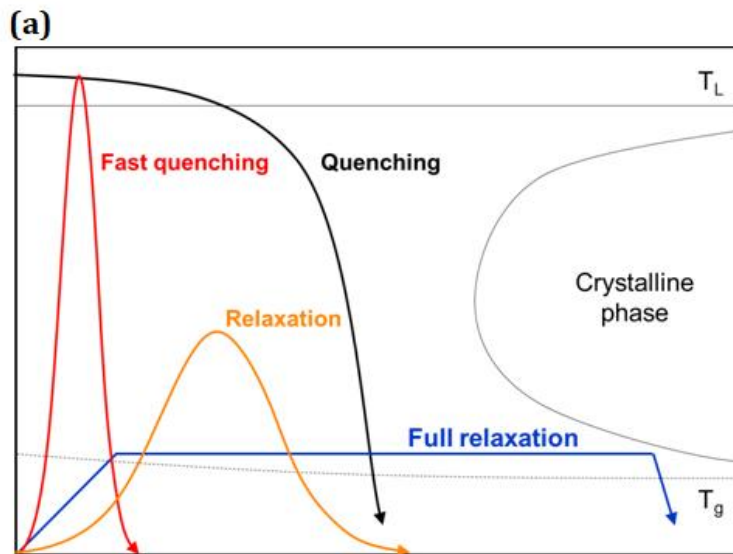


Figure 4.17. (a) Schematic of the thermal histories and (b) total free volumes of SC, SPS, AM.

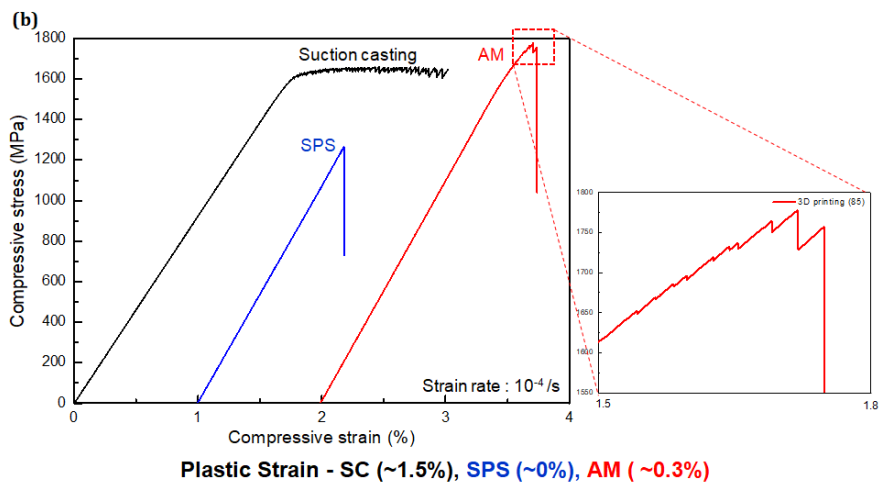
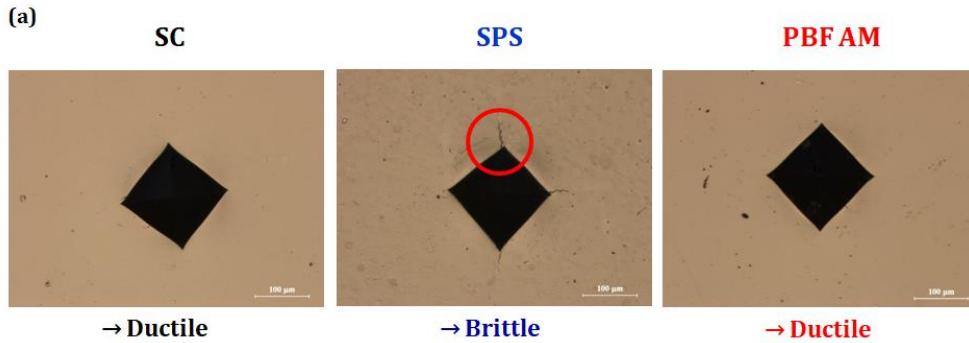


Figure 4.18. (a) Optical microscopy images after macroindentation and (b) the stress-strain curves of uniaxial compression tests of SC, SPS, and AM.

4.4. Summary

$Zr_{65}Cu_{17.5}Al_{7.5}Ni_{10}$ bulk metallic glass powder was produced using an inert gas atomization process. The crystallinity and morphology of the inert gas atomized $Zr_{65}Cu_{17.5}Al_{7.5}Ni_{10}$ powder depended on the particle size. The amorphous degree and sphericity improved as the particle size decreased. The quantities of long-tailed particles and elongated particles reduced significantly. Nevertheless, as-atomized and classified powders were not layered on the build platform owing to severe agglomeration regardless of powder size distribution. Oxalic acid pre-treatment and crystallization pre-heat treatment improved the flowability and layering ability. It is concluded that the surface crystallinity of BMG powder may play a critical role in powder interactions. With respect to the fabrication of a fully amorphous part, the crystal phase and pores are regarded as defect microstructures. In this study, the melting-solidification cooling rate was faster than the critical cooling rate; therefore, crystallization of the weld metal was avoided. As the volumetric energy density decreased, solid-state reheating crystallization diminished for sufficient melting. On the other hand, crystallized HAZ remained when it was not remelted during subsequent laser scanning, even at low volumetric energy density. Laser PBF AM showed high feasibility for scalability in amorphous BMG part fabrication.

The relative mechanical properties of bulk specimens prepared

by AM, SPS, and suction casting were compared with those of bulk specimens manufactured by AM. Some parts of AM specimens relaxed during processing (similar to relaxation occurring in SPS specimens); AM specimen has parts that pass through fast quenching. Because of this heterogeneity and the fast quenching part, AM specimens contain sites with low activation energy and easy to nucleate shear bands. The specimen fabricated by AM exhibited 1770 ± 20 MPa yield strength and $\sim 0.3\%$ plasticity.

Chapter 5. Conclusions

This study investigated two approaches to overcome the limits of application of amorphous materials to structural materials and to suggest new directions for controlling amorphous alloys.

In Chapter 3, we investigated the mechanism by which amorphous structure can be controlled through composition control and by which amorphous brittleness and amorphous forming ability can be improved without loss of strength, even after yielding at room temperature. For this purpose, we added minor amounts of elements with positive heats of mixing and analyzed the effects of the added elements on the structural and mechanical properties of amorphous alloys. When adding a small amount of Zr in the mixing sequence of a Ni-Nb alloy -a simple binary amorphous alloy- EXAFS and XANES analyses (which is an analyzer at the atomic scale), show that local atomic-scale heterogeneity was generated in a monolithic amorphous phase. In addition, the local atomic-scale heterogeneity can provide many sites where shear bands can be generated, thereby preventing sudden destruction by a concentrated shear band and ultimately improving the ductility of the amorphous phase. Nano-indentation and self-designed bending test results on ribbons confirmed the concept. A compression test was carried out to compare with bulk specimens; it was confirmed through compression tests that the local

atomic-scale heterogeneity in a single amorphous phase could simultaneously increase the strength and elongation of the amorphous phase. On the other hand, when Y and Gd which have large heat of mixing relative to the Ni-Nb binary alloy, were added, phase separated amorphous phase was obtained and the added elements Y and Gd were homogeneously amorphous. It was confirmed that the microstructure and thermal properties were very different. Based on the thermodynamic data, it is possible to control the microstructure of the phase-separated amorphous alloy (considering the governing factor) to induce differences in the microstructure and thermal characteristics of the phase-separated amorphous alloy and to design the alloy that can be produced through the amorphous composite concept.

In Chapter 4, amorphous materials were fabricated by 3D printing to study approaches to overcome limitations of the size and shape of amorphous material while retaining the amorphous structure. First, amorphous powders of $Zr_{65}Al_{7.5}Ni_{10}Cu_{17.5}$ were prepared by gas atomization and the processing conditions for powders capable of 3D printing (PBF) (through the pretreatment of powders such as by oxalic acid treatment) were derived. In addition, to find the optimum 3D printing conditions, the optimal heat input condition was established by changing the process parameters of the 3D printing equipment. The relative mechanical properties of bulk specimens prepared by AM, SPS, and suction casting were compared with those

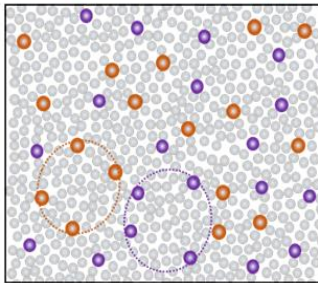
of bulk specimens manufactured by AM. Nanoindentation and compression tests were performed to evaluate the mechanical behaviors of bulk specimens. Local gradient relaxation was induced between the fast quenching region (directly affected by the laser) and the HAZ and substrate regions (indirectly affected by the laser); the local atomic scale heterogeneity due to the difference in asynchronous cooling of atoms due to this temperature gradient was studied. It was confirmed that the strength could be improved and that ductility could be instigated.

Fig. 5.1 summarizes the results of this study. As shown in Fig. 5.1, when a small amount of positive enthalpy was added through a small amount of composition control to induce chemical heterogeneity at the atomic scale and optimization was performed by controlling the cooling rate; the strength and elongation of the bulk amorphous alloy could be improved at the same time. In addition, as a method of process control, homogeneity at the atomic scale was caused by mixing local unrelaxed-relaxed structures by a cooling method inherent to 3D printing, and the concept of overcoming the size restriction of amorphous drawing is proposed.

The new alloy design and process design concept that can produce customized amorphous material to expand the industrial application of amorphous materials will be presented.

▪ **Composition control**

: minor addition of element with small positive enthalpy of mixing
 → **local preferential ordering**



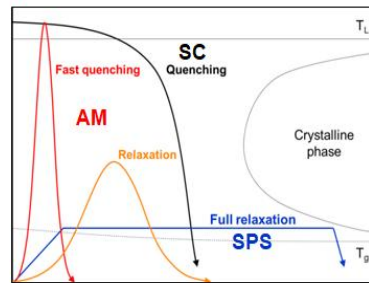
Alloy design + process control
 Optimum atomic scale heterogeneity

↓
 Glass forming ability / Ductility ↑

➔ **Overcome strength-ductility trade off with higher glass forming ability**

▪ **Process control**

: Power bed fusion additive manufacturing
 → unique thermal history
 → **unique local unrelaxed-relaxed structure**



Control of thermal history
 Optimum heterogeneous relaxed structure

↓
 Size with design freedom / Ductility ↑

➔ **Overcoming limited scalability with design freedom & potentially ductility**

Figure 5.1. Summary of this study

Bibliography

- [1] R. Zallen, *The Physics of Amorphous Solids*, John Wiley, New York, (1983).
- [2] W. Klement, R. H. Willens and P. Duwez, *Nature*, 187 (1960) 869.
- [3] L. E. Luborsky (Ed.), *Amorphous Metallic Alloys*, Butterworths, London, 1983
- [4] R. H. Libermann (Ed.), *Rapidly Solidified Alloys*, Butterworths, New York, 1993.
- [5] H.S. Chen and D. Turnbull, *Acta Metall.* 22 (1974) 1505.
- [6] M.C. Lee, J.M. Kendall and W.L. Johnson, *Appl. Phys. Lett.* 40 (1982) 382.
- [7] H.W. Kui, A.L. Greer and D. Turnbull, *Appl.Phys. Lett.* 45 (1984) 615.
- [8] A. Inoue, *Acta Mater.* 48 (2000) 279.
- [9] A. Peker and W.L. Johnson, *Appl. Phys. Lett.* 63 (1993) 2342.
- [10] C. Suryanarayana, A. Inoue, *Bulk Metallic Glasses*, CRC Press, New York(2011)
- [11] Liquidmetal Technologies, [http : //www.liquidmetal.com](http://www.liquidmetal.com)
- [12] M. Ishida, H. Takeda, D. Watanabe, K. Amiya, N. Nishiyama, K. Kita, Y. Saotome and A. Inoue, *Mater. Trans. JIM* 45 (2004) 1239.
- [13] N. Nishiyama, K. Amiya and A. Inoue, *Mater. Sci. Eng. A* 449 (2007) 79.

- [14] C.L. Ma, N. Nishiyama and A. Inoue, *Mater. Sci. Eng. A* 407 (2005) 54.
- [15] A. Inoue, W. Zhang and T. Zhang, *Mater. Trans. JIM* 43 (2002) 1952.
- [16] A. Inoue, T. Shimizu, S. Yamaura, Y. Fujita, S. Takagi and H.M. Kimura, *Mater. Trans. JIM* 46 (2005) 1706.
- [17] N. Nishiyama, A. Amiya and A. Inoue, "Amorphous and Nanocrystalline Metals", R. Busch, T.C. Hufnagel, J. Eckert, A. Inoue, W.L. Johnson, A.R. Yavari, Eds. (*Mater. Res. Soc. Symp. Proc.* 806, Warrendale, PA, 2004) p.387.
- [18] S. Yoshida, T. Mizushima, T. Hatanai and A. Inoue, *IEEE Trans. Magn.* 36 (2000) 3424.
- [19] Schuh, C. A., Hufnagel, T. C. & Ramamurty, U. Mechanical behavior of amorphous alloys. *Acta Mater.* 55 (2007) 4067.
- [20] Spaepen, F. A microscopic mechanism for steady state inhomogeneous flow in metallic glasses. *Acta Metall.* 25 (1977) 407.
- [21] Argon, A. S. Plastic deformation in metallic glasses. *Acta Metall.* 27, (1979) 47.
- [22] Bernal, J. D. A geometrical approach to the structure of liquids. *Nature* 183, (1959) 141.
- [23] Cohen, M. H. & Turnbull, D. Molecular transport in liquids and glasses. *J. Chem. Phys.* 31, (1959) 1164.
- [24] Spaepen, F. Homogeneous flow of metallic glasses: A free volume

- perspective. *Scripta Mater.* 54, (2006) 363.
- [25] Yang, B., Wadsworth, J. & Nieh, T.-G. Thermal activation in Au-based bulk metallic glass characterized by high-temperature nanoindentation. *Appl. Phys. Lett.* 90, (2007) 061911.
- [26] Falk, M. L. & Langer, J. S. Dynamics of viscoplastic deformation in amorphous solids. *Phys. Rev.* E57, (1998) 7192.
- [27] Heggen, M., Spaepen, F. & Feuerbacher, M. Creation and annihilation of free volume during homogeneous flow of a metallic glass. *J. Appl. Phys.* 97, (2005) 033506.
- [28] Argon, A. S. & Kuo, H. Y. Plastic flow in a disordered bubble raft (an analog of a metallic glass). *Mater. Sci. Eng.*39, (1979) 101.
- [29] Srolovitz, D., Vitek, V. & Egami, T. An atomistic study of deformation of amorphous metals. *Acta Metall.* 31, (1983) 335.
- [30] Falk, M. L. Molecular-dynamics study of ductile and brittle fracture in model noncrystalline solids. *Phys. Rev.* B60, (1999) 7062.
- [31] Choi, I.-C. et al. Estimation of the shear transformation zone size in a bulk metallic glass through statistical analysis of the first pop-in stresses during spherical nanoindentation. *Scripta Mater.* 66, (2012) 923.
- [32] Choi, I.-C. et al. Indentation size effect and shear transformation zone size in a bulk metallic glass in two different structural states. *Acta Mater.* 60, (2012) 6862.

- [33] Ma, Y., Ye, J. H., Peng, G. J., Wen, D. H. & Zhang, T. H. Nanoindentation study of size effect on shear transformation zone size in a Ni - Nb metallic glass. *Mater. Sci. Eng. A627*, (2015) 153.
- [34] Pan, D., Inoue, A., Sakurai, T. & Chen, M. W. Experimental characterization of shear transformation zones for plastic flow of bulk metallic glasses. *Proc. Natl. Acad. Sci.* 105, (2008) 14769.
- [35] T.H. Courtney, "Mechanical behavior of materials", (McGraw-Hill International Editions, 2000) p.369.
- [36] Qiao, J. C. & Pelletier, J. M. Dynamic mechanical relaxation in bulk metallic glasses: A review. *J. Mater. Sci. Tech.* 30, (2014) 523.
- [37] Nieh, T. G. & Wadsworth, J. Homogeneous deformation of bulk metallic glasses. *Scripta Mater.* 54, (2006) 387.
- [38] Schroers, J. Processing of bulk metallic glass. *Adv. Mater.* 22, (2010) 1566.
- [39] Steif, P. S., Spaepen, F. & Hutchinson, J. W. Strain localization in amorphous metals. *Acta Metall.* 30, (1982) 447.
- [40] Sun, Y., Concustell, A. & Greer, A. L. Thermomechanical processing of metallic glasses: extending the range of the glassy state. *Nature Rev. Mater.*, (2016) 16039.
- [41] Kimura, H. & Masumoto, T. A model of the mechanics of serrated flow in an amorphous alloy. *Acta Metall.* 31, 231-240 (1983).

- [42] Qiao, J., Jia, H. & Liaw, P. K. Metallic glass matrix composites. *Mater. Sci. Eng. R100*, (2016) 1.
- [43] Shimizu, F., Ogata, S. & Li, J. Yield point of metallic glass. *Acta Mater.*54, (2006) 4293.
- [44] Ogata, S., Shimizu, F., Li, J., Wakeda, M. & Shibutani, Y. Atomistic simulation of shear localization in Cu - Zr bulk metallic glass. *Intermetallics* 14, (2006) 1033.
- [45] Klaumünzer, D., Maaß, R. & Löffler, J. F. Stick-slip dynamics and recent insights into shear banding in metallic glasses. *J. Mater. Res.* 26, (2011) 1453.
- [46] Matthews, D. T. A., Ocelík, V., Bronsveld, P. M. & De Hosson, J. T. M. An electron microscopy appraisal of tensile fracture in metallic glasses. *Acta Mater.* 56, (2008) 1762.
- [47] Liu, C. T. et al. Test environments and mechanical properties of Zr-base bulk amorphous alloys. *Metall and Mat Trans A29*, (1998) 1811.
- [48] Lewandowski, J. J. & Greer, A. L. Temperature rise at shear bands in metallic glasses. *Nature Mater.*5, (2006) 15.
- [49] Yang, B. et al. In-situ thermographic observation of mechanical damage in bulk-metallic glasses during fatigue and tensile experiments. *Intermetallics* 12, (2004) 1265.
- [50] Spaepen, F. Metallic glasses: Must shear bands be hot? *Nature Mater.* 5, (2006) 7.
- [51] Cheng, Y. Q., Han, Z., Li, Y. & Ma, E. Cold versus hot shear

- banding in bulk metallic glass. *Phys. Rev. B*80, (2009) 134115.
- [52] Maaß, R., Klaumünzer, D., Villard, G., Derlet, P. M. & Löffler, J. F. Shear-band arrest and stress overshoots during inhomogeneous flow in a metallic glass. *Appl. Phys. Lett.*100, (2012) 071904.
- [53] Maaß, R. & Löffler, J. F. Shear-band dynamics in metallic glasses. *Adv. Func. Mater.*25, (2015) 2353.
- [54] Park, E. S. Understanding of the shear bands in amorphous metals. *Applied Microscopy*45, (2015) 63.
- [55] Demetriou, M. D. et al. A damage-tolerant glass. *Nature Mater.*10, (2011) 123.
- [56] Z.F. Zhang, J. Eckert and L. Schultz, *Acta Mater.* 51 (2003) 1167.
- [57] J.W. Weeton, "engineer' Guide to Composite Materials" (ASM, Metals Park, Ohio, 1987).
- [58] Lee, M.L., Y. Li, and C.A. Schuh . *Acta Mater.* 52: (2004) 4121.
- [59] Shen, B.L., H. Men, and A. Inoue . *Appl. Phys. Lett.* 89: (2006) 101915-1.
- [60] Qin, C.L., W. Zhang, K. Asami, H.M. Kimura, X.M. Wang, and A. Inoue. *Acta Mater.* 54: (2006) 3713.
- [61] Sun, G.Y., G. Chen, and G.L. Chen. *Intermetallics* 15: (2007) 632.
- [62] Chen, L.Y., Z.D. Fu, W. Zeng, G.Q. Zhang, Y.W. Zeng, G.L. Xu, S.L. Zhang, and J.Z. Jiang. *J. Alloys Compd.* 443: (2007) 105.
- [63] Fan, C., L. Kecskes, T. Jiao, H. Choo, A. Inoue, and P.K. Liaw. *Mater. Trans.* 47: (2006) 817.
- [64] Kim, D. H., Kim, W. T., Park, E. S., Mattern, N. & Eckert, J.

- Phase separation in metallic glasses. *Prog. Mater. Sci.*58, (2013) 1103.
- [65] Chou, C. P. P. & Spaepen, F. Some mechanical properties of phase separated Pd_{0.74}Au_{0.08}Si_{0.38} metallic glasses. *Acta Metall.*23, (1975) 609.
- [66] Krebs, H. U., Webb, D. J. & Marshall, A. F. Phase separation in amorphous Fe-Zr: Comparison of sputtered and solid-state-reacted films. *Phys. Rev. B*35, (1987) 5392.
- [67] Okumura, H., Inoue, A. & Masumoto, T. Heating rate dependence of two glass transitions and phase separation for a La₅₅Al₂₅Ni₂₀ amorphous alloy. *Acta Metall. Mater.*41, (1993) 915.
- [68] Schneider, S., Thiyagarajan, P. & Johnson, W. L. Formation of nanocrystals based on decomposition in the amorphous Zr_{41.2}Ti_{13.8}Cu_{12.5}Ni₁₀Be_{22.5} alloy. *Appl. Phys. Lett.*68, (1996) 493.
- [69] Busch, R., Schneider, S., Peker, A. & Johnson, W. L. Decomposition and primary crystallization in undercooled Zr_{41.2}Ti_{13.8}Cu_{12.5}Ni_{10.0}Be_{22.5} melts. *Appl. Phys. Lett.*67, (1995) 1544.
- [70] Hays, C. C., Kim, C. P. & Johnson, W. L. Large supercooled liquid region and phase separation in the Zr - Ti - Ni - Cu - Be bulk metallic glasses. *Appl. Phys. Lett.*75, (1999) 1089.
- [71] Han, J. H., Mattern, N., Kim, D. H. & Eckert, J. Phase separation and microstructure evolution of rapidly quenched Gd - Hf - Co -

- Al alloys. *J. Alloy Compd.*509, Supplement 1, (2011) S42.
- [72] Mattern, N. et al. Phase separation in $\text{Cu}_{46}\text{Zr}_{47-x}\text{Al}_7\text{Gd}_x$ metallic glasses. *J. Alloy Compd.*509, Supplement 1, (2011) S23.
- [73] Sohn, S. W., Yook, W., Kim, W. T. & Kim, D. H. Phase separation in bulk-type Gd - Zr - Al - Ni metallic glass. *Intermetallics* 23, (2012) 57.
- [74] Mattern, N. et al. Phase separation in Ni - Nb - Y metallic glasses. *J. Alloy Compd.* 495, (2010) 299.
- [75] Chang, H. J., Park, E. S. & Kim, D. H. Nano-scale shell in phase separating Gd-Ti-Al-Co metallic glass. *Applied microscopy*43, (2013) 98.
- [76] Han, J. H. et al. Phase separation in $\text{Zr}_{56-x}\text{Gd}_x\text{Co}_{28}\text{Al}_{16}$ metallic glasses ($0 \leq x \leq 20$). *Acta Mater.*66, (2014) 262.
- [77] Park, B. J. et al. Phase separating bulk metallic glass: A hierarchical composite. *Phys. Rev. Lett.*96, (2006) 245503.
- [78] Park, E. S. et al. In situ formation of two glassy phases in the Nd - Zr - Al - Co alloy system. *Scripta Mater.*56, (2007) 197.
- [79] Kündig, A. A., Ohnuma, M., Ping, D. H., Ohkubo, T. & Hono, K. In situ formed two-phase metallic glass with surface fractal microstructure. *Acta Mater.*52, (2004) 2441.
- [80] Park, E. S. & Kim, D. H. Phase separation and enhancement of plasticity in Cu - Zr - Al - Y bulk metallic glasses. *Acta Mater.*54, (2006) 2597.
- [81] Inoue, A. Stabilization of metallic supercooled liquid and bulk

- amorphous alloys. *Acta Mater.*48, (2000) 279.
- [82] Park, B. J., Chang, H. J., Kim, D. H. & Kim, W. T. In situ formation of two amorphous phases by liquid phase separation in Y - Ti - Al - Co alloy. *Appl. Phys. Lett.*85, (2004) 6353.
- [83] Mattern, N. et al. Spinodal decomposition of Ni - Nb - Y metallic glasses. *Acta Mater.*57, (2009) 903.
- [84] Chang, H. J., Yook, W., Park, E. S., Kyeong, J. S. & Kim, D. H. Synthesis of metallic glass composites using phase separation phenomena. *Acta Mater.*58, (2010) 2483.
- [85] Han, J. H., Mattern, N., Schwarz, B., Kim, D. H. & Eckert, J. Phase separation and magnetic properties in Gd - (Hf,Ti,Y) - Co - Al metallic glasses. *Scripta Mater.*67, (2012) 149.
- [86] Jayaraj, J., Fleury, E., Park, B. J., Kim, D. H. & Kim, W. T. Synthesis and characterization of nanometer-sized Ti-based amorphous powders. *J. Mater. Res.*22, (2007) 1754.
- [87] Jayaraj, J., Park, B. J., Kim, D. H., Kim, W. T. & Fleury, E. Nanometer-sized porous Ti-based metallic glass. *Scripta Mater.*55, (2006) 1063.
- [88] Lupis, C. H. P. *Chemical thermodynamics of materials.* (North-Holland, 1983).
- [89] Hancock, H. *Theory of Maxima and Minima.* (Ginn, 1917).
- [90] Redlich, O. & Kister, A. T. Algebraic representation of thermodynamic properties and the classification of solutions. *Industrial & Engineering Chemistry*40, (1948) 345.

- [91] Cahn, J. W. Phase separation by spinodal decomposition in isotropic systems. *J. Chem. Phys.* 42, (1965) 93.
- [92] ISO/ASTM 52900-15
- [93] R.J. Friel, *Power ultrasonic for additive manufacturing and consolidation of materials* (2015) 313.
- [94] A.R. Nassar et al., Intra-layer closed-loop control of build plan during directed energy additive manufacturing of Ti - 6Al - 4V, *Additive Manufacturing* Vol. 6 (2015) 39
- [95] J. Xiong et al., Heat propagation of circular thin-walled parts fabricated in additive manufacturing using gas metal arc welding *Journal of Materials Processing Technology* Vol. 251 (2018) 12.
- [96] X. Liet al, *Solid Freeform Fabrication 2016*, TMS, Austin, USA (2016) 219.
- [97] D. Jerzog et al., *Additive manufacturing of metals ActaMaterialia* Vol. 117 (2016) p371-392
- [98] Bidare et al., Fluid and particle dynamics in laser powder bed fusion, *Acta Materialia*, Vol. 142 (2018) 107.
- [99] L. Parry et al. Understanding the effect of laser scan strategy on residual stress in selective laser melting through thermo-mechanical simulation, *Additive Manufacturing* Vol.12 (2016) 1.
- [100] T. Deb Roy et al., *Progress in Materials Science*, Vol. 92 (2018), 112.
- [101] M. Newville, IFEFFIT: interactive XAFS analysis and FEFF

- fitting, *Journal of synchrotron radiation* 8(2) (2001) 322.
- [102] M. Newville, *Fundamentals of XAFS, Reviews in Mineralogy and Geochemistry* 78(1) (2014) 33.
- [103] A.Inoue, High strength bulk amorphous alloys with low critical cooling rates(overview), *Mat. Trans, JIM* 36(7) (1995) 866.
- [104] E. Park, J. Kyeong, D.Kim, Phase separation and improved plasticity by modulated heterogeneity in Cu-[Zr, Hf]-[Gd, Y]-Al metallic glassed, *Scripta Materialia* 57(1) (2007) 49.
- [105] J. Oh, T.Ohkubo, Y.Kim, E. Fleury, K.Hono, Phase separation in Cu₄₃Zr₄₃Al₇Ag₇ bulk metallic glasses, *Scripta Materialia* 53(2) (2005) 165.
- [106] H. Chang, E. Park, Y.Jung, M.Kim, D.Kim, The effect of Zr addition in glass forming ability of Ni-Nb alloy system, *Journal of alloys and compounds* 434 (2007) 156.
- [107] F.R. De Boer, W. Matterns, R. Boom, A. Miedema, A. Niessen, *Cohesion in metals*, (1988)
- [108] D. Koningberger, R. Prins, *X-ray absorption : Principle, applications, techniques of EXAFS, SEXAFS, and XANES*, (1988)
- [109] B. Warren, B Averbach, B. Roberts, Atomic size effect in X-ray scattering by alloy, *Journal of Applied Physics* 22(12) (1951) 1493.
- [110] G. Cargill, F. Spaepen, Description of chemical ordering in amorphous alloys, *Journal of Non-Cry. Solids* 43(1) (1981) 91.
- [111] E.S. Park, H.J. Chang, D.H. Kim, Effect of addition of Be on

- glass-forming ability, plasticity and structural change in Cu - Zr bulk metallic glasses, *Acta Materialia* 56(13) (2008) 3120.
- [112] T. Egami, Formation and deformation of metallic glasses: atomistic theory, *Intermetallics* 14(8) (2006) 882.
- [113] X.F. Wang, T.E. Jones, Y. Wu, Z.P. Lu, S. Halas, T. Durakiewicz, M.E. Eberhart, An electronic criterion for assessing intrinsic brittleness of metallic glasses, *The Journal of Chemical Physics* 141(2) (2014) 024503.
- [114] A.L. Ankudinov, J.J. Rehr, S.R. Bare, Hybridization peaks in Pt - Cl XANES1 Supported in part by the US DOE and by UOP LLC.1, *Chemical Physics Letters* 316(5) (2000) 495.
- [115] Y. Shimakawa, H. Imai, H. Kimura, S. Kimura, Y. Kubo, E. Nishibori, M. Takata, M. Sakata, K. Kato, Z. Hiroi, Orbital hybridization and covalency in paraelectric and ferroelectric SrBi₂Nb₂O₉, *Physical Review* B66(14) (2002) 144110.
- [116] V.V. Poltavets, M.Croft, M.Greenblatt, Charge transfer, hybridization and local inhomogeneity effects in Na_xCoO₂·yH₂O : An x-ray absorption spectroscopy study, *Physical Review* B74(12) (2006) 125103.
- [117] X. Bian, G. Wang, K. Chan, J. Ren, Y. Gao, Q. Zhai, Shear avalanches in metallic glasses under nanoindentation: Deformation units and rate dependent strain burst cut-off, *Applied Physics Letters* 103(10) (2013) 101907.
- [118] J. Lee, S. Kim, E. Park, In-situ synthesis and mechanical

- properties of Zr-based bulk metallic glass matrix composites manipulated by nitrogen additions, *Intermetallics* 91 (2017) 70
- [119] J. Lee, J. Kim, H. Oh, J. Park, E. Park, Abnormal devitrification behavior and mechanical response of cold-rolled Mg-rich Mg-Cu-Gd metallic glasses, *Acta Materialia* 116 (2016) 238.
- [120] C. Fan, A. Inoue, Improvement of mechanical properties by precipitation of nanoscale compound particles in Zr - Cu - Pd - Al amorphous alloys, *Materials Transactions, JIM* 38(12) (1997) 1040.
- [121] C. Hays, C. Kim, W.L. Johnson, Microstructure controlled shear band pattern formation and enhanced plasticity of bulk metallic glasses containing in situ formed ductile phase dendrite dispersions, *Physical Review Letters* 84(13) (2000) 2901.
- [122] G. He, J. Eckert, W. Löser, L. Schultz, Novel Ti-base nanostructure - dendrite composite with enhanced plasticity, *Nature materials* 2(1) (2003) 33.
- [123] E. Park, D. Kim, T. Ohkubo, K. Hono, Enhancement of glass forming ability and plasticity by addition of Nb in Cu - Ti - Zr - Ni - Si bulk metallic glasses, *Journal of non-crystalline solids* 351(14) (2005) 1232.
- [124] D.-S. Sung, O.-J. Kwon, E. Fleury, K.-B. Kim, J.-C. Lee, D.-H. Kim, Y.-C. Kim, Enhancement of the glass forming ability of Cu-Zr-Al alloys by Ag addition, *Metals and materials International* 10(6) (2004) 575.

- [125] E. Park, H. Chang, D. Kim, T. Ohkubo, K. Hono, Effect of the substitution of Ag and Ni for Cu on the glass forming ability and plasticity of Cu 60 Zr 30 Ti 10 alloy, *Scripta Materialia* 54(9) (2006) 1569.
- [126] E. Park, J. Lee, D. Kim, Effect of Ag addition on the improvement of glass-forming ability and plasticity of Mg - Cu - Gd bulk metallic glass, *Journal of materials research* 20(9) (2005) 2379.
- [127] M. Lee, J. Lee, D. Bae, W. Kim, D. Sordelet, D. Kim, A development of Ni-based alloys with enhanced plasticity, *Intermetallics* 12(10) (2004) 1133.
- [128] J. Kim, H.S. Oh, W. Kim, P.-P. Choi, D. Raabe, E.S. Park, Modulation of plastic flow in metallic glasses via nanoscale networks of chemical heterogeneities, *Acta Materialia* 140(Supplement C) (2017) 116.
- [129] N. Mattern, M. Zinkevich, W. Löser, G. Behr, J. Acker, Experimental and thermodynamic assessment of the Nb-Ni-Y system, *Journal of phase equilibria and diffusion* 29(2) (2008) 141.
- [130] A. Dinsdale, SGTE unary database, version 4.4, 2002.
- [131] O. Redlich, A. Kister, Algebraic representation of thermodynamic properties and the classification of solutions, *Industrial & Engineering Chemistry* 40(2) (1948) 345.
- [132] C.H. Lupis, *Chemical thermodynamics of materials*, Elsevier

Science Publishing Co., Inc., 1983 (1983) 581.

- [133] C. J. Gilbert, R. O. Ritchie, and W. L. Johnson. Appl. Phys. Lett. 71, (1997) 476.
- [134] A. D. Padsalgikar and M. S. Ellison. Polym. Eng. Sci. 37(6), (1997) 994.
- [135] T. Hao. Phys. Chem. Chem. Phys.17(34), (2015) 21885.
- [136] K. S. Nakayama, Y. Yokoyama, T. Wada, N. Chen and A. Inoue. Nano Lett.12(5), (2012) 2404.
- [137] S. Yaginuma, C. Nakajima, N. Kaneko, Y. Yokoyama and K. S. Nakayama. Sci. Rep. 5, (2015) 10711.

Abstract in Korean

Tailor-made 비정질 합금에서 구조-특성간 상관관계 규명

박 태 규

서울대학교 공과대학 재료공학부

비정질 합금은 결정질 합금과는 다른 무질서한 원자 배열 구조를 가짐으로 인해 기존의 이론으로 설명할 수 없는 새로운 물리적, 화학적, 기계적 특성을 나타내며, 특히 기계적 특성이 매우 우수하기 때문에 비정질 재료를 대형화할 경우 구조용 재료로서의 적용 가능성이 매우 높다. 그러나, 비정질 합금은 결정질 합금과 달리 슬립, 전위와 같은 소성 변형 기구가 존재하지 않기 때문에 항복이 일어남과 동시에 갑작스러운 파괴가 일어난다는 취약점을 가지고 있다. 아울러, 빠른 냉각속도를 필요로 하는 비정질 형성능으로 인해 일반적인 금속의 제조공정으로는 제작하기가 쉽지 않아, 비정질의 대형화에는 한계가 있는 상황이다. 따라서, 비정질 재료의 구조용 재료로의 활용 가능성을 확대하기 위해서는 재료의 소성 변형능을 향상 시키고, 비정질 구조를 유지하면서 대형화하는 것이 필수적이다.

따라서, 본 연구에서는 첨가원소에 따른 비정질 합금의 원자단위의 구조변화를 분석하고, 구조변화에 따른 물성 변화를 실험적으로 고찰

함으로서 기존 비정질 재료의 구조재로서의 적용한계를 극복하고 우리가 원하는 대로 단일 비정질상의 구조를 제어할 수 있는 개념을 제시하고자 하였다. 아울러, 최근 제조업 제조기술의 혁신을 주도하고 있는 3D 프린팅 공정을 이용, 비정질 분말의 적층 가공(Additive Manufacturing)을 통한 대형화 연구를 통해 기존 비정질 합금의 활용한계를 극복코자 하였다.

먼저, 단일 비정질상의 구조 변화 및 물성변화를 고찰하기 위하여 간단한 이원계 합금계(Ni-Nb)를 선택한 후 구성 원소간 양의 혼합열을 가지고 혼합열의 상대적인 크기가 다른 일련의 원소(Zr, Gd, Y)를 첨가하는 방식으로 합금을 설계하였다. Ni-Nb 이원계 합금에 양의 혼합열이 상대적으로 작은 Zr(+4 kJ/mol)을 첨가할 경우, 투과전자현미경이나 SAXS(small angle X-ray Scattering)를 통해서는 단일 비정질 상에서 어떠한 불균일성을 확인할 수 없었다. 그러나, EXAFS(Extended X-ray Absorption Fine Structure)를 이용하여 원자간 결합 거리, 배위수 등을 확인한 결과, Zr을 첨가함에 따라, 단일 비정질상내 원자단위의 국부적인 불균일성을 확인할 수 있었다. 아울러, 이러한 원자단위의 국부적인 불균일성이 전단띠가 생성될 수 있는 사이트를 많이 부여하여 집중된 한 전단띠에 의한 급작스러운 파괴를 막을 수 있고 궁극적으로는 비정질의 연신을 향상시킬 수 있음을 리본의 굽힘실험 등을 통해 실험적으로 최초로 규명하였다. 아울러, 이러한 원자단위의 불균일성과 물성간의 상관관계를 벌크 시편을 통해 확인한 결과, 냉각속도에도 영향을 받으며, 이러한 조성, 냉각속도 등의 정밀 제어를 통해 단일 비정질상의 구조를 유지하면서 재료의 강도와 연신을 동시에 증가시킬 수 있음을 규명하였다.

한편, Ni-Nb 이원계 합금에 양의 혼합열이 상대적으로 큰 Y,

Gd(+30 kJ/mol)을 첨가하는 경우, 상분리 비정질을 얻을 수 있었으며, 혼합열의 크기가 같음에도 각각의 첨가 원소에 따라, 상분리 비정질의 미세구조 및 열적 특성은 다름을 확인하였다. 열역학적 데이터를 바탕으로 미세구조의 차이를 유발할 수 있는 상분리 비정질의 miscibility gap 을 계산하고 governing factor를 고찰함으로써, 상분리 비정질 합금의 미세구조를 제어할 수 있는 새로운 합금설계 개념을 수립하였다.

대형화 연구와 관련해서는 비정질 분말의 3D 프린팅 레이저 적층 가공을 통해 공정변수 제어에 따른 프린팅 결과물의 물성변화를 확인하였다. 이를 통해 비정질 조성의 분말을 이용하여 3D 프린팅의 공정변수와 입열량을 적정하게 제어할 경우 비정질을 구조를 유지하면서 대형화할 수 있었다. 아울러, 3D 프린팅을 통해 제작된 비정질의 기계적 거동 실험을 통해 3D 프린팅을 통해 비정질 제작시, 전통적인 방식의 비정질 제조와는 달리 냉각속도의 차이가 단일 비정질내에 존재하고, 이러한 냉각속도의 차이에 의해 유발된 단일 비정질내의 원자단위 불균일성이 비정질의 연신을 증가시킬 수 있음을 규명하였다.

본 연구의 비정질 구조와 특성 상관관계에 대한 폭넓은 이해는 궁극적으로 비정질 재료의 우수한 특성을 적절히 이용할 수 있는 다양한 합금 설계 및 공정에 대한 새로운 방법을 제시할 수 있을 것으로 보인다. 또한 더 나아가 비정질 재료의 산업적 활용분야 확대를 위한 맞춤형 비정질을 제조할 수 있는 새로운 이정표를 제시하였다고 사료된다.

주요어 : 비정질 합금, 양의 혼합열, 소성 변형능, 불균일성, 선호 결합,
레이저 분말 적층가공

학 번 : 2013-30179